

AD-A216 598

DTRC-89/029 Advanced Panel Method for Ship Wave Inviscid Flow Theory (SWIFT)

# David Taylor Research Center

Bethesda, MD 20084-5000

DTIC FILE COPY

2

DTRC-89/029 November 1989

Ship Hydromechanics Department  
Research and Development Report

## Advanced Panel Method for Ship Wave Inviscid Flow Theory (SWIFT)

by

Yoon-Ho Kim

Sea Heon Kim

Thomas Lucas

DTIC  
ELECTE  
JAN 11 1990  
S & E D



Approved for public release; distribution is unlimited.

90 01 10 143

## MAJOR DTRC TECHNICAL COMPONENTS

- CODE 011 DIRECTOR OF TECHNOLOGY, PLANS AND ASSESSMENT
- 12 SHIP SYSTEMS INTEGRATION DEPARTMENT
  - 14 SHIP ELECTROMAGNETIC SIGNATURES DEPARTMENT
  - 15 SHIP HYDROMECHANICS DEPARTMENT
  - 16 AVIATION DEPARTMENT
  - 17 SHIP STRUCTURES AND PROTECTION DEPARTMENT
  - 18 COMPUTATION, MATHEMATICS & LOGISTICS DEPARTMENT
  - 19 SHIP ACOUSTICS DEPARTMENT
  - 27 PROPULSION AND AUXILIARY SYSTEMS DEPARTMENT
  - 28 SHIP MATERIALS ENGINEERING DEPARTMENT

### DTRC ISSUES THREE TYPES OF REPORTS:

1. **DTRC reports, a formal series**, contain information of permanent technical value. They carry a consecutive numerical identification regardless of their classification or the originating department.
2. **Departmental reports, a semiformal series**, contain information of a preliminary, temporary, or proprietary nature or of limited interest or significance. They carry a departmental alphanumeric identification.
3. **Technical memoranda, an informal series**, contain technical documentation of limited use and interest. They are primarily working papers intended for internal use. They carry an identifying number which indicates their type and the numerical code of the originating department. Any distribution outside DTRC must be approved by the head of the originating department on a case-by-case basis.

UNCLASSIFIED

SECURITY CLASSIFICATION OF THIS PAGE

REPORT DOCUMENTATION PAGE				Form Approved OMB No 0704-0188	
1a REPORT SECURITY CLASSIFICATION <b>UNCLASSIFIED</b>			1b RESTRICTIVE MARKINGS		
2a SECURITY CLASSIFICATION AUTHORITY			3 DISTRIBUTION / AVAILABILITY OF REPORT <b>Approved for public release; distribution is unlimited.</b>		
2b DECLASSIFICATION / DOWNGRADING SCHEDULE <b>N/A</b>					
4. PERFORMING ORGANIZATION REPORT NUMBER(S) <b>DTRC-89/029</b>			5 MONITORING ORGANIZATION REPORT NUMBER(S)		
6a. NAME OF PERFORMING ORGANIZATION <b>David Taylor Research Center</b>	6b OFFICE SYMBOL (If applicable) <b>Code 1522</b>	7a. NAME OF MONITORING ORGANIZATION <b>Naval Sea Systems Command</b>			
6c. ADDRESS (City, State, and ZIP Code) <b>Bethesda, MD 20084-5000</b>		7b ADDRESS (City, State, and ZIP Code) <b>Washington, D.C. 20362</b>			
8a. NAME OF FUNDING / SPONSORING ORGANIZATION <b>Naval Sea Systems Command</b>	8b OFFICE SYMBOL (If applicable)	9 PROCUREMENT INSTRUMENT IDENTIFICATION NUMBER			
8c. ADDRESS (City, State, and ZIP Code) <b>Washington, D. C. 20362</b>		10 SOURCE OF FUNDING NUMBERS			
		PROGRAM ELEMENT NO <b>61153N</b>	PROJECT NO	TASK NO <b>SR 0230101</b>	WORK UNIT ACCESSION NO <b>DN505016</b>
11. TITLE (Include Security Classification) <b>Advanced Panel Method for Ship Wave Inviscid Flow Theory (SWIFT)</b>					
12. PERSONAL AUTHOR(S) <b>Kim, Yoon-Ho, Sea-Heon Kim, and Thomas Lucas</b>					
13a. TYPE OF REPORT <b>(Final)</b>	13b TIME COVERED FROM _____ TO _____	14. DATE OF REPORT (Year, Month, Day) <b>1989 November</b>		15 PAGE COUNT <b>75</b>	
16 SUPPLEMENTARY NOTATION					
17. COSATI CODES			18. SUBJECT TERMS (Continue on reverse if necessary and identify by block number)		
FIELD	GROUP	SUB-GROUP	<b>Wave Profile; Wave-Making Resistance; Higher-Order Panel Method.</b>		
19 ABSTRACT (Continue on reverse if necessary and identify by block number) An advanced numerical scheme for computing the free surface flow about a ship is presented. The present approach is a higher order panel method which employs a parabolic quadrilateral as a basic element. It can represent an actual curved ship hull surface more accurately with a smaller number of panels than is possible with a flat panel approximation. Singularity strength can vary linearly or quadratically across the panel. A sample unbounded flow problem with an analytic solution was considered first to validate the present approach and examine the characteristics of accuracy and coverage compared with those of the conventional low-order approaches (constant source strength across flat panel). The Wigley hull and the Series 60, $C_g=0.60$ hull, which have been studied extensively, were selected for sample free surface flow computations. Comparisons between calculated and experimental results show good agreement. A modified body boundary condition was suggested to simulate a dry transom stern numerically, and calculated results show good correspondence with test data.					
20 DISTRIBUTION / AVAILABILITY OF ABSTRACT <input checked="" type="checkbox"/> UNCLASSIFIED/UNLIMITED <input type="checkbox"/> SAME AS RPT <input type="checkbox"/> DTIC USERS			21 ABSTRACT SECURITY CLASSIFICATION <b>Unclassified</b>		
22a NAME OF RESPONSIBLE INDIVIDUAL <b>Yoon-Ho Kim</b>			22b TELEPHONE (Include Area Code) <b>(202) 227-1594</b>	22c OFFICE SYMBOL <b>Code 1522</b>	

## CONTENTS

	Page
<b>Abstract</b> .....	1
<b>Administrative Information</b> .....	1
<b>Introduction</b> .....	1
<b>Mathematical Formulation</b> .....	4
<b>Numerical Method</b> .....	6
Higher-Order Curved Panel .....	7
Induced Potential and Velocity .....	9
Numerical Approximation of the Far-Field Behavior of the Solution .....	10
Implementation of Numerical Solution .....	13
Transom Stern .....	16
Convergence Test of Numerical Solution .....	17
<b>Results and Discussion</b> .....	19
Sphere .....	19
Wigley Hull .....	20
Series 60, $C_B = 0.60$ .....	22
Athena Hull .....	23
Large Combatant Ships .....	23
Comparison with Other Approaches .....	24
<b>Conclusions</b> .....	25
<b>Recommendations</b> .....	26
<b>Acknowledgments</b> .....	27
<b>Appendix A. Computation of Velocity Potential <math>\Phi</math></b> .....	29
<b>Appendix B. Computation of H Integrals</b> .....	33
<b>References</b> .....	63

## FIGURES

1. Coordinate system .....	35
2. Field point/panel geometry .....	35
3. 3-D perspective view of the surface panel network .....	35
4. Network of panels .....	36
5. Wigley hull form (from Shearer and Cross, 1965) .....	36
6. Convergence test for X-direction truncation boundary .....	37
7. Convergence test for Y-direction truncation boundary .....	37

## FIGURES (Continued)

	Page
8. Convergence test for number of panels .....	38
9. Illustration of body and free surface panel network .....	38
10. Regular and random paneling of sphere .....	39
11. Wave profile comparison for Wigley hull at $F_n=0.250$ .....	40
12. Wave profile comparison for Wigley hull at $F_n=0.267$ .....	40
13. Wave profile comparison for Wigley hull at $F_n=0.289$ .....	41
14. Wave profile comparison for Wigley hull at $F_n=0.316$ .....	41
15. Wave profile comparison for Wigley hull at $F_n=0.354$ .....	42
16. Wave profile comparison for Wigley hull at $F_n=0.408$ .....	42
17. Wave-making resistance comparison for Wigley hull .....	43
18. 3-D perspective view of Wigley hull generated waves at $F_n=0.408$ .....	43
19. Predicted wave contour plot for Wigley hull at $F_n=0.408$ .....	44
20. Lines of Series 60, $C_B=0.60$ (from Todd, 1953) .....	44
21. Wave profile comparison for Series 60 at $F_n=0.220$ .....	45
22. Wave profile comparison for Series 60 at $F_n=0.250$ .....	45
23. Wave profile comparison for Series 60 at $F_n=0.280$ .....	46
24. Wave profile comparison for Series 60 at $F_n=0.300$ .....	46
25. Wave profile comparison for Series 60 at $F_n=0.320$ .....	47
26. Wave profile comparison for Series 60 at $F_n=0.350$ .....	47
27. Wave-making resistance comparison for Series 60 .....	48
28. Longitudinal wave-cut comparison for Series 60 .....	48
29. Body plan of the fore body of Athena .....	49
30. Body plan of the aft body of Athena .....	49
31. Wave profile comparison for Athena hull at $F_n=0.350$ .....	50
32. Wave profile comparison for Athena hull at $F_n=0.412$ .....	50
33. Wave profile comparison for Athena hull at $F_n=0.484$ .....	51
34. Wave profile comparison for Athena hull at $F_n=0.651$ .....	51
35. Wave profile comparison behind stern at $F_n=0.484$ .....	52
36. Body plans of Models X and A .....	53
37. Body plans of Models A and C .....	53
38. Wave profile along the hull at $F_n=0.179$ .....	54
39. Wave profile along the hull at $F_n=0.238$ .....	54
40. Wave profile along the hull at $F_n=0.298$ .....	55
41. Wave profile along the hull at $F_n=0.179$ for Models A and C .....	55

## FIGURES (Continued)

	Page
42. Wave profile along the hull at $F_n=0.238$ for Models A and C .....	56
43. Wave profile along the hull at $F_n=0.298$ for Models A and C .....	56
44. Capacitance wire wave probes for wave-cut measurements .....	57
45. Longitudinal wave cut at $F_n=0.238$ (Probe 1) .....	57
46. Longitudinal wave cut at $F_n=0.238$ (Probe 2) .....	58
47. Longitudinal wave cut at $F_n=0.238$ (Probe 3) .....	58
48. Longitudinal wave cut at $F_n=0.238$ (Probe 4) .....	59
49. Longitudinal wave cut at $F_n=0.238$ (Probe 5) .....	59

## TABLES

1. Comparisons between flat panel and curved panel results .....	60
2. Tables of offsets, Series 60, $C_B=0.60$ .....	60
3. Offsets for the high-speed hull, Athena .....	61
4. Principal dimensions and form coefficients of Models X, A, and C .....	61

Accession For	
NTIS GRA&I	<input checked="" type="checkbox"/>
DTIC TAB	<input type="checkbox"/>
Unannounced	<input type="checkbox"/>
Justification	
By _____	
Distribution/	
Availability Codes	
Dist	Avail and/or Special
A-1	



## NOMENCLATURE

$B$	Beam, moulded of ship
$C_B$	Block coefficient, $C_B = \text{displacement}/(LwlxBxT)$
$C_F$	Force coefficient vector, $C_F = \text{Force}/(1/2 \rho U^2 S)$
$C_p$	Hydrodynamic pressure coefficient, $C_p = p/(1/2 \rho U^2)$
$C_W$	Wave-making resistance coefficient, $C_W = \text{Resistance}/(1/2 \rho U^2 S)$
$F_n$	Froude number, $F_n = U/\sqrt{gL}$
$g$	Gravitational acceleration
$h$	Characteristic panel length
$l$	Double body streamline coordinate
$Lwl$	Length of a ship
$n_x, n_y, n_z$	Unit normal vector component
$p$	Hydrodynamic pressure
$\vec{P}$	Position vector, field point, $\vec{P} = P(x, y, z)$
$Q$	Singular point on a singularity surface, $Q = Q(\xi, \eta, \zeta)$
$r$	Distance, $r = (x^2 + y^2 + z^2)^{1/2}$
$\vec{R}$	Distance vector, $\vec{R} = \vec{P} - \vec{Q} = (x - \xi, y - \eta, z - \zeta)$
$S$	Surface element bounded by four corner points and wetted surface area of ship
$T$	Draught, moulded of ship
$U$	Mean forward speed of ship
$\vec{V}$	Absolute velocity, $\vec{V} = \vec{V}\phi$
$W_j$	Weighting function used for least square method
$x, y, z$	Coordinate system fixed on the body, or global coordinate system
$\phi$	Total velocity potential, $\phi = \Phi + \phi'$
$\phi'$	Disturbance velocity potential due to free surface wave
$\Phi$	Double body velocity potential
$\lambda_k$	Singularity parameter
$\nu$	Rayleigh viscosity
$\psi$	Disturbance velocity potential, $\phi = -Ux + \psi$
$\rho$	Fluid density
$\sigma(\xi, \eta)$	Source strength distribution, $\sigma(\xi, \eta) = \sigma_0 + \sigma_\xi \xi + \sigma_\eta \eta$
$\Sigma$	Quadrilateral formed by projection of the corner points of $S$ on $(\xi, \eta)$ -plane

$\tau(\xi, \eta)$	Doublet strength distribution, $\tau(\xi, \eta) = \tau_0 + \tau_\xi \xi + \tau_\eta \eta + 1/2 \tau_{\xi\xi} \xi^2 + \tau_{\xi\eta} \xi \eta + 1/2 \tau_{\eta\eta} \eta^2$
$\xi, \eta, \zeta$	Local coordinate system
$\zeta$	Nondimensionalized free surface profile. $\zeta = Z/(U^2/2g)$



**THIS PAGE INTENTIONALLY LEFT BLANK**

## ABSTRACT

An advanced numerical scheme for computing the free surface flow about a ship is presented. The present approach is a higher order panel method which employs a parabolic quadrilateral as a basic element. It can represent an actual curved ship hull surface more accurately with a smaller number of panels than is possible with a flat panel approximation. Singularity strength can vary linearly or quadratically across the panel. A sample unbounded flow problem with an analytic solution was considered first to validate the present approach and examine the characteristics of accuracy and convergence compared with those of the conventional low-order approaches (constant source strength across flat panel). The Wigley hull and the Series 60,  $C_B=0.60$  hull, which have been studied extensively, were selected for sample free surface flow computations. Comparisons between calculated and experimental results show good agreement. A modified body boundary condition was suggested to simulate a dry transom stern numerically, and calculated results show good correspondence with test data.

## ADMINISTRATIVE INFORMATION

This work was performed under the General Hydrodynamics Research Program, administered by the David Taylor Research Center (DTRC) Ship Hydromechanics Department, and was funded by the Naval Sea Systems Command (NAVSEA), Hull Research and Technology Office. Funding was provided under Program Element 61153N, Task Area SR 0230101, and Work Unit 1522-070. Additional funding was provided to the third author by the National Science Foundation under Grant Number ECS 8515174.

## INTRODUCTION

Many attempts to predict the wave-making resistance of surface ships have been made since Michell's<sup>1</sup> pioneering work at the end of the 19th century. However, due to a variety of difficulties, none of the existing methods have been fully satisfactory. In the present work a comprehensive modern effort, using a higher-order curved panel method, is adopted and applied to the computation of the free surface flow around a surface ship. This choice was partially motivated by a limitation in the Hess and Smith approach<sup>2</sup> observed in existing computational implementations. The Hess and Smith approach uses flat panels with constant source strength

over each panel. Methods employing this feature are quite sensitive to the geometric arrangement of panels.<sup>3</sup> Numerical problems arise when the solution is dependent on the variation of panel size and arrangement for a given configuration. Such problems place severe limitations on the development of automatic panelling or other complementary aids, which are important for ship designers in that they relieve users from the large amount of hard work and numerous judgements associated with producing the input geometry needed for accurate numerical solutions. Though the versatility of the Hess and Smith approach has been appreciated over the past decade, the need for basic improvement has become increasingly evident. In the present work we have employed a curved panel as a basic element. It is anticipated that the arrangement using curved panels will require a smaller number of curved panels than would flat panels to approximate the actual surface of the ship with the same degree of accuracy. Also, the source strength distribution on the body has been assumed to vary linearly across each panel. For the solution of the free surface flow problem we distributed either sources or doublets on the free surface. In the doublet network we have assumed quadratically varying doublet strengths across each panel for the sake of consistency with its quadratic geometric description. For the purpose of a later extension to the full nonlinear free surface boundary conditions, the software for curved free surface panels has also been included as a runtime option.

The capability of the present approach was carefully examined by applying it to the computation of unbounded potential flow problems first and then extending it to free surface flow problems. Comparison of the numerical results of the unbounded potential flow around a sphere with the exact solution showed that the present higher-order curved panel method gives a convergence rate of  $O(h^2)$ , while the rate of the zero-order flat panel method is only  $O(h)$ , where  $h$  denotes a characteristic length scale of the panel. Estimation of numerical accuracy of the calculated results for a free surface flow problem is far more difficult. First, there is no known analytical result with which to compare. Other difficulties are more specific and concern a variety of numerical approximations involved in the treatment of boundary conditions and the infinite computational fluid domain. Finally, one important quantity of interest, the wave-making resistance, is very small compared with other quantities, such as the velocity potential and the free surface elevation. In this report emphasis is placed on the accurate prediction of the free surface wave profile along a ship hull instead of on the wave-making

resistance. The prediction of the wave profile implies the detailed description of local flow phenomena while the wave-making resistance is a global quantity usually obtained by integrating the pressure, which is a local quantity, along the hull surface. It may be fruitless to attempt a computational method for an accurate prediction of the wave-making resistance without first achieving a corresponding accuracy of the local phenomena. It is also noted that none of the existing numerical schemes have been systematically verified for convergence and for the numerical approximations employed. The results have been shown to vary dramatically depending on such factors as the panel density and the numerical truncation of the computational fluid domain.<sup>3</sup> In this report the numerical results are carefully examined and the results are found to be quite robust with respect to changes in the truncated computational domain and both the ship hull and free surface panel density.

The numerical modeling of the free surface flow around a surface ship with a dry transom stern is an another major challenge for a modern free surface problem code. One of the outstanding features of the present analysis scheme SWIFT(Ship Wave Inviscid Flow Theory) is the treatment of the transom stern hull characteristic. This feature is particularly important for the Navy because most fast combatant ships have transom stern hulls. In addition, the numerous efforts for application of SWIFT to ship design and performance evaluation problems have motivated the development of extensive pre-processor codes (PANHULL) and post-processor software (PLTPRG) for geometry definition and graphic presentation.

Validation computations for the free surface flow problem have been made for the Wigley hull and the Series 60 hull,  $C_B = 0.60$ , for which extensive experimental measurements are available. Transom stern ship hulls have also been considered in detail. Here, emphasis has been given to the numerical results of wave profiles and comparisons with the experimental measurements. Predicted longitudinal wave cuts away from the ship have also been compared with the measurements.

## MATHEMATICAL FORMULATION

We consider a ship which moves in the positive  $x$ -direction with constant forward speed  $U$ . It is convenient to introduce a Cartesian coordinate system  $\vec{x} = (x, y, z)$  translating with the ship as shown in Fig. 1. The  $z=0$  plane is taken as the undisturbed free surface, the positive  $x$ -axis in the direction of the ship's forward velocity, and the positive  $z$ -axis upward. The fluid is assumed to be ideal, incompressible with constant density  $\rho$ , and its motion to be irrotational. With these assumptions the fluid velocity vector  $\vec{V}(\vec{x})$  is represented as the gradient of the velocity potential  $\phi(\vec{x})$  which satisfies the Laplace equation.

$$\nabla^2 \phi(\vec{x}) = 0 \quad (1)$$

throughout the fluid domain. On the submerged portion of the ship's wetted surface  $S$ , the normal velocity of the ship is equal to that of the adjacent fluid such that

$$\phi_n(\vec{x}) = 0 \quad \text{on } S. \quad (2)$$

On the free surface  $z = \zeta(x, y)$ , where  $\zeta$  is the free surface elevation, the kinematic boundary condition is expressed in terms of the substantial derivative  $D/Dt = \partial/\partial t + \vec{V} \cdot \vec{\nabla}$ , in the form

$$(D/Dt)(\zeta - z) = 0 \quad \text{on } z = \zeta. \quad (3)$$

An additional dynamic boundary condition is obtained by requiring that the pressure on the free surface be atmospheric:

$$(1/2)\vec{\nabla}\phi \cdot \vec{\nabla}\phi + gz = 0 \quad \text{on } z = \zeta. \quad (4)$$

Since Eq. (4) holds on the free surface, its substantial derivative can be set equal to zero. This derivative leads to an exact nonlinear free surface boundary condition.

$$(1/2)\vec{\nabla}\phi \cdot (\vec{\nabla}\phi \cdot \vec{\nabla}\phi) + g\phi_z = 0 \quad \text{on } z = \zeta. \quad (5)$$

with

$$\zeta = (1/2g)\nabla\phi\cdot\nabla\phi \quad \text{on } z = \zeta. \quad (6)$$

Finally, energy consideration requires that the velocity potential approach the uniform onset flow potential and that there be no waves far upstream of the ship:

$$\phi = \begin{cases} -Ux + o(1/r) & x > 0 \\ -Ux + O(1/r) & x < 0 \end{cases} \quad (7)$$

where  $r = \{x^2 + y^2 + z^2\}^{1/2}$ .

The set of Eqs. (1)-(7) formulates the exact boundary-value problem within the limitations of an ideal incompressible fluid. However, the nonlinear free-surface condition precludes any solution within the present linear framework. In the present linear approach we followed Dawson's approximation<sup>4</sup> that the disturbance due to free surface waves is small compared to the corresponding double-model solution. The total velocity potential is now expressed as the sum of two potential functions  $\Phi$  and  $\phi'$ .

$$\phi = \Phi + \phi' \quad (8)$$

where  $\Phi$  and  $\phi'$  are the double-model velocity potential and the disturbance potential due to free surface waves, respectively. Under the assumption that  $\phi'$  is small compared to  $\Phi$ , the free surface condition in Eq.(5) can be linearized with respect to  $\phi'$  such that

$$[ \Phi_x^2(\Phi_x^2 + \Phi_y^2)_x + \Phi_y^2(\Phi_x^2 + \Phi_y^2)_y + 2\Phi_x(\Phi_x\phi'_x + \Phi_y\phi'_y) + 2\Phi_y(\Phi_x\phi'_x + \Phi_y\phi'_y) + \phi'_x(\Phi_x^2 + \Phi_y^2) + \phi'_y(\Phi_x^2 + \Phi_y^2) ] + g\phi'_z = 0 \quad \text{on } z = 0 \quad (9)$$

$$\zeta = (1/2g)[U^2 - \Phi_x^2 - \Phi_y^2 - 2\Phi_x\phi'_x - 2\Phi_y\phi'_y] \quad \text{on } z = 0. \quad (10)$$

The simplified form of the linearized free surface condition expressed in terms of double-model streamline coordinates is written as

$$(\phi_1^2 \phi_1)_1 + g \phi_z = 2 \phi_1^2 \phi_{11} \quad \text{on } z = 0 \quad (11)$$

$$\zeta = (1/2g)[U^2 + \phi_1^2 - 2 \phi_1 \phi_1] \quad \text{on } z = 0 \quad (12)$$

where  $l$  denotes the double-model streamline coordinate and subscript  $l$  the derivative along the  $l$ -direction. The mathematical formulation then consists of the Laplace equation, Eq. (1), with the boundary conditions of Eqs. (2) and (11) on a truncated region of the free surface near the ship, and Eq. (7). Equation (12) is used for the wave height computation.

## NUMERICAL METHOD

The method used here is a boundary element method in which simple Rankine sources are distributed across each panel. The boundary-value problem formulated above then reduces to a determination of an unknown singularity distribution over the boundary surface of the fluid domain. Once singularity distribution is determined as the solution, the hydrodynamic quantities of interest, the velocity and the pressure, are also determined. The integration of the hull surface pressure gives forces and moments on the ship.

The new and original features of the present approach are summarized as follows:

1. The geometry of all the boundary surfaces is patched by quadratically varying curved panels instead of flat panels.
2. Linearly varying sources or quadratically varying doublet singularities are distributed on the surface panel, while existing approaches use constant sources on each panel.
3. A new transom stern condition is used.
4. An automatic method of determining a truncated free surface region and a suitable density of free surface panels depending the Froude number is implemented.
5. A variety of graphical post-processors have been developed.

The following sections give a detailed description of the advantages of the present approach over conventional approaches.

## HIGHER-ORDER CURVED PANEL

We use curved panels instead of flat ones to patch the ship surface. Let  $S$  be a true surface element bounded by four corner points  $P1$ ,  $P2$ ,  $P3$ , and  $P4$  as shown in Fig. 2. We assume that  $S$  may be represented in the approximate form

$$\zeta(\xi, \eta) = \zeta_0 + \zeta_\xi \xi + \zeta_\eta \eta + \zeta_{\xi\xi} \xi^2/2 + \zeta_{\xi\eta} \xi\eta + \zeta_{\eta\eta} \eta^2/2 \quad (13)$$

where  $(\xi, \eta, \zeta)$  are orthogonal coordinates local to  $S$ . The six coefficients  $(\zeta_0, \zeta_\xi, \zeta_\eta, \zeta_{\xi\xi}, \zeta_{\xi\eta}, \zeta_{\eta\eta})$  are obtained by requiring that the approximate surface given by Eq. (13) pass through its four corner points exactly and through its neighboring points approximately in a least squares sense. That is, for each panel the expression

$$R = 1/2 \sum_{j=1}^N W_j [\zeta(\xi_j, \eta_j) - \zeta_j]^2 \quad (14)$$

is minimized with respect to the six unknown coefficients appearing in Eq. (13). The summation in Eq. (14) ranges over the  $N$  neighboring grid points. The choice of the  $N$  points and the weights  $W_j$  has been made in an attempt to minimize any irregularities that may appear in the paraboloid approximation of the true surface. In the present formulation the values  $N = 9, 12$ , or  $16$  and  $W_j = 1$  or  $10^8$  are used depending on the location of the panel in the surface panel network. A typical 3-D perspective view of the surface panel network is shown in Fig. 3. Here we use the term network to represent the collection of quadrilaterals. The use of curved panels reduces the geometric discontinuity (leakage) experienced by the usual faceted flat panel approximations. Furthermore, the choice of these features is required by the argument given by Hess,<sup>2</sup> that certain computing methods which use flat panels do not obtain increased accuracy over the basic zero-order method (constant source on flat panels) even though they use higher-order source distributions. It is shown by Johnson<sup>5</sup> that for purposes of computational efficiency Eq. (13) can be reduced by an appropriate coordinate transformation to the canonical form



$$\zeta = a\xi^2 + b\eta^2 \quad (\xi, \eta) \in \Sigma \quad (15)$$

where  $\Sigma$  is the quadrilateral formed by the projection of the corner points on the  $(\xi, \eta)$  plane. In the case of a flat panel,  $a$  and  $b$  are both zero.

Let

$$\delta = 1/2 \text{Max} \{ a^2 \xi^2 + b^2 \eta^2 \}^{1/2}, \quad (\xi, \eta) \in \Sigma \quad (16)$$

and assume that

$$\delta \ll 1.0. \quad (17)$$

Physically, this assumption implies that the surface paneling is fine enough to assume a small ratio of the height to the maximum diameter of the panel. Under this assumption the integrals associated with the induced potentials and velocities are expressible as integrals in the  $\Sigma$ -plane, and all the resultant influence coefficients are obtainable in closed form. Furthermore, all the influence coefficients associated with the higher-order curved panel method can be computed from the corresponding integrals pertinent to the zero-order flat panel methods. Since these additional computations are carried out through a linear recursion relationship, the extra effort is minimal. The justification of this approximation was given by Johnson.<sup>5</sup> His numerical tests suggested that  $\delta < 0.066$  ensures a sufficiently fine paneling, and that a coarser paneling with a higher ratio gives results with less accuracy.

The distribution of singularity strengths on a panel  $S$  is assumed to be linear in the case of a source network and quadratic in the case of a doublet network. Specifically, we assume that the singularity strengths  $\sigma$  and  $\tau$  at a point  $(\xi, \eta, \zeta)$  on a panel  $S$  are given by

$$\text{Source: } \sigma(\xi, \eta) = \sigma_0 + \sigma_\xi \xi + \sigma_\eta \eta \quad (18)$$

$$\text{Doublet: } \tau(\xi, \eta) = \tau_0 + \tau_\xi \xi + \tau_\eta \eta + 1/2 \tau_{\xi\xi} \xi^2 + \tau_{\xi\eta} \xi\eta + 1/2 \tau_{\eta\eta} \eta^2. \quad (19)$$

The coefficients in Eqs. (18) and (19) are determined by using a method of weighted least squares over the panel and up to eight of its neighboring panels. This method requires that the form of Eq. (18) or (19) gives exactly the singularity value at its centroid and approximate values in the least square sense at centroids of the neighboring panels, as shown in Fig. 4. Since the singularity strengths are not known a priori, these coefficients are obtained as linear combinations of the unknown singularity values at discrete centroidal points. For each panel L there exists a relationship,

$$\begin{Bmatrix} \sigma_0 \\ \sigma_\xi \\ \sigma_\eta \end{Bmatrix}_L = [B]_L \begin{Bmatrix} \sigma_1 \\ \sigma_2 \\ \sigma_3 \\ \sigma_4 \\ \sigma_5 \\ \sigma_6 \\ \sigma_7 \\ \sigma_8 \\ \sigma_9 \end{Bmatrix}_L \quad (20)$$

Here the subscript L identifies the panel of interest and the subscripts 1,2, 3,....,9 the local panel indices associated with the panel L.

The sole reason for this least squares procedure is to express the assumed panel singularity distribution in terms of a neighboring subset of the unknown singularity, such that this approach requires no additional control points to those used in a constant-source, flat-panel method. It still gives the full power of the higher-order singularity method.

#### INDUCED POTENTIAL AND VELOCITY

Now the velocity potential at  $P=(x,y,z)$  induced by a singularity distribution on S is given by

$$\text{Source: } \phi = (-1/4\pi) \iint (\sigma/R) ds . \quad (21)$$

$$\text{Doublet: } \phi = (-1/4\pi) \iint \tau(\vec{R} \cdot \vec{n}/R^3) ds . \quad (22)$$

where

$$\vec{R} = (\xi-x, \eta-y, \zeta-z) = \vec{Q} - \vec{P} . \quad (23)$$

$$R = |\vec{R}| = \{ (\xi-x)^2 + (\eta-y)^2 + (\zeta-z)^2 \}^{1/2} . \quad (24)$$

and  $\sigma$  and  $\tau$  are given in Eqs. (18) and (19), respectively.

The velocity vector  $\vec{V}$  induced at  $P$  is given as the gradient of the corresponding velocity potential, i.e.,

$$\vec{V} = \vec{\nabla} \phi . \quad (25)$$

We are now in a position to evaluate the integral Eqs. (21), (22), and (25). From the relations of Eqs. (15), (17), (18), and (19) the induced velocity potential at  $P(x,y,z)$  due to the singularity distribution on the panel  $L$  can be expanded in closed form by using a combination of closed form calculations and recursive relationships. Details are fully included in Johnson's report<sup>5</sup> and in Appendix A.

## NUMERICAL APPROXIMATION OF THE FAR-FIELD BEHAVIOR OF THE SOLUTION

In the present approach a finite computational domain is used for the numerical computation by truncating the infinite fluid domain at a finite distance from the ship. If the truncation boundary is located sufficiently far from the ship, so that the contribution resulting from this truncated region is negligible, this numerical approximation can be justified. However, unless we specify legitimate boundary conditions on this far boundary, the solution of the boundary-value problem is not unique and the numerical solution cannot be justified. In order to render the boundary-value problem unique, or alternatively to ensure that the waves associated with the disturbance appear only downstream, three-point or four-point upstream difference schemes have been commonly used for the approximation of the terms  $\phi_{||}$  and  $(\phi_{||}^2 \phi_{||})_1$  in Eq. (11).

$$(\partial\omega/\partial l)_i = C4_i\omega_i + C4_{i-1}\omega_{i-1} + C4_{i-2}\omega_{i-2} + C4_{i-3}\omega_{i-3} \quad (26)$$

or

$$(\partial\omega/\partial l)_i = C3_i\omega_i + C3_{i-1}\omega_{i-1} + C3_{i-2}\omega_{i-2} \quad (27)$$

where the coefficients C4 and C3 are given by

$$C4_{i-1} = -dl_{i-2}dl_{i-3}(dl_{i-3}-dl_{i-2})/D4 \quad (28)$$

$$C4_{i-2} = dl_{i-1}dl_{i-3}(dl_{i-3}-dl_{i-1})/D4 \quad (29)$$

$$C4_{i-3} = -dl_{i-1}dl_{i-2}(dl_{i-2}-dl_{i-1})/D4 \quad (30)$$

$$C4_i = -(C4_{i-1} + C4_{i-2} + C4_{i-3}) \quad (31)$$

where

$$D4 = dl_{i-1}dl_{i-2}dl_{i-3}(dl_{i-3}-dl_{i-1})(dl_{i-3}-dl_{i-2})(dl_{i-2}-dl_{i-1})(dl_{i-1}+dl_{i-2}+dl_{i-3}), \quad (32)$$

or

$$C3_i = (dl_{i-2}-dl_{i-1})/D3 \quad (33)$$

$$C3_{i-1} = -dl_{i-2}/D3 \quad (34)$$

$$C3_{i-2} = dl_{i-1}/D3 \quad (35)$$

where

$$D3 = dl_{i-1}dl_{i-2}(dl_{i-1}+dl_{i-2}) \quad (36)$$

and

$$dl_{i-k} = l_i - l_{i-k} \quad (37)$$

This upstream finite difference scheme for the free-surface boundary condition introduces numerical dissipation into the physical problem to ensure only downstream waves. However, the extent of this numerical

dissipation depends on the panel sizes and on the free-surface panel arrangement so that it is hard to control or to estimate. Furthermore the upstream difference scheme introduces unnecessary numerical dispersion into the physical problem. An alternative way to ensure no upstream waves is to introduce explicitly an artificial viscosity, known as Rayleigh viscosity, so that the numerical dispersion due to the difference scheme can be avoided. The corresponding free-surface boundary condition becomes

$$\begin{aligned}
 & [ \phi_x^2 \psi_{xx} + 2\phi_x \phi_y \psi_{xy} + \phi_y^2 \psi_{yy} + 2(\phi_x \phi_{xx} + \phi_y \phi_{xy}) \psi_x + 2(\phi_x \phi_{xy} + \phi_y \phi_{yy}) \psi_y ] \\
 & + \nu [(2\phi_x + 1) \psi_x + 2\phi_y \psi_y] + g \psi_z \\
 & = 2[ \phi_x^2 \phi_{xx} + 2\phi_x \phi_y \phi_{xy} + \phi_y^2 \phi_{yy} + \phi_x \phi_{xx} + \phi_y \phi_{xy} ] + \nu [(\phi_x + 1)^2 + \phi_y] \quad (38)
 \end{aligned}$$

where  $\nu$  is a small positive Rayleigh viscosity term and  $\psi$  is the disturbance potential such that  $\phi = -Ux + \psi$ . The derivative terms in Eq. (38) are evaluated analytically through the recursion relationship with minor additional computations. The dissipation introduced by an artificial Rayleigh viscosity should be small enough not to damp the solution too much.

The radiation condition of no waves upstream is imposed to make the solution unique. If we had applied appropriate boundary conditions on this far-field truncation boundary to ensure uniqueness, the approximate procedures could have been avoided. A physically acceptable uniqueness condition is the condition of no waves at the upstream truncation boundary. That is,

$$\psi_x = 0 \quad (39)$$

$$\psi_{xx} = 0. \quad (40)$$

Once the singularity distributions are determined as the solution of the boundary-value problem formulated above, the hydrodynamic pressure coefficient can be obtained from the Bernoulli equation

$$C_p = p/(1/2 \rho U^2) = 1 - V^2/U^2. \quad (41)$$

A linear distribution of  $C_p$  on each panel can be calculated from the values of  $C_p$  at the control points. The

method used is identical to that for computing the linear source distribution network. On any panel  $S$ , we then have

$$C_p(\xi, \eta) = C_{po} + C_{p\xi}\xi + C_{p\eta}\eta. \quad (42)$$

The force coefficient vector  $\vec{C}_F$  on  $S$  is defined by

$$\vec{C}_F = (1/S) \iint C_p(\xi, \eta) \vec{n}(\xi, \eta) ds \quad (43)$$

where  $S$  is a specified reference area. After algebraic manipulations, we obtain the following expression for  $\vec{C}_F$  in local coordinates:

$$\begin{aligned} \vec{C}_F = (1/S) \{ & -2a[ C(2,1)C_{po} + C(3,1)C_{p\xi} + C(2,2)C_{p\eta} ] \\ & -2b[ C(1,2)C_{po} + C(2,2)C_{p\xi} + C(1,3)C_{p\eta} ] \\ & [ C(1,1)C_{po} + C(2,1)C_{p\xi} + C(1,2)C_{p\eta} ] \zeta \}. \end{aligned} \quad (44)$$

## IMPLEMENTATION OF NUMERICAL SOLUTION

The present method uses a discrete panel method to achieve a numerical solution of the boundary-value problem. More specifically, the problem is reduced to the determination of unknown singularity strengths at discrete centroidal points on each panel. A finite set of control points (equal in number to the number of unknown singularity strengths) is selected at which the boundary conditions are imposed. Application of the boundary conditions results in a finite set of simultaneous algebraic equations denoted symbolically by

$$[A] \{X\} = \{B\}. \quad (45)$$

Here,  $\{X\}$  is the vector of unknown singularities,  $\{B\}$  is the vector of specified boundary conditions, and  $[A]$  is the square matrix of influence coefficients.  $A_{ij}$  represents the influence of the  $j$ -th singularity  $X_j$  on the boundary condition at the  $i$ -th control point.

While the solution of Eq. (45) may be obtained by using any available numerical algorithm, we have paid particular attention to the techniques of numerical linear algebra in this research. The part of the matrix resulting from the ship hull surface boundary condition is diagonally dominant, which has led many researchers to use iterative methods analogous to aerodynamic computations. When the linearized free surface conditions are added for the study of free surface flows, this diagonal dominance is lost. It is common for research purposes to solve free surface flows at a number of different ship velocities without altering the paneling with fixed sinkage and trim. Letting the number of body surface panels, free surface panels, and the total panels be denoted by NBP, NFP, and NTOT, it is easy to see that the resulting matrix is of size

$$(NTOT)^2 = (NBP + NFP)^2. \quad (46)$$

This matrix may be partitioned as

$$[A] = \begin{bmatrix} A_{BB} & A_{BF} \\ A_{FB} & A_{FF} \end{bmatrix}. \quad (47)$$

Only the submatrices  $A_{FB}$  and  $A_{FF}$  change with ship speed,  $A_{BB}$  and  $A_{BF}$  being generated from the no-penetration condition on the wetted hull surface. A partitioned matrix solution technique can be devised to eliminate a large number of redundant calculations, requiring matrix work only on  $A_{FB}$  and  $A_{FF}$ . A major benefit of this partitioned matrix approach is that only the submatrices need to be in core at any given stage of computation, which greatly increases the number of ship surface panels and especially the number of free surface panels available to the user. All the experience of the aerodynamic researchers has indicated an increasing demand for more panels to enable the study of more complicated geometries. In naval applications also a large number of free surface panels is often desired and a total of around 1000 can be a serious limitation. With the program developed here, the only limitations on size are that number of the body surface panels and the free surface panels must each individually be not more than 900 for use on a CRAY X-MP/12, and this limit increases to over 1400 on a CRAY X-MP/24 such as is available at DTRC. Thus the total

number of panels will be between 1800 and 2800 on the CRAY X-MP family of supercomputers, depending on available memory sources.

Partitioning the solution vector  $\{X\}$  and the right-hand side vector  $\{B\}$  in a compatible way gives the total partitioned matrix equation

$$\begin{bmatrix} A_{BB} & A_{BF} \\ A_{FB} & A_{FF} \end{bmatrix} \begin{bmatrix} X_B \\ X_F \end{bmatrix} = \begin{bmatrix} B_B \\ B_F \end{bmatrix} \quad (48)$$

This equation reduces to

$$[A_{FF} - A_{FB} [A_{BB}^{-1} A_{BF}]] \{X_F\} = \{B_F\} - A_{FB} [A_{BB}^{-1} B_B] \quad (49)$$

with  $X_B$  being given by an almost no-cost calculation as

$$\{X_B\} = (A_{BB}^{-1} B_B) - [A_{BB}^{-1} A_{BF}] \{X_F\}. \quad (50)$$

Note that  $A_{BB}^{-1} A_{BF}$  and  $A_{BB}^{-1} B_B$  can be computed just once so that the only new work of consequence needed for additional ship speed cases is the above matrix times matrix multiplication and a factorization of the modified NFP by the NFP free surface matrix in Eq. (49). If the solution for only one Froude number is required, the total operation count is the usual  $(NTOT)^3/3$  exactly as when no partitioning is used, except that the operations for the  $A_{BB}$  factorization are not repeated.

We have also implemented and extended some very recent advances in squeezing supervector speed out of matrix multiplication and factorization routines recently developed by Dongarra and Eisenstat.<sup>6</sup> This procedure improved the vectorization in the present numerical code so much that the resulting factorization times in portable FORTRAN were significantly better than the previously used LINPACK-based code optimized in assembly language.

Numerous other vectorization techniques were used which were variations on the theme of creating large inner loops. In some cases reorganizing algorithms actually decreased the number of operations significantly. For example, a combination of both techniques decreased the computer time spent in the computation of the



far-field approximation of influence coefficients by a factor of 85. An example of the first technique arises in the typical computation

$$\text{TRJO}_K = \text{TRJO}_K + C * \text{TRJ}_K, \quad 1 \leq K \leq N \quad (51)$$

where  $C$  is a fixed 3 by 3 coordinate transformation matrix and  $\text{TRJ}_K$  and  $\text{TRJO}_K$  are 3 by 3 matrices. This calculation is routinely performed in the middle of a large  $K$ -loop by calling on a utility routine  $\text{MXM}$  to perform the 3 by 3 matrix multiplication of  $C$  times  $\text{TRJ}_K$ . The code can be reorganized so that the  $K$ -loop is around just this calculation, and a vector subroutine can be created with the result given by nine hand-coded dot products of vectors of length 3. One of the nine FORTRAN lines would read

$$\text{TRJO}(1,1,K) = \text{TRJO}(1,1,K) + C(1,1)*\text{TRJ}(1,1,K) + C(1,2)*\text{TRJ}(2,1,K) + C(1,3)*\text{TRJ}(3,1,K).$$

This new routine with the key calculation inside a large loop is so efficient that it decreases the computer time for vectors of length  $K$  around 250 or larger by a factor of 15. The current code is now well structured for inclusion of new modeling approaches and is over 90 percent vectorized for extremely efficient use on Class VI and Class VII supercomputers. It consists of about 12,000 lines of FORTRAN, 40 percent of which are comments.

## TRANSOM STERN

Most Navy high speed combatant ships have transom sterns and at high speed the flow clears the stern completely. To model this unwetted transom flow, one suggested approach is to add a cruiser stern-like extension behind the transom stern and apply the boundary condition  $\phi_n \approx 0$  on the transom section. This approach has given results that compare poorly with experimental data. Adequate numerical modeling of the *transom stern* condition is challenging within the framework of the linearized free surface potential flow theory. In the basic formulation assumptions have been made that the disturbance created is small enough to allow the linearization of the free surface condition about the undisturbed free surface  $\zeta = 0$ . Several variations

of numerically modeling have been attempted. The version currently in the program provides the most reasonable results compared with experimental values. In this approach, we removed the transom stern part from the hull geometry input data, creating is a hole at the stern of a ship in the sense that the hull is not completely closed. Along the first row of bottom panels adjacent to the transom stern, the hull surface boundary condition  $\phi_n = 0$  was replaced by the requirement that the flow pass by each panel tangentially. The magnitude and angle of tangential velocity were obtained by extrapolating values from neighboring panels. The free surface behind the transom exists at  $z = 0$  so that the linearized free surface condition is satisfied. This numerical model has been tested on the Athena hull form and on several combatant ships.

### CONVERGENCE TEST OF NUMERICAL SOLUTION

In addition to the difficulty experienced in the numerical implementation of the radiation condition, there exist numerous sources of computational uncertainties, such as (1) numerical differentiation and integration, (2) truncated domain from infinite to finite, and (3) panel size. Furthermore these sources of errors are interwoven in a complicated manner. It is not possible to separate and quantify simply each source of error. Three main attributes generate traceable errors: (1) fore- and aft- truncation boundary, (2) side truncation boundary, and (3) number of panels for a given finite domain. These attributes are examined separately below. A Wigley parabolic hullform in Fig. 5 was used for this numerical convergence experiment.

#### Fore and Aft Truncation

Fore and aft truncation boundaries are always taken the same distance from FP(forward perpendicular) and AP(aft perpendicular) of the ship, respectively. Their ranges are approximately between  $1.5L$  and  $3.2L$  where  $L$  is the half of the ship length,  $L=LWL/2$ . Froude numbers considered were between  $0.2$  and  $0.375$ . The side boundary was fixed at  $y=1.0L$ . The relative error is defined as

$$\text{Relative Error} = \frac{[C_w \text{ (at } x=x_i) - C_w \text{ (at } x=3.2L)]}{C_w \text{ (at } x=3.2L)}$$

where  $C_w$  is the wave resistance coefficient and  $x_i = 1.46L, 1.9L, 2.2L, 2.9L$ , and  $3.2L$ . The results are

plotted in Fig. 6. The maximum relative error is about 2% and decreases proportionally with increasing distance of the truncation boundary. For this Froude number range, the truncation boundary  $x=2.5L$  seems sufficiently far away to provide stable results.

#### Side Truncation

The examined side truncation boundaries were located between  $0.5L$  and  $1.6L$  from the ship's centerline. Fore- and aft- boundaries were fixed at  $x=2.0L$  and the same Froude number range was considered. The relative error is defined similarly as

$$\text{Relative Error} = \frac{[C_w \text{ (at } y=y_i) - C_w \text{ (at } y=1.6L)]}{C_w \text{ (at } y=1.6L)}$$

where  $y_i = 0.53L, 1.0L, 1.25L$ , and  $1.6L$ . Figure 7 shows the results. The observed maximum error is about 2.5% and decreases linearly with the distance of the boundary. The differences are hardly distinguishable when  $y$  is more than  $1.25L$ .

#### Panel Size

The last parameter considered is the panel size or number of panels for a fixed domain. The computational domain was fixed at  $x=2.0L$  fore and aft and  $y=1.0L$ . The total number of panels for both body and free surface varied from 612 to 1052. Figure 8 shows the relative error which is the ratio between the difference of  $C_w$  at 612, 700, 800, 860, 950, and 1052 panels and  $C_w$  of 1052 panels. The maximum error is about 4%. The error decreases rapidly to about 1% between 600 and 700 panels, and at more than 700 panels the rate of decrement is very slow compared with the rate of increment in panel numbers. It appears that, once the primary variation is obtained, the effect of further refinement of the panel size is not significant. In problems of this type, with abrupt changes in the boundary conditions (hull-free surface interface) or geometry, there is a singularity in the solution within a local neighborhood. This singularity leads to the slow convergence of the solution. Typically a halving of the panel size (which increases the work by a factor of 4) might produce only a 40% improvement in the error. In recent work, Lucas and Oh<sup>\*</sup> formulated a new approach to this problem

---

\* "The Method of Auxiliary Mapping and the Finite Element Solution of Elliptic Boundary Value Problem Containing Boundary or Corner Singularities," submitted to IMA J. of Numerical Analysis.

which has promise for a generalization to the 3-dimensional problem. For the moment, however, about all that can be said is that a medium-sized grid gives sufficient resolution. Without a new and different approach, further refinement is probably too costly to be effective.

## RESULTS AND DISCUSSION

The first step of the panel method approach is to discretize the fluid boundary in the form of panel networks. These networks are a collection of either source or doublet panels and are independently defined over various portions of the ship hull and the free surface as illustrated in Fig. 9. Once this panel discretization has been completed, the solution of the boundary-value problem can be carried out.

### SPHERE

The first test case is an unbounded potential flow about a sphere in a uniform stream. The solution is well known analytically. This choice was made to examine the capability of the present approach versus that of the zero-order flat-panel approach. There is symmetry of the flow about two planes so that only a quarter of the sphere needs to be paneled. To test the flexibility of the panel method we used two different panel arrangements as shown in Fig. 10: a regular paneling and a random paneling. The corner points for random panels were chosen using a random number generator, which led to a wide variation in panel size and shape; the corner points of regular panels were generated using cosine spacing along the x-direction and uniform spacing along the transverse direction. Velocity potentials at each of the 12x4 control points are plotted in Fig. 10 as a function of the x-coordinate. Agreement with the exact solution is good. This example demonstrates the extreme forgiveness of the method to irregular paneling, a feature which greatly enhances the method's practical utility for applications involving much more complex configurations. The accuracy and the convergence rate of the method are also compared with those of the zero-order flat panel approach. The results, summarized in Table 1, show the superiority of the present higher-order curved panel method over the conventional zero-order flat panel method in both accuracy and convergence rate: the present method gives a convergence rate of  $O(h^2)$ .

while the rate of the conventional method is only  $O(h)$ . Here  $h$  denotes a characteristic length scale of the panel.

The results in Table 1 for the zero-order flat panel approach were obtained as the special limiting solutions of the present higher-order curved panel code. Numerical tests showed that the zero-order flat panel solutions from the present code are exactly same as those from an existing zero-order code.<sup>2</sup>

#### WIGLEY HULL

The Wigley hull is a mathematical hull with a parabolic waterline and parabolic cross section. The equation used for the surface is

$$y = (1-x^2)(1-z^2/64)/10, \quad (52)$$

and the particulars and body plans are given in Fig. 5. Six Froude numbers, 0.25, 0.267, 0.289, 0.316, 0.354, and 0.408, were considered. Extensive numerical tests revealed that the extent of the paneled part of the free surface must be determined on the basis of the wavelength of the generated waves as well as on the hull configuration. Numerical tests suggest that a finite free surface region, extending one wavelength upstream from the bow, one wavelength downstream from the stern, and  $3/4$  ship length from the centerline to the side, is sufficient to approximate an unbounded free surface to the desired accuracy.

It is a common practice in the field of computational fluid dynamics to verify the accuracy of a numerical solution by systematically varying panel densities and then examining the resulting convergence characteristics. Systematic variations of panel densities on the wetted hull surface and on the free surface were investigated for this mathematical hull form. During these numerical tests the upstream finite difference operator given in Eq. (26) or (27) was used to approximate the radiation condition numerically. The effect of the free surface panel density on the numerical solution was then tested by changing the densities in the lateral and longitudinal directions. It was found that the numerical results were more sensitive to the variation of the free surface panel density than to the body surface panel density. This sensitivity may be explained in two ways. First, the free surface boundary condition is of mixed type involving tangential velocities as well as normal velocities, while

the body boundary condition is of Neumann type involving only velocities normal to the boundary. Secondly, we use the upstream finite difference operator to compute the streamwise derivatives of the tangential velocities in the free surface condition. This operator is used to eliminate upstream disturbances numerically. It is well known that the accuracy of the finite difference operation depends on the size of the basic element. Furthermore, the artificial numerical damping involved in a specific upstream finite difference operation is expected to vary with the free surface panel densities.

In the present report, we used for the higher-order panel approach a linearly varying source distribution on the curved ship hull and a quadratic doublet distribution on the free surface. In order to satisfy the free surface condition a three-point upstream finite-difference and a four-point upstream finite difference operator were used for the higher-order panel approach and the zero-order panel approach, respectively. The ship hull surface was defined using 192 panels (24x8), and 624 panels (52x12) were used to represent the truncated free surface domain. In Figs. 11 through 17, the computed wave profiles and wave-making resistance results, are compared with the measurements reported by the Resistance Committee of the 17th ITTC(International Towing Tank Conference).<sup>7</sup>

To facilitate comparisons, the following non-dimensionalization has been made:

$$C_W(\text{Wave-making resistance coefficient}) = \text{Resistance}/(1/2 \rho U^2 S)$$

$$\bar{\zeta}(\text{Wave profile}) = \zeta/(U^2/2g)$$

where  $U$  is the forward speed,  $g$  the gravitational acceleration, and  $S$  the wetted surface area. Generally speaking, the advantage of the higher-order panel approach is not evident in these numerical results to the same extent that the results for the unbounded potential flow show the advantage of the higher-order panel approach over the zero-order panel approach. The numerical results shown in the Figs. 11 through 17 suggest that a fair comparison of approaches must be made without using an approximate scheme (upstream-finite difference operator) which induces numerical errors that cannot be estimated easily. The alternative approaches using Eqs. (38) or (39) and (40) instead of the upstream-finite difference operator are expected to provide fair

comparisons and to show the superiority of the higher-order approach even for the free-surface flow problems. Figure 18 shows 3-dimensional perspective view of waves generated by Wigley hull at  $F_n = 0.408$ . Wave contour plot is shown in Fig. 19.

#### SERIES 60, $C_B = 0.60$

The body plan and profile drawings of the cruiser stern Series 60,  $C_B = 0.60$  hull form are shown in Fig. 20 and the table of offsets is provided in Table 2. In this case, the ship hull surface was defined using 360 panels (30x12), and 696 panels (58x12) were used for the truncated free surface. Figures 21 through 26 show the measured and the computed wave profiles compared at six Froude numbers: 0.20, 0.25, 0.30, 0.32, and 0.35. At the forward half of hull the computed wave profiles compare favorably with the measured ones, but the agreement becomes poorer downstream. The prediction always overestimates the magnitude of the last crest. The discrepancy near the stern may be explained partially by the fact that growth of a thick boundary layer violates the underlying assumption of potential flow, and the nonlinear free surface condition should be taken into account in order to make improvement. Note that the comparison between the computation and experiment for the Series 60 hull is different from the Wigley hull case in which the prediction always underestimates the magnitude of the bow crest and shows good agreement in the aft part.

In Fig. 27, the calculated wave-making resistance coefficients are compared with the experimental results of Kim and Jenkins.<sup>8</sup> It is interesting to note that for both the Wigley and Series 60 hulls the differences between the measured and the computed wave profiles are relatively small, but the discrepancy in wave-making resistance between theory and experiment is much greater than expected. As is well known, most of the wave-making resistance comes from the difference between the integrated longitudinal pressure forces at the bow and at the stern. Particularly in these two areas, the observed flow seems to violate the underlying assumptions for linearized potential-flow theory. In Fig. 28 the computed longitudinal wave cut was compared with the measured one at  $y/(L/2) = 0.7521$  and  $F_n = 0.323$ . Near and aft of the stern the wave phase is shifted slightly, but the amplitude shows excellent agreement between calculated and experimental results.

## ATHENA HULL

A body plan of the round bilge, semi-planing high speed ship hull of the Athena is shown in Figs. 29 and 30, and the offsets are given in Table 3. The hull was represented by 23 by 8 panels. The transom stern and free surface region behind the transom stern were considered as a special section in the computation. A total of 489 panels was used to cover the whole free surface: 48x8 panels for the main portion of the free surface and 15x7 panels for the free surface behind the transom stern. As mentioned previously the transom stern segment of the body geometry is left unpaneled and a tangential condition was satisfied at the last row of panels of the hull. Four Froude numbers, 0.350, 0.412, 0.484, and 0.651, were selected from among the test runs of the ITTC Resistance Committee,<sup>7</sup> and the measured wave profiles were compared with the computed ones in Figs. 31 - 34. At lower Froude numbers a discrepancy is noticeable, especially aft of midship. The computational results show a deeper trough than do the experimental data. Furthermore up to Froude number 0.412 we see a kink in the wave profile very near the stern which does not exist in the experimental results. This peculiar result at lower Froude numbers may come from the transom boundary condition incorporated here, since at lower speeds the transom stern is not completely dry. As speed increases, this phenomenon disappears completely and the predicted wave profiles smoothly follow the measured ones along the entire hull. These numerical results indicate that the suggested transom stern boundary condition is well suited to higher Froude numbers (i.e., dry transom stern), but for lower Froude numbers we will have to develop a wetted transom version of the stern boundary condition.

Figure 35 shows the wave profiles behind the stern of the ship at two different locations:  $y/(L/2) = 0.027$  and 0.054 for  $F_n = 0.484$ . The computed and measured results show excellent agreement.

## LARGE COMBATANT SHIPS

As part of an intensive program to study the wave systems generated by a large combatant ship, DTRC conducted model tests for three similar hull configurations: Models X, A, and C (see Beaver's report<sup>9</sup>). The purpose of the testing was to study the effects of hull shape changes on the wave generation characteristics.



Figure 36 shows a comparison of body plans for Model X and Model A. Model X is the existing configuration and Model A identifies the notched-hull configuration in which the 7.5-foot wide notch extends the length between stations 3.7 and 18.8 at the designed waterline. The body plan of Model C is compared with that of Model A in Fig. 37. Model C identifies a modification of Model A that incorporates only the removal of volume from the shoulder region between stations 4 and 10. Hull form characteristics of Models X, A, and C are given in Table 4.

The wave profiles along the hulls were measured at  $F_n = 0.179, 0.238, \text{ and } 0.298$  between stations 0 and 8 for each configuration. In Figs. 38, 39, and 40 the computed and measured wave profiles are plotted together to make comparison easier between Models X and A at each speed. In Figs. 41, 42, and 43 the same comparisons are shown for Models A and C. As shown in these figures, the computed results agree well with the measured ones for all three models and for all speeds considered, except near the bow region.

Off-body wave elevations for Models X and A were measured at  $F_n = 0.238$  using five capacitance wire wave probes mounted transversely across the basin. As shown in Fig. 44, the probe locations were approximately 77, 90, 102, 120, and 135 ft ship scale off the centerline of the ship. The comparisons between the computed and measured off-body longitudinal wave elevations at each probe were plotted in Figs. 45 through 49 and their agreements are excellent.

## COMPARISON WITH OTHER APPROACHES

DTRC organized a special workshop called "Wake-Off"<sup>10</sup> which was held on 12 and 13 January 1988. The objective of this workshop was to gather all available numerical codes that may be useful for predicting or evaluating ship generated waves, wave spectra, wave contour, wave pattern, and wave-making resistance and to make comparative evaluation of results of these codes for given specific ships and speeds. Two models, DDG51 and QUAPAW, were selected and their offsets, particulars, and specific Froude numbers were provided to each participant. DTRC conducted model tests at the same time, but the test data were not disclosed to the participants. This closure provided a blind test for predictive capability of the various computational approaches. Twelve computer programs were involved in this workshop: five from DTRC, two from

SAIC(Science Application International Corporation), one each from University of Michigan, Lockheed, SSPA Maritime Consulting, MIT(Massachusetts Institute of Technology), and Rosen(Engineering Consultant). It was interesting to see that only two methods, the Havelock source and the Rankine source method, were used among them. Five computer codes use the Havelock source and the others use the Rankine source method.

Both methods consistently underpredicted the amplitude of the bow wave and overpredicted the amplitude of the stern wave. Overall, the Havelock source codes provided better results than the Rankine source codes, especially for the far field wake. Excellent near-field calculations were provided by the codes SWIFT and FLOPAN which use a higher order Rankine source and a constant source/doublet distribution method, respectively. These two codes outperformed the methods such as XYZFS which used the constant Rankine source. As already mentioned, the Rankine source method customarily adopts the upstream finite-difference operator to satisfy the free surface condition and the radiation condition, but the use of the upstream finite-difference operator is equivalent to introducing an artificial viscosity. This viscosity effect attenuates the wave amplitudes significantly as they propagate and the results get progressively poorer far downstream. There should be a strong effort to develop a computational method that combines the excellent near-field capability of the Rankine source method with the superior far-field behavior of the Havelock source method.

## CONCLUSIONS

A higher-order panel method for the linearized free-surface flow has been developed. The capability of the present higher-order curved panel method is summarized as follows:

1. The cost of curved higher order panels in the computation of the influence coefficients is not notably greater than the cost of flat constant source panels, because of the use of recursive relations from the flat constant case.
2. The results from the use of curved panel, linear source terms on the ship hull are robust with respect to the panel size and geometry.
3. The convergence rate for the double body case is  $O(h^2)$ , while the zero-order flat panel method gives  $O(h)$ .

4. The free surface calculations have been shown to be robust with respect to changes in the longitudinal and lateral free surface computational domain and with respect to the panel density.
5. New partitioned matrix techniques have been used to minimize storage requirements and allow the number of body and free surface panels to be up to 2800 panels.
6. Extensive use of advanced vectorization techniques has made the code highly efficient.
7. A new transom stern condition has been developed and implemented which gives excellent results for the tested models.
8. A number of tests with the Wigley hull, Series 60, ATHENA, and a large combatant hull have given excellent comparisons with measurements of wave profiles.
9. A new user-friendly preprocessor program has been developed by Mr. Steven Fisher of DTRC to provide input to SWIFT.
10. Two new postprocessors have been developed which give graphical results of both the wave height on the ship body and the contours of the wave heights over the computational region (see Robinson,\* for example)

## RECOMMENDATIONS

1. Since the wave-making resistance is a small quantity whose accuracy depends critically on the corresponding accuracy of numerical discretization, an approach other than a direct numerical integration of the pressure should be considered.
2. In order to fully exploit the superior potential of the present higher-order method over the zero-order approach, the free surface condition should be recast in a form which minimizes the artificial numerical dissipation and/or numerical dispersion.

---

\* Robins, C.R., "Ship Wave Color Graphics Using DI-3000." Computer Science Senior Project, U. of North Carolina at Charlotte, 1986.

3. An accurate prediction of near-field flow around a surface ship is essential for the prediction of wave breaking near the bow and/or stern, for investigation of pressure distributions (possibly cavitation inception) on a sonar dome, for tracing bubble sweep along the hull, and for the alignment of appendages. Since the local and nonlinear effects close to the hull surface are important, a nonlinear formulation of the free surface flow is needed for the accurate analysis. Commonly used surface singularity techniques for nonlinear free surface problems are based on the iteration of the unknown surface wave topology, in which the adjustment of the free surface shape obtained from the previous iteration is a crucial factor in the convergence and stability of the iterative solution. The present panel method allows the use of higher order curved panels which can closely approximate the actual surface topology. Further, the linear variation of surface singularity in the higher-order panel method enables self-induction effects to be included for each panel. The higher-order panel method is, therefore, expected to make the iteration solution more stable than that of existing lower order panel approaches. The nonlinear extension of the present numerical scheme will be the subject of separate, ongoing work.

### ACKNOWLEDGMENTS

The authors express their gratitude to Dr. Wen-Chin Lin of DTRC for his valuable suggestions and encouragement during the course of this work. The authors also thank Mr. Steven Fisher of DTRC for his continuous support in the development of pre-processor and post-processor software for the present analysis code.

**THIS PAGE INTENTIONALLY LEFT BLANK**

## APPENDIX A

### COMPUTATION OF VELOCITY POTENTIAL $\phi$

In this appendix we will evaluate the integrals of Eqs. (21), (22), and (25). With the relations of Eqs. (15), (17), (18), and (19), the induced velocity potential at  $\vec{P}(x,y,z)$  due to the singularity distribution on the panel L can be expanded as

$$\phi = \sigma_o I_\sigma(1,1) + \sigma_\xi [x I_\sigma(1,1) + I_\sigma(2,1)] + \sigma_\eta [y I_\sigma(1,1) + I_\sigma(1,2)] \quad (A1)$$

and

$$\begin{aligned} \phi = & \tau_o I_\tau(1,1) + \tau_\xi [x I_\tau(1,1) + I_\tau(2,1)] + \tau_\eta [y I_\tau(1,1) + I_\tau(1,2)] \\ & + (1/2) \tau_{\xi\xi} [x^2 I_\tau(1,1) + 2x I_\tau(2,1) + I_\tau(3,1)] + (1/2) \tau_{\eta\eta} [y^2 I_\tau(1,1) + 2y I_\tau(1,2) + I_\tau(1,3)] \\ & + \tau_{\xi\eta} [xy I_\tau(1,1) + y I_\tau(2,1) + x I_\tau(1,2) + I_\tau(2,2)]. \end{aligned} \quad (A2)$$

Here

$$\begin{aligned} I_\sigma(M,N) = & (-1/4\pi) \{ H(M,N,1) + a[hH(M+2,N,3) + 2xhH(M+1,N,3)] \\ & + b[hH(M,N+2,3) + 2yhH(M,N+1,3)] \\ & + c[hH(M,N,3)] \} \end{aligned} \quad (A3)$$

and

$$\begin{aligned} I_\tau(M,N) = & (1/4\pi) \{ hH(M,N,3) + a[H(M+2,N,3) + 3h^2H(M+2,N,5) + 6xh^2H(M+1,N,5)] \\ & + b[H(M,N+2,3) + 3h^2H(M,N+2,5) + 6yh^2H(M,N+1,5)] \\ & + c[-H(M,N,3) + 3h^2H(M,N,5)] \} \end{aligned} \quad (A4)$$

where

$$c = ax^2 + by^2 - z_o \quad (A5)$$

$$h = z - z_o \quad (A6)$$

$$z_0 = ax_0 + by_0 \quad (A7)$$

$$H(M,N,K) = \iint \frac{(\xi-x)^{M-1}(\eta-y)^{N-1}}{\rho^K} d\xi d\eta \quad (A8)$$

$$\rho = \sqrt{(\xi-x)^2 + (\eta-y)^2 + h^2} \quad (A9)$$

and  $(x_0, y_0, 0)$  is the point on  $\Sigma$  closest to  $(x, y, 0)$  (see Fig. 2). Since

$$(\partial/\partial x)H(M,N,K) = -(M-1)H(M-1,N,K) + KH(M+1,N,K+2)$$

$$(\partial/\partial y)H(M,N,K) = -(N-1)H(M,N-1,K) + KH(M,N+1,K+2)$$

$$(\partial/\partial z)H(M,N,K) = -KhH(M,N,K+2), \quad (A10)$$

the induced velocities are obtained as

$$\vec{V} = \sigma_0 \vec{J}_\sigma(1,1) + \sigma_\xi [x \vec{J}_\sigma(1,1) + \vec{J}_\sigma(2,1)] + \sigma_\eta [y \vec{J}_\sigma(1,1) + \vec{J}_\sigma(1,2)] \quad (A11)$$

where

$$\vec{J}_\sigma(M,N) = [J_{\sigma x}(M,N), J_{\sigma y}(M,N), J_{\sigma z}(M,N)] \quad (A12)$$

and

$$\begin{aligned} J_{\sigma x}(M,N) = (-1/4\pi) \{ & H(M+1,N,3) + 3ah[H(M+3,N,5) + 2xH(M+2,N,5)] \\ & + 3bh[H(M+1,N+2,5) + 2y(M+1,N+1,5)] \\ & + 3ch[H(M+1,N,5)] \} \end{aligned} \quad (A13)$$

$$\begin{aligned} J_{\sigma y}(M,N) = (-1/4\pi) \{ & H(M,N+1,3) + 3ah[H(M+2,N+1,5) + 2xH(M+1,N+1,5)] \\ & + 3bh[H(M,N+3,5) + 2yhH(M,N+2,5)] \\ & + 3ch[H(M,N+1,5)] \} \end{aligned} \quad (A14)$$

$$\begin{aligned}
J_{\sigma_z}(M,N) = & (-1/4\pi) \{ -hH(M,N,3) + a[H(M+2,N,3)-3h H(M+2,N,5)] \\
& + 2xH(M+1,N,3)-6xh H(M+1,N,5)] \\
& + b[H(M,N+2,3)-3h H(M,N+2,5)] \\
& + 2yH(M,N+1,3)-6yh H(M,N+1,5)] \\
& + c[H(M,N,3)-3h H(M,N,5)] \} . \quad (A15)
\end{aligned}$$

The corresponding expressions for the induced velocities due to doublet can be obtained easily by differentiating Eq. (A2) and then using the relations of Eq. (A10).

If the field point  $P(x,y,z)$  is located at a large distance from the panel surface  $S$ , the expressions (A3), (A4), (A14), and (A15) can be further simplified using a series expansion with respect to origin of the local coordinate system  $(\xi, \eta, \zeta)$ . For large values of  $|P|$  compared to  $|Q|$ , we obtain

$$I_{\sigma}(M,N) = (-1/4\pi) \{ E1/P + (E2 P)/P^2 + [-E3/2 + 3(P E4P)/2]/P^3 \} \quad (A16)$$

where

$$E1 = C(M,N) \quad (A17)$$

$$\vec{E2} = [ C(M+1,N) , C(M,N+1) , aC(M+2,N)+bC(M,N+2) ] \quad (A18)$$

$$E3 = C(M+2,N) + C(M,N+2) \quad (A19)$$

$$E4 = \begin{bmatrix} C(M+2,N) & C(M+1,N+1) & aC(M+3,N)+bC(M+1,N+2) \\ C(M+1,N+1) & C(M,N+2) & aC(M+2,N+1)+bC(M,N+3) \\ aC(M+3,N)+bC(M+1,N+2) & aC(M+2,N+1)+bC(M,N+3) & 0 \end{bmatrix} \quad (A20)$$

$$C(M,N) = H(M,N,0) \text{ evaluated at } x = y = z = 0. \quad (A21)$$

The leading terms in Eqs. in (A3), (A4), and (A11) correspond to a flat panel. The remaining terms having



coefficients of a, b, and c constitute panel curvature effects. The corresponding integrals associated with doublet distribution can be expressed in terms of H integrals with different combination of values M, N, and K. Furthermore, we can show that there exists a recurrence relationships between  $H(M,N,K)$  such that the computation of velocity potential and its derivatives involves only simple algebraic manipulations. The detailed evaluation of the H integral is illustrated by Johnson<sup>5</sup> and the results are summarized in Appendix B.

The total induced velocity potential at  $P(x_i, y_i, z_i)$  is, therefore, obtained by collecting individual contributions due to all the surface panels N,

$$\phi_i = \sum_{j=1}^N \phi_j \quad (A22)$$

Using the the relation for the source distribution, Eq. (20), the total induced velocity potential and induced velocities are expressed in terms of N singularity parameters

$$\phi_i = \sum_{j=1}^N (C\phi)_{ij} \sigma_j \quad (A23)$$

$$\vec{V}_i = \sum_{j=1}^N [CV_x, CV_y, CV_z]_{ij} \sigma_j \quad (A24)$$

where  $(C\phi)_{ij}$  and  $[CV_x, CV_y, CV_z]_{ij}$  denote the influence kernels associated with the j-th singularity parameter evaluated at the i-th control point.

## APPENDIX B

### COMPUTATION OF H INTEGRALS

In this appendix we shall summarize the recursion relations which were used for the computation of H integrals in Eqs. (A1)-(A15). The detailed derivation of these recursion relations can be found in Johnson.<sup>5</sup>

From the definition of H integrals

$$H(M,N,K) = \iiint \frac{(\xi-x)^{M-1}(\eta-y)^{N-1}}{\rho^K} d\xi d\eta. \quad (B1)$$

$$\rho = \sqrt{(\xi-x)^2 + (\eta-y)^2 + (\zeta-z)^2},$$

where

$$M = 0,1,2,\dots; \quad N = 0,1,2,\dots; \quad K = 1,3,5,\dots$$

we can easily show the following identity:

$$H(M+2,N,K) + H(M,N+2,K) + h^2 H(M,N,K) = H(M,N,K-2). \quad (B2)$$

Integrating by parts yields second recursion relations

$$(K-2)H(M,N,K) = (M-1)H(M-2,N,K-2) + \sum_{\xi} v_{\xi} F(M-1,N,K-2) \quad (B3)$$

and

$$(K-2)H(M,N,K) = (N-1)H(M,N-2,K-2) + \sum_{\eta} v_{\eta} F(M,N-1,K-2). \quad (B4)$$

The summation on the right side of Eqs. (B3) and (B4) is over all four sides of  $\Sigma$  shown in Fig. 2. Here  $v = v(\xi, \eta)$  is the unit outer normal to the side of  $\Sigma$  and  $F(M,N,K)$  is the line integral defined by

$$F(M,N,K) = \int_L \frac{(\xi-x)^{M-1}(\eta-y)^{N-1}}{\rho^K} dl. \quad (B5)$$

Similarly we can devise the recursion relations for the computation of F integrals. From the definition of F integrals we have the identities

$$F(M+2,N,K) + F(M,N+2,K) + h^2 F(M,N,K) = F(M,N,K-2) \quad (B6)$$

and

$$v_{\xi} F(M+1,N,K) + v_{\eta} F(M,N+1,K) = -a F(M,N,K). \quad (B7)$$

Integration by parts also yields

$$\begin{aligned} & (K-2)v_{\xi} F(M,N+1,K) - (K-2)v_{\eta} F(M+1,N,K) \\ & = Nv_{\xi} F(M,N-1,K-2) - Mv_{\eta} F(M-1,N,K-2) + E(M,N,K-2) \end{aligned} \quad (B8)$$

where

$$E(M,N,K) = [ (\xi-x)^{M-1} (\eta-y)^{N-1} / \rho^K ]. \quad (B9)$$

The recursion relations for H and F have been recombined in the present procedure to compute needed H and F integrals efficiently and accurately. For example, since S is a singular surface for H, the reverse of the relation Eq. (B3) has been used for the field point in the interior of S. Similar care has been exercised for the evaluation of F integrals. By properly accounting for the singular behavior of H, it was possible to compute accurate velocities even when the field point is close to the edge or corner of S.

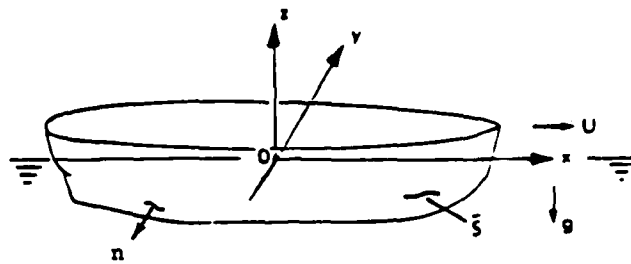


Fig. 1. Coordinate system.

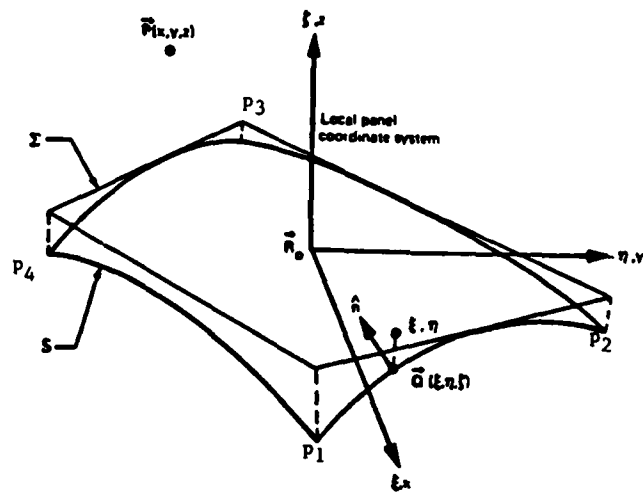


Fig. 2. Field point/panel geometry.

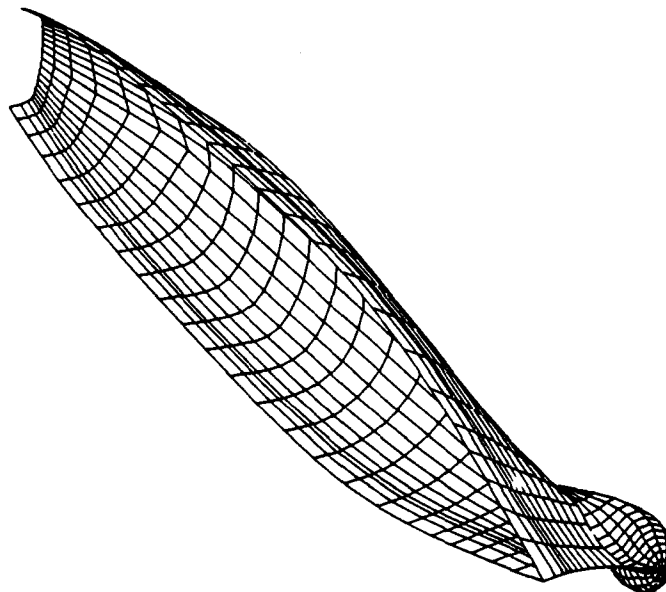


Fig. 3. 3-D perspective view of the surface panel network.

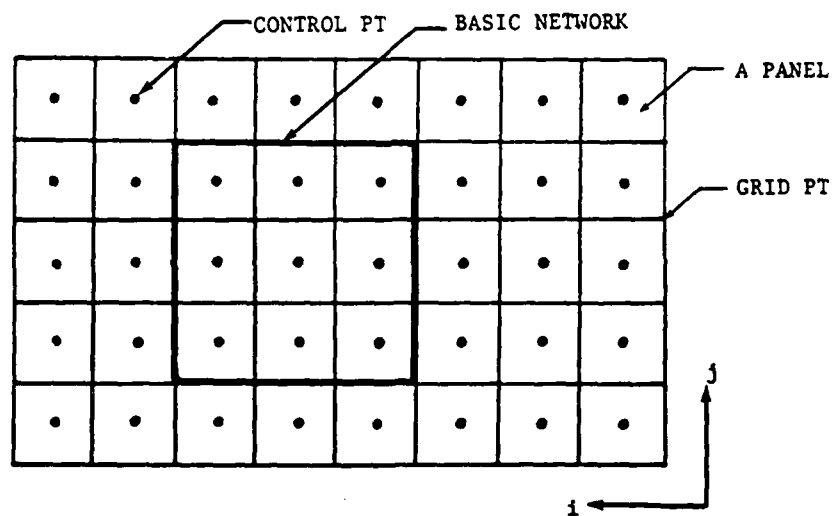


Fig. 4. Network of panels.

#### Hull Geometry

$$B/L = 0.1000$$

$$H/L = 0.0625$$

$$C_B = 0.444$$

$$C_{PR} = 0.667$$

$$C_x = 0.667$$

$$C_i = 0.661$$

$$L/L_{pp} = 1.000 \text{ (where } L = LWL \text{)}$$

The hull surface is shown in Figure 5 and is defined by:

$$y = \frac{B}{2} \left\{ 1 - \left( \frac{2x}{L} \right)^2 \right\} \left\{ 1 - \left( \frac{z}{H} \right)^2 \right\}$$

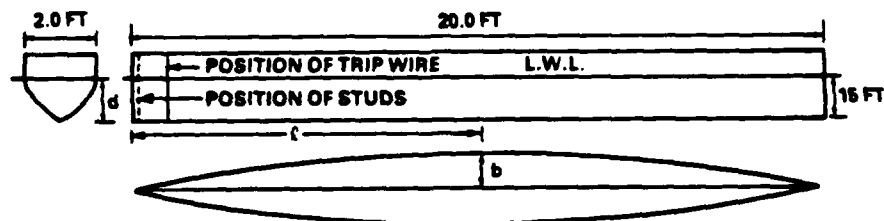


Fig. 5. Wigley hull form (from Shearer and Cross, 1965).

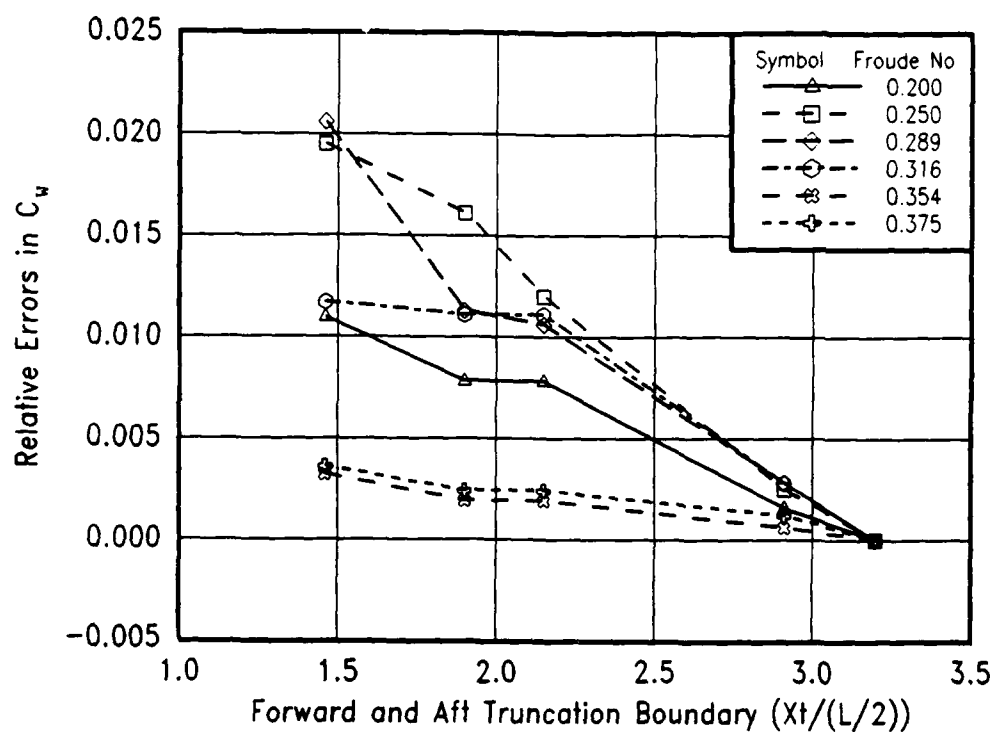


Fig. 6. Convergence test for X-direction truncation boundary.

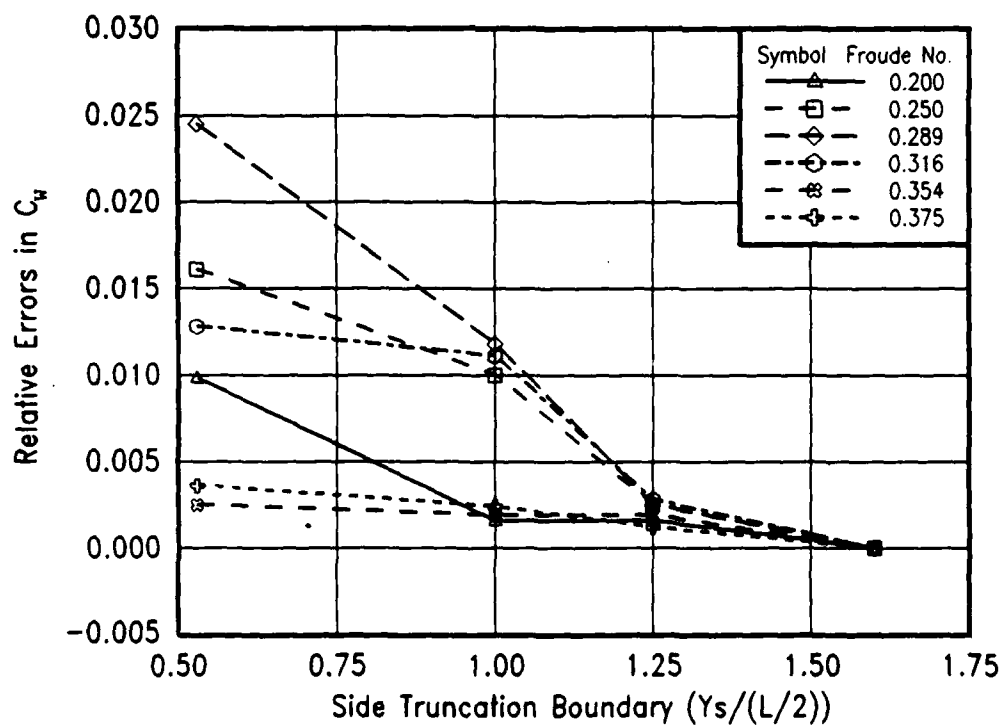


Fig. 7. Convergence test for Y-direction truncation boundary.

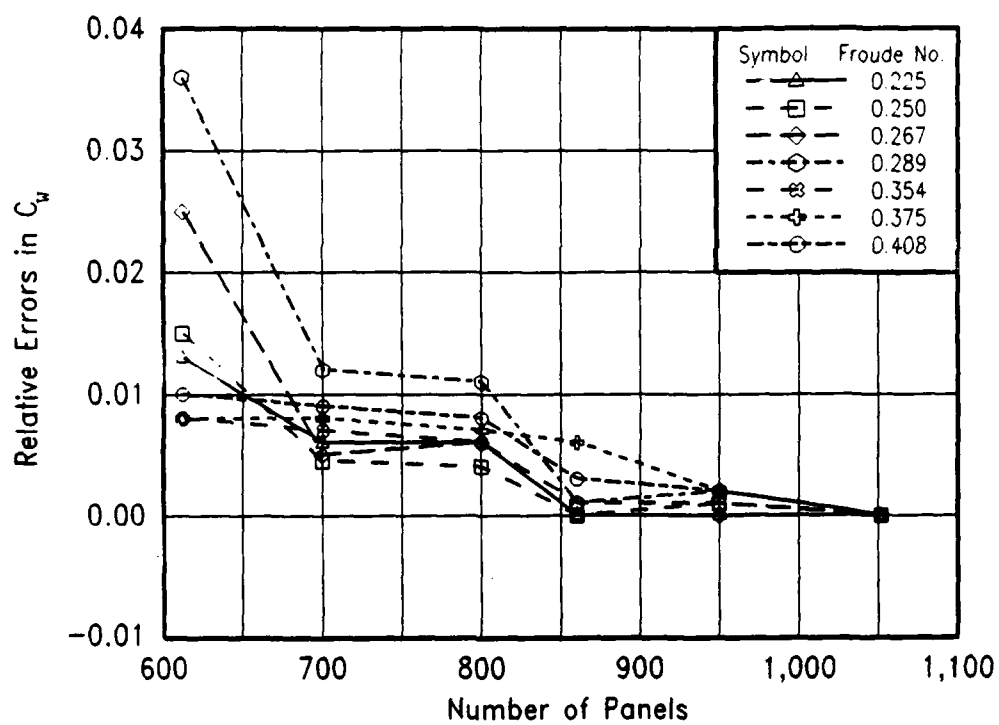


Fig. 8. Convergence test for number of panels.

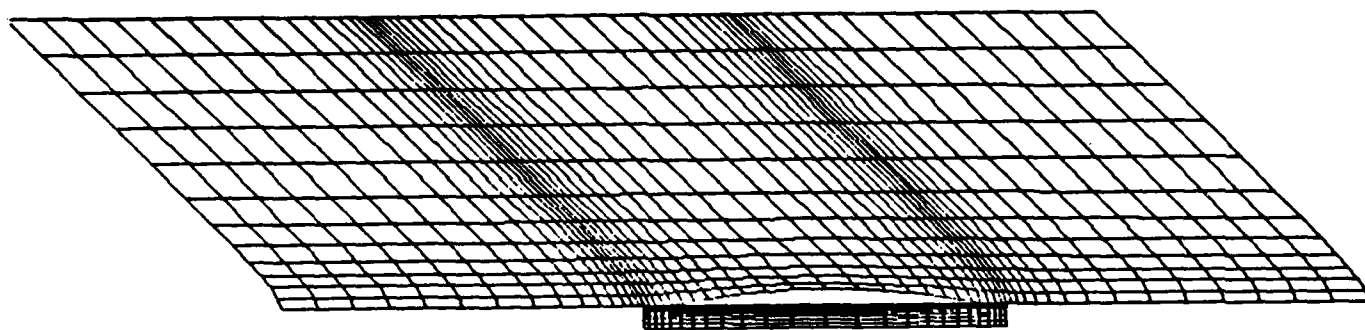
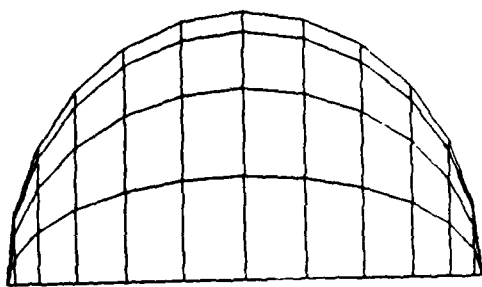
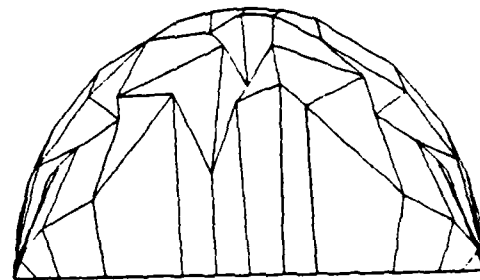


Fig. 9. Illustration of body and free surface panel network.



Regular Paneling



Random Paneling

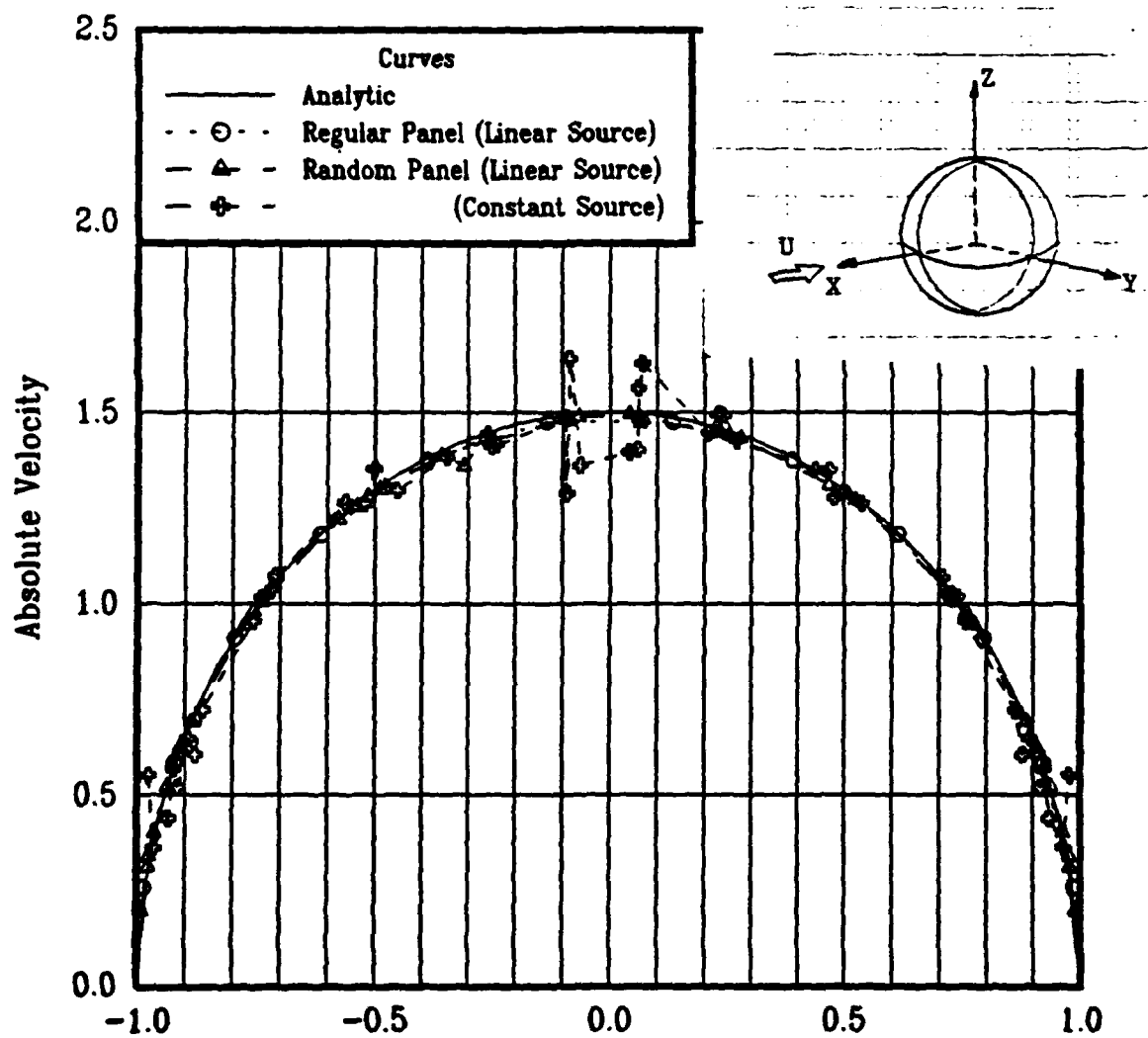


Fig. 10. Regular and random paneling of sphere.



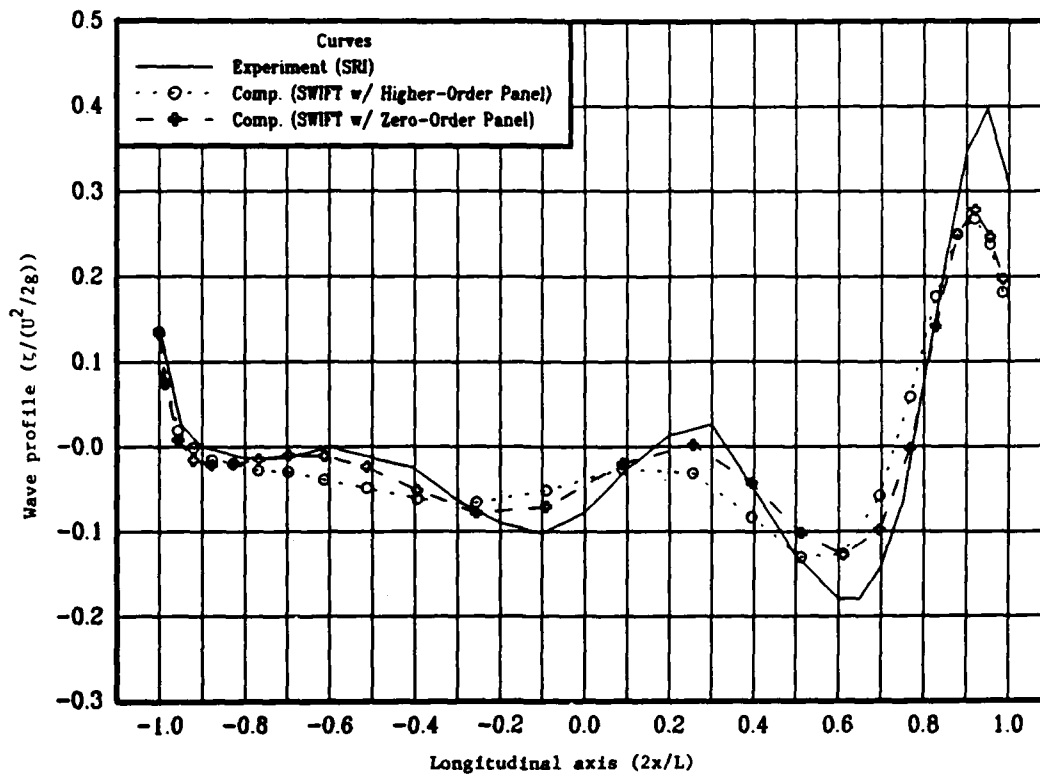


Fig. 11. Wave profile comparison for Wigley hull at  $F_n=0.250$ .

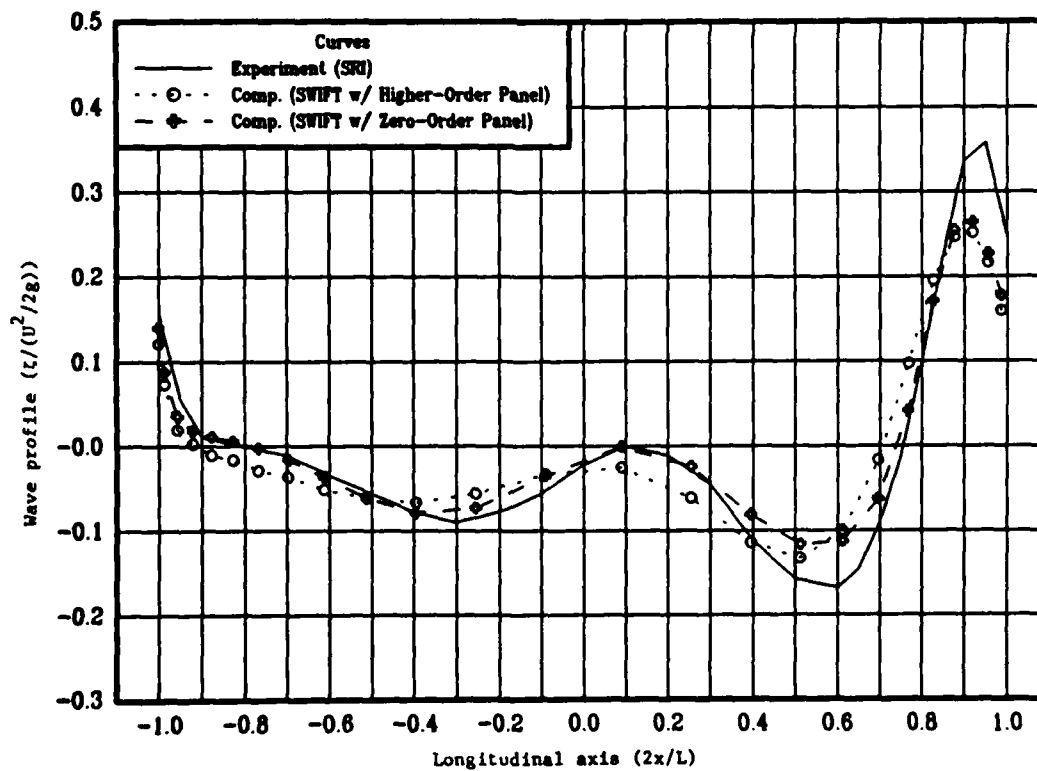


Fig. 12. Wave profile comparison for Wigley hull at  $F_n=0.267$ .

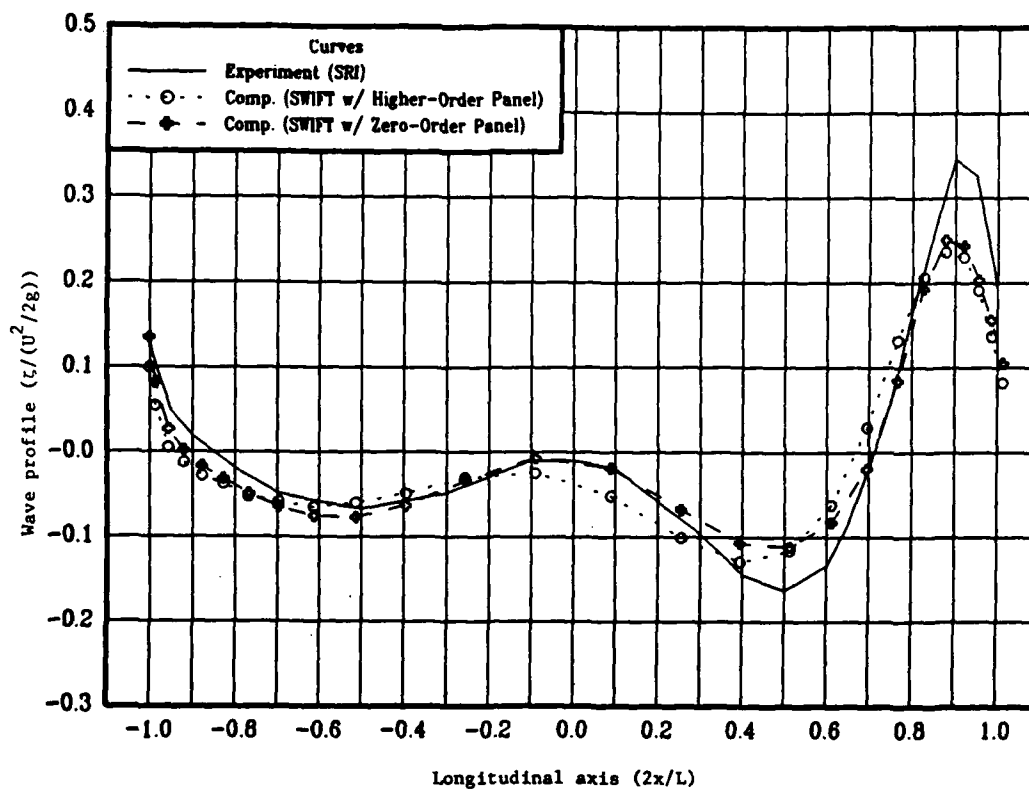


Fig. 13. Wave profile comparison for Wigley hull at  $F_n=0.289$ .

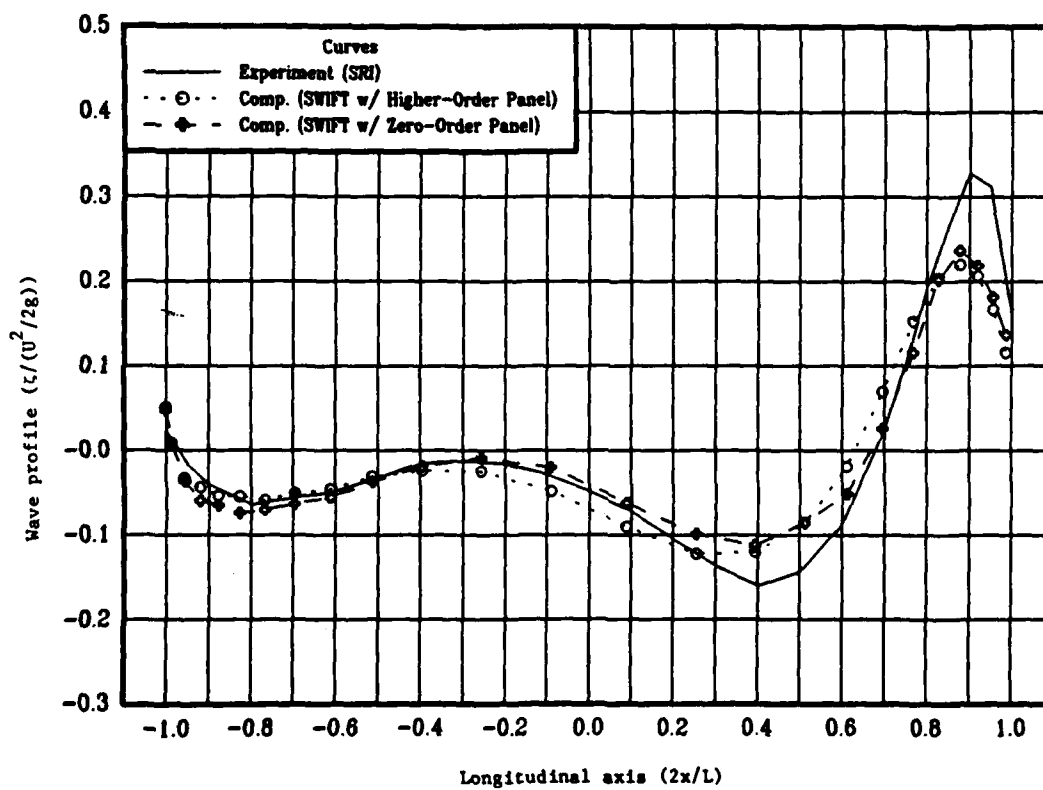


Fig. 14. Wave profile comparison for Wigley hull at  $F_n=0.316$ .

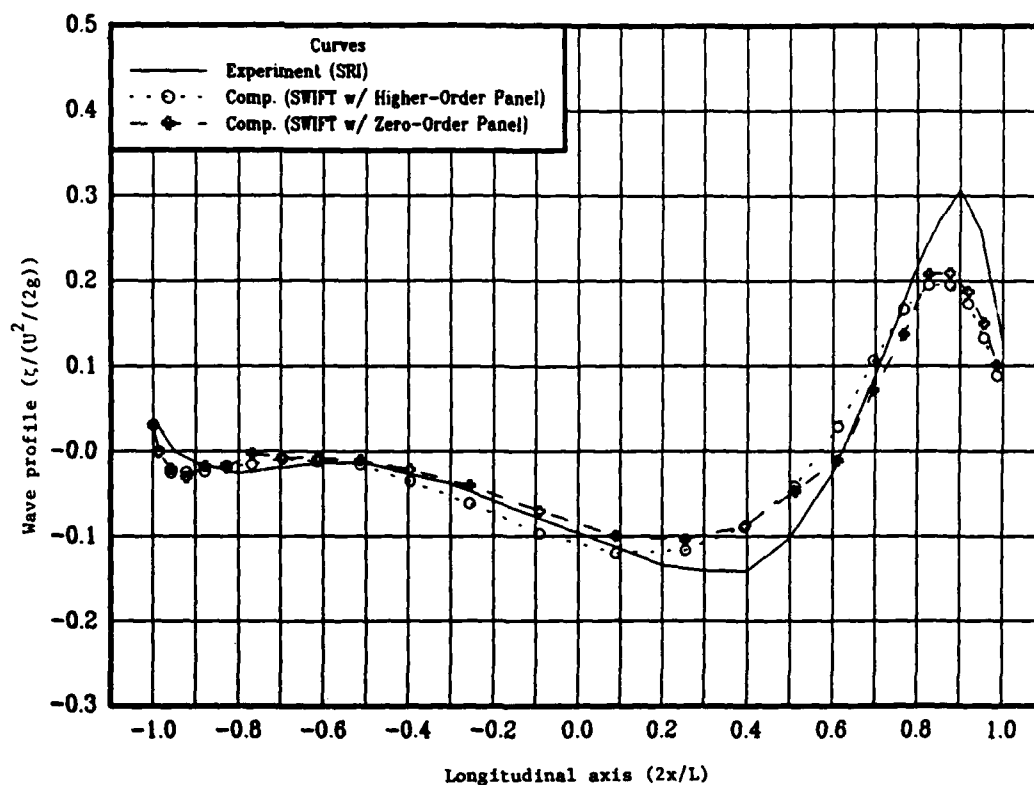


Fig. 15. Wave profile comparison for Wigley hull at  $F_n=0.354$ .

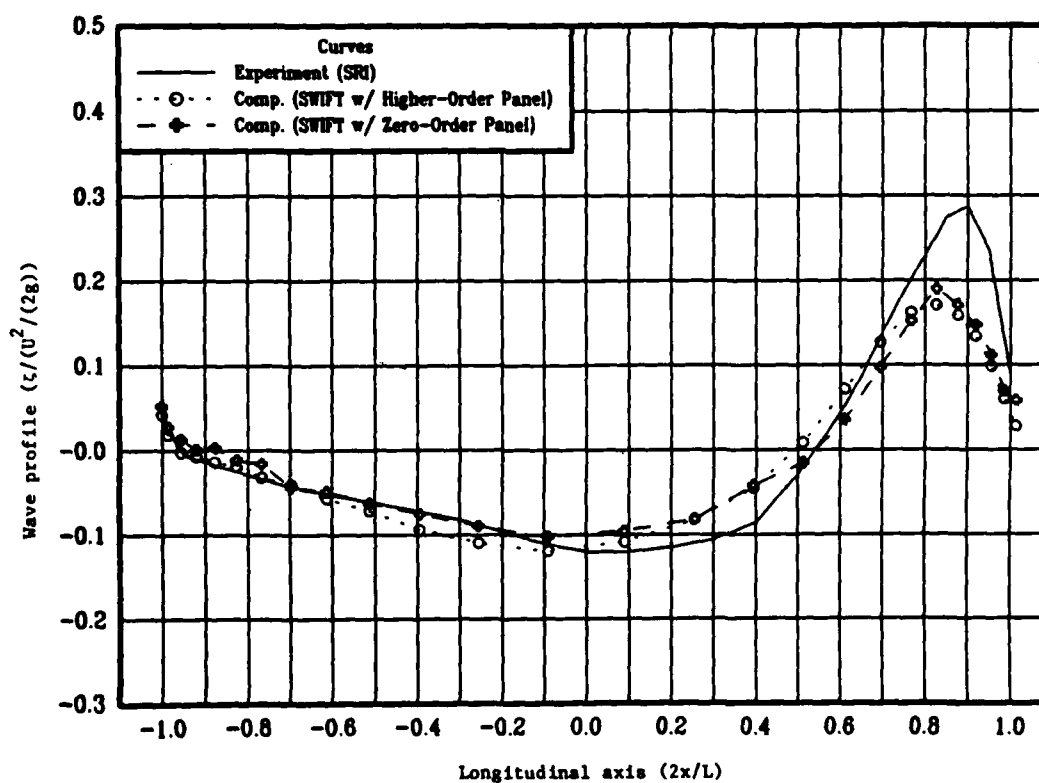


Fig. 16. Wave profile comparison for Wigley hull at  $F_n=0.408$ .

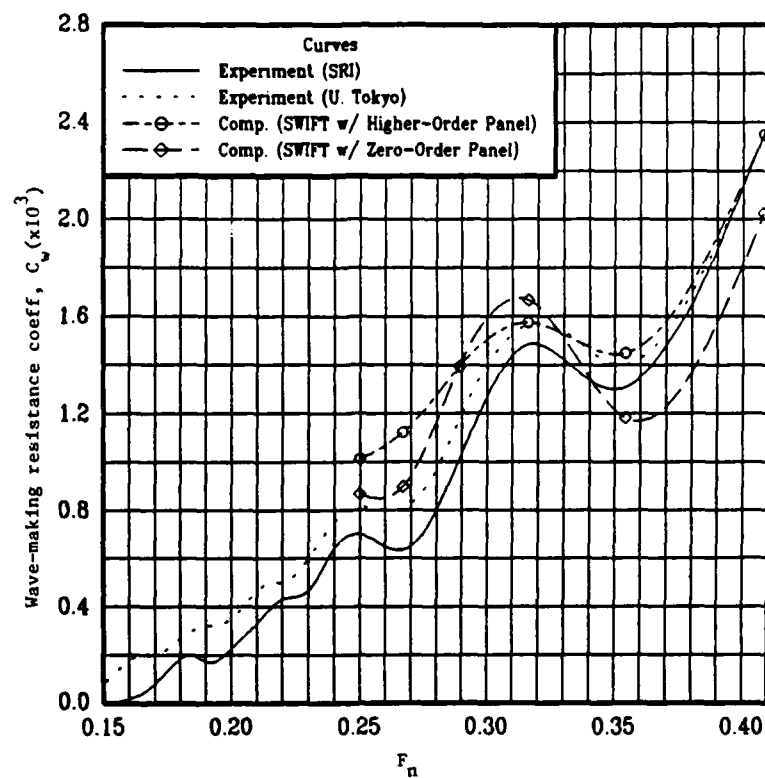


Fig. 17. Wave-making resistance comparison for Wigley hull.

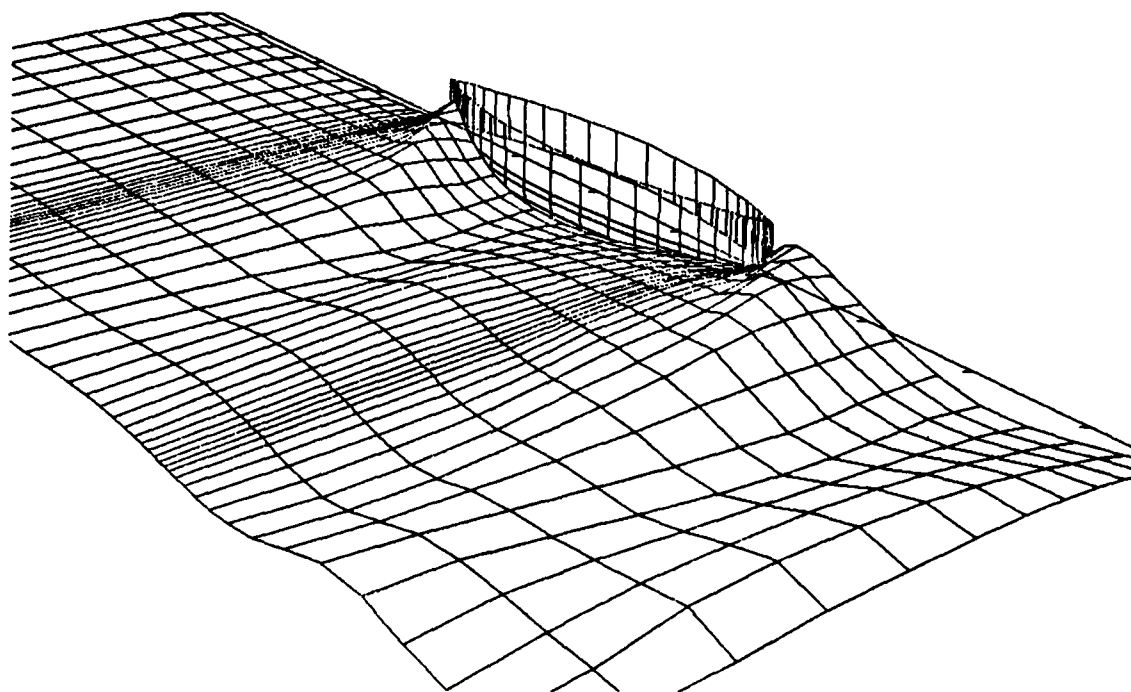


Fig. 18. 3-D perspective view of Wigley hull generated waves at  $F_n=0.408$ .

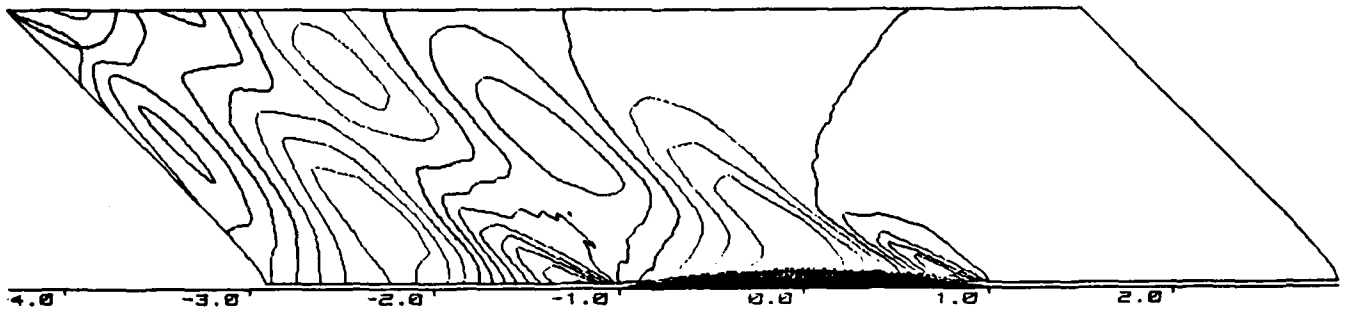


Fig. 19. Predicted wave contour plot for Wigley hull at  $F_n=0.408$ .

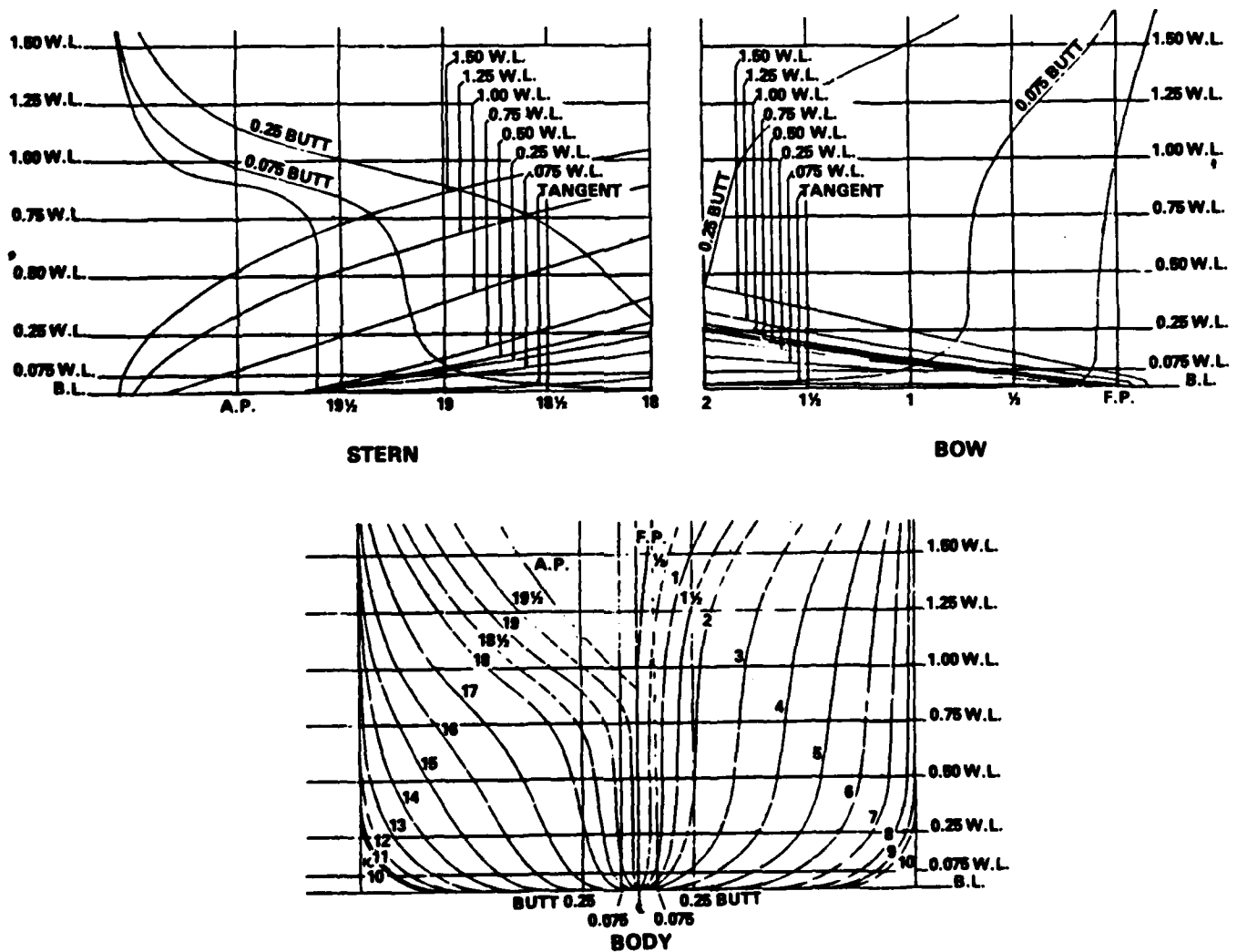


Fig. 20. Lines of Series 60,  $C_B=0.60$  (from Todd, 1953).

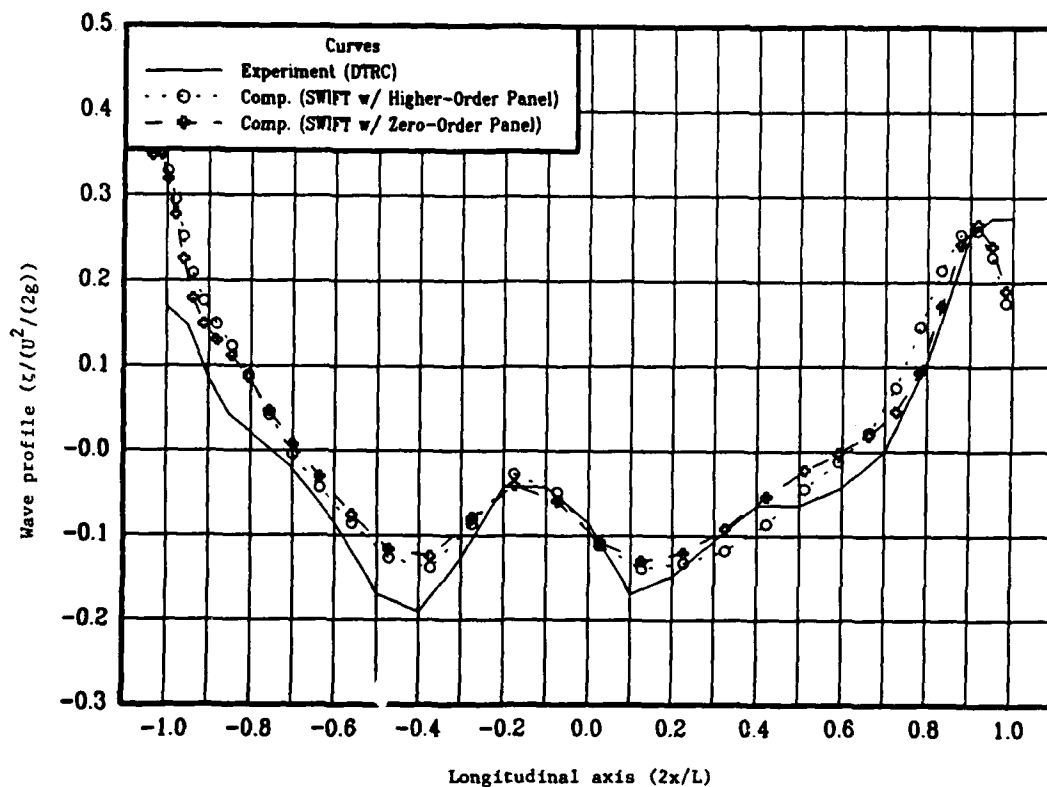


Fig. 21. Wave profile comparison for Series 60 at  $F_n=0.220$ .

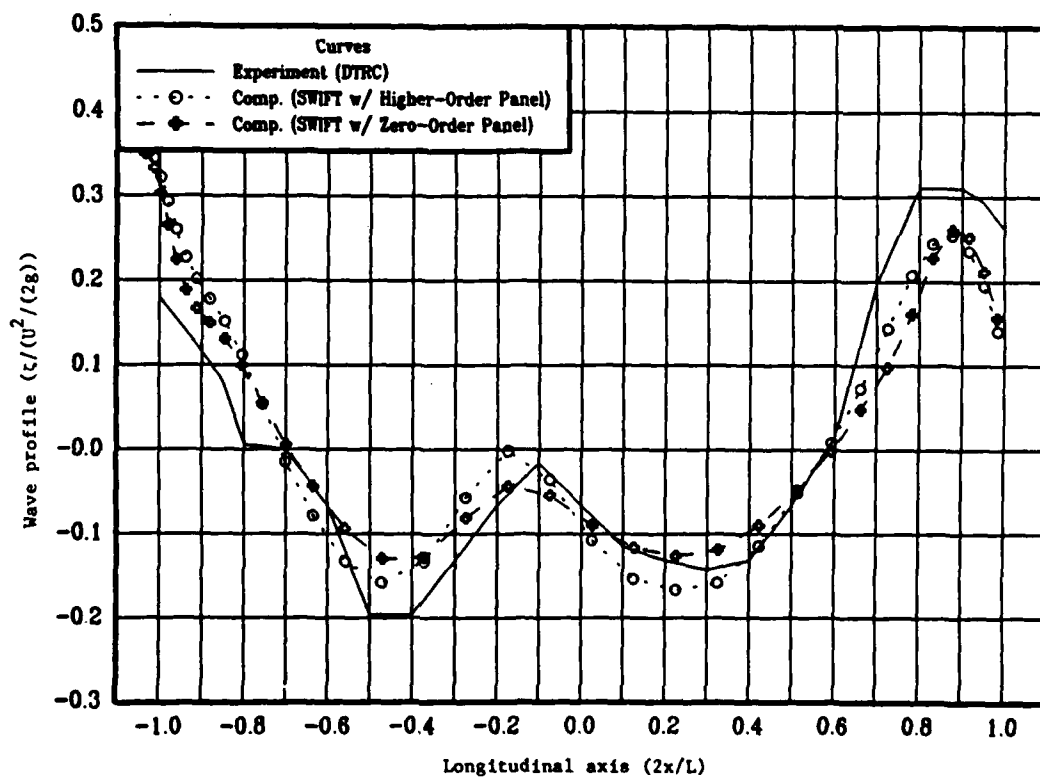


Fig. 22. Wave profile comparison for Series 60 at  $F_n=0.250$ .

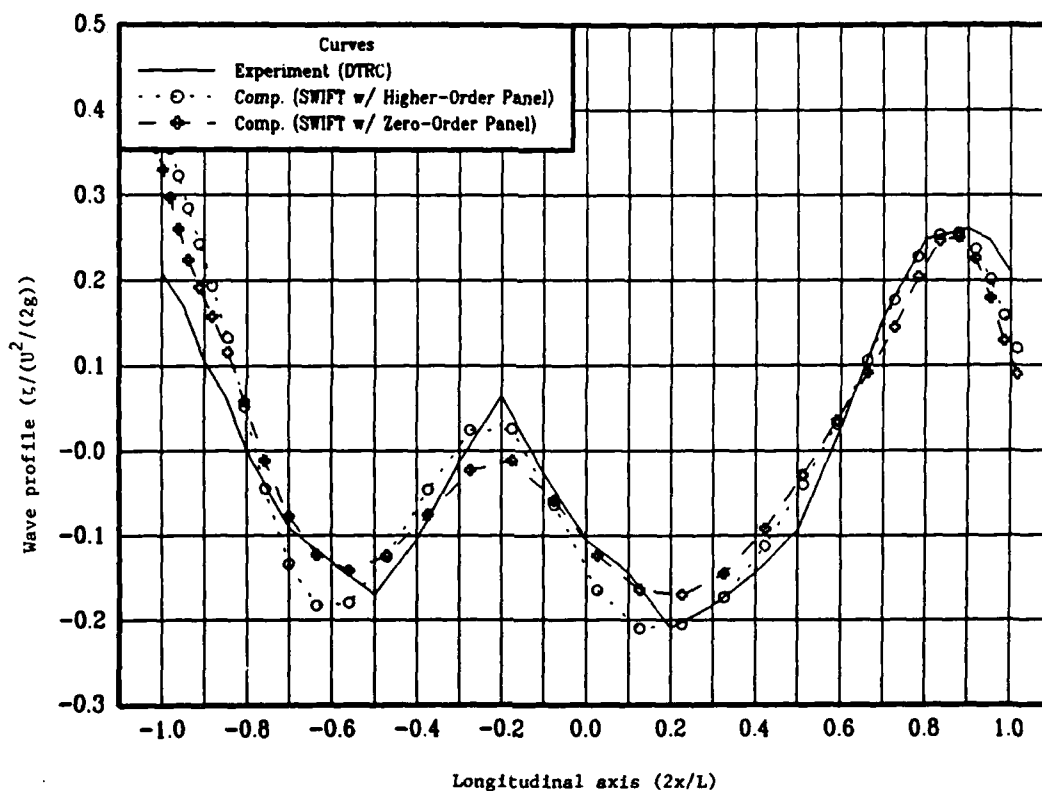


Fig. 23. Wave profile comparison for Series 60 at  $F_n=0.280$ .

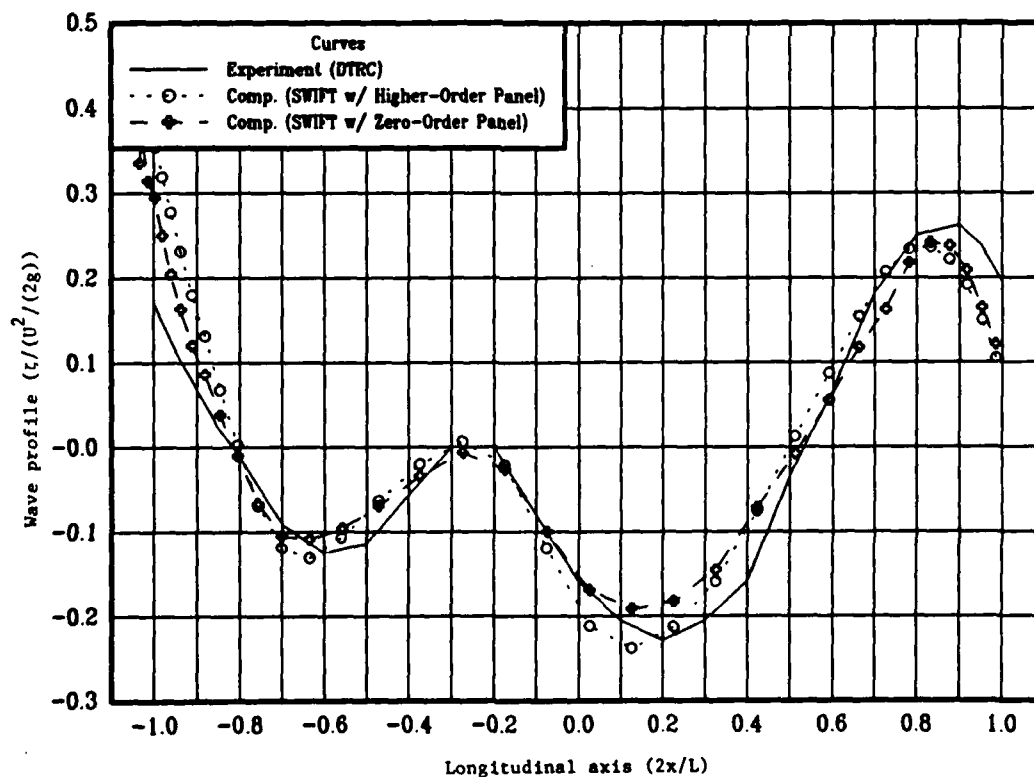


Fig. 24. Wave profile comparison for Series 60 at  $F_n=0.300$ .

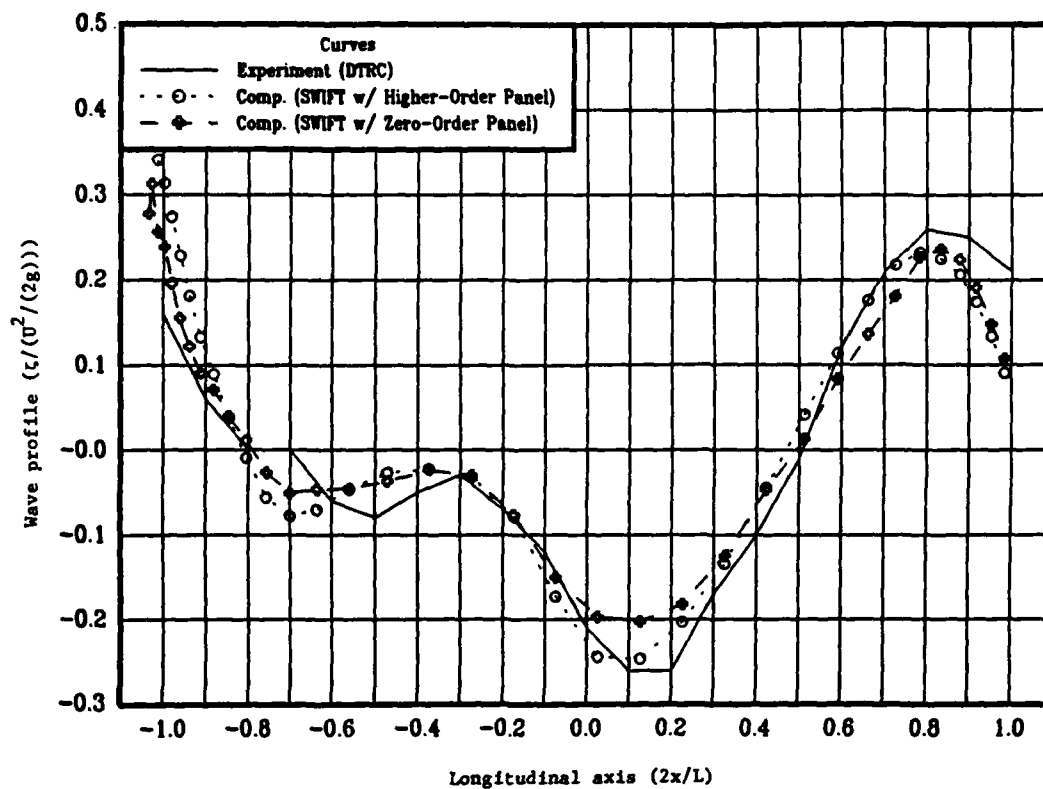


Fig. 25. Wave profile comparison for Series 60 at  $F_n=0.320$ .

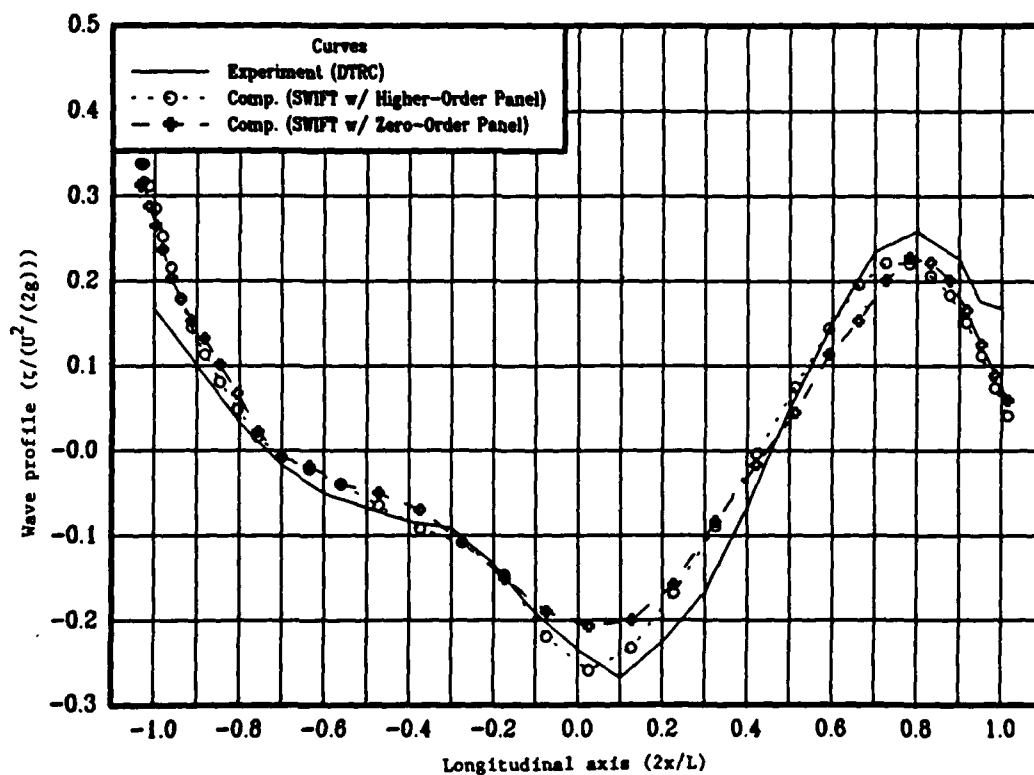


Fig. 26. Wave profile comparison for Series 60 at  $F_n=0.350$ .



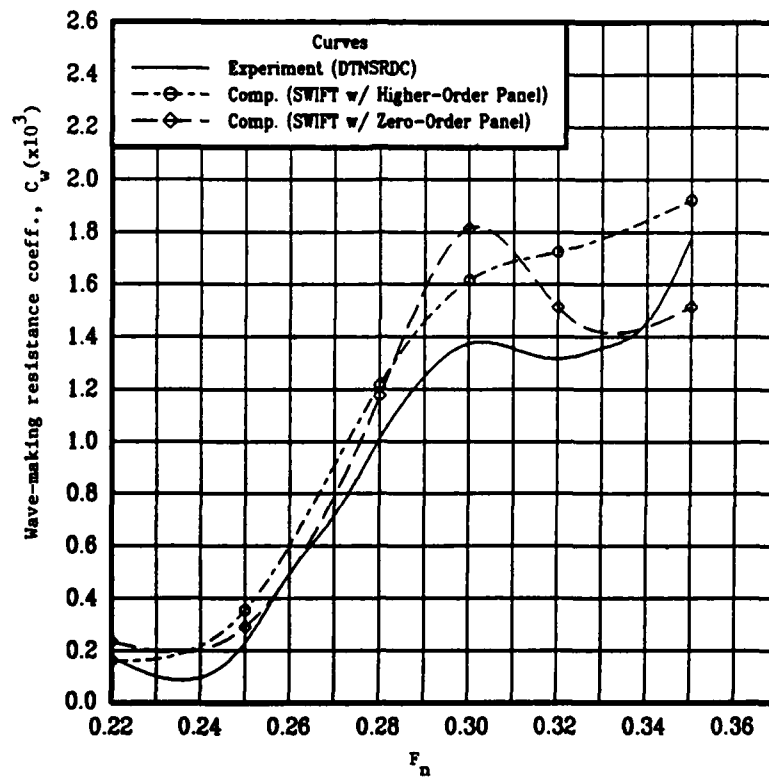


Fig. 27. Wave-making resistance comparison for Series 60.

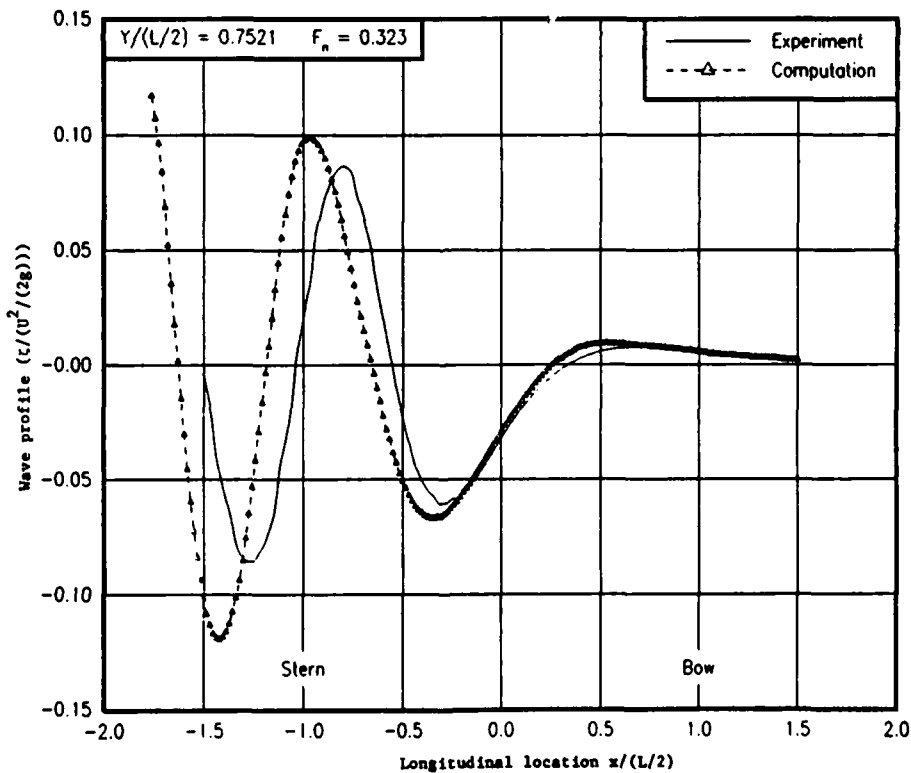


Fig. 28. Longitudinal wave-cut comparison for Series 60.

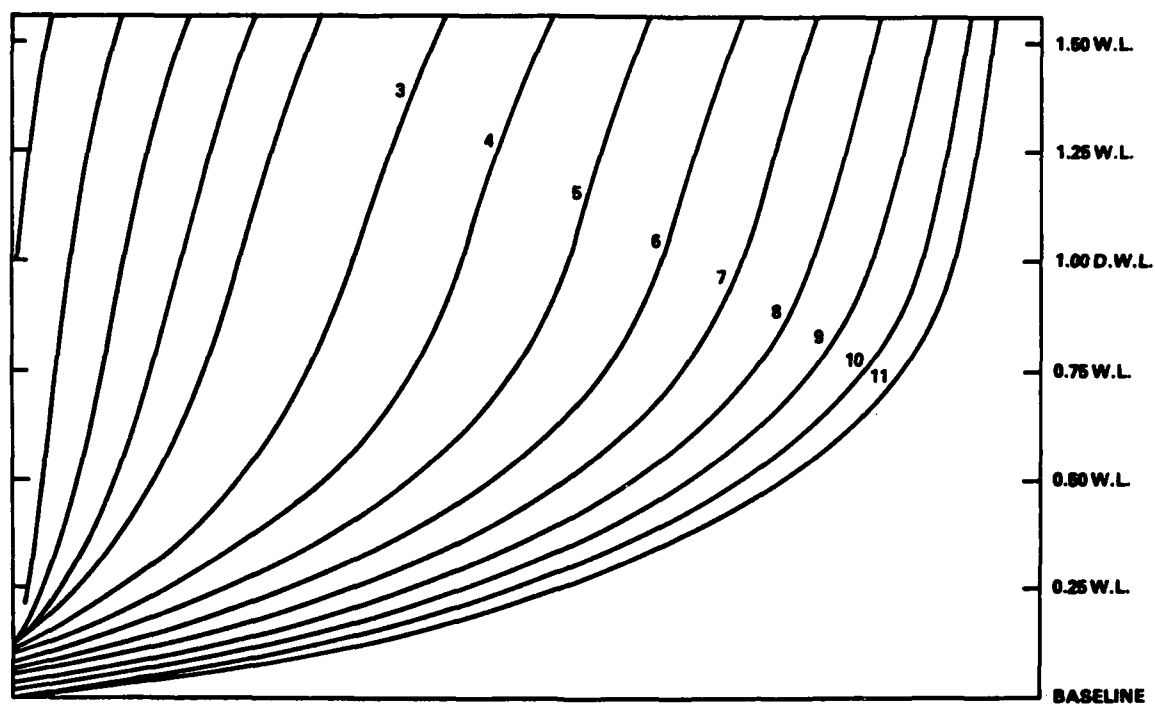


Fig. 29. Body plan of the fore body of Athena.

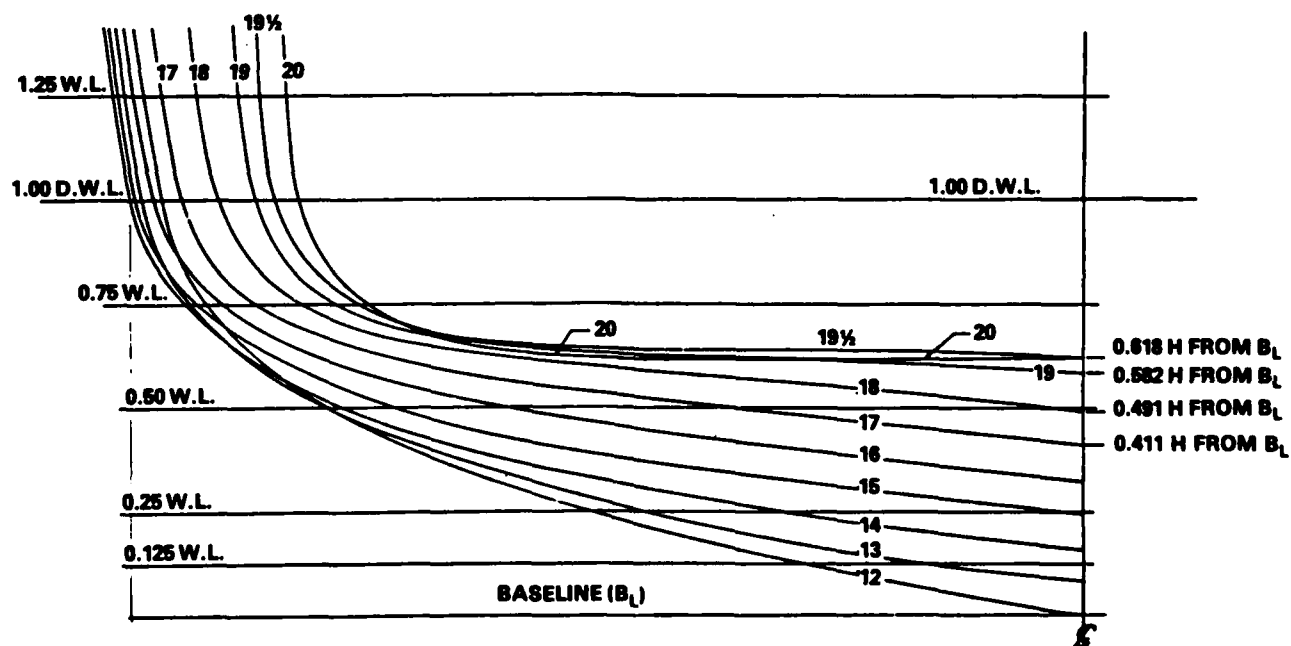


Fig. 30. Body plan of the aft body of Athena.

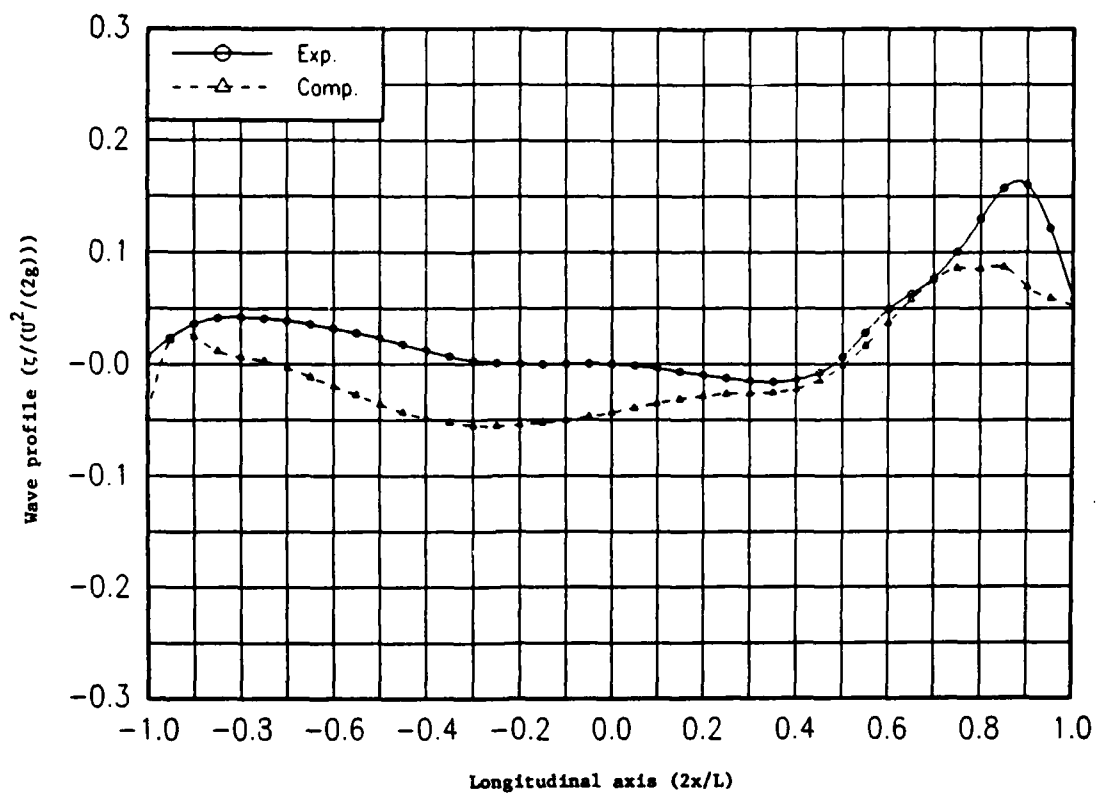


Fig. 31. Wave profile comparison for Athena hull at  $F_n=0.350$ .

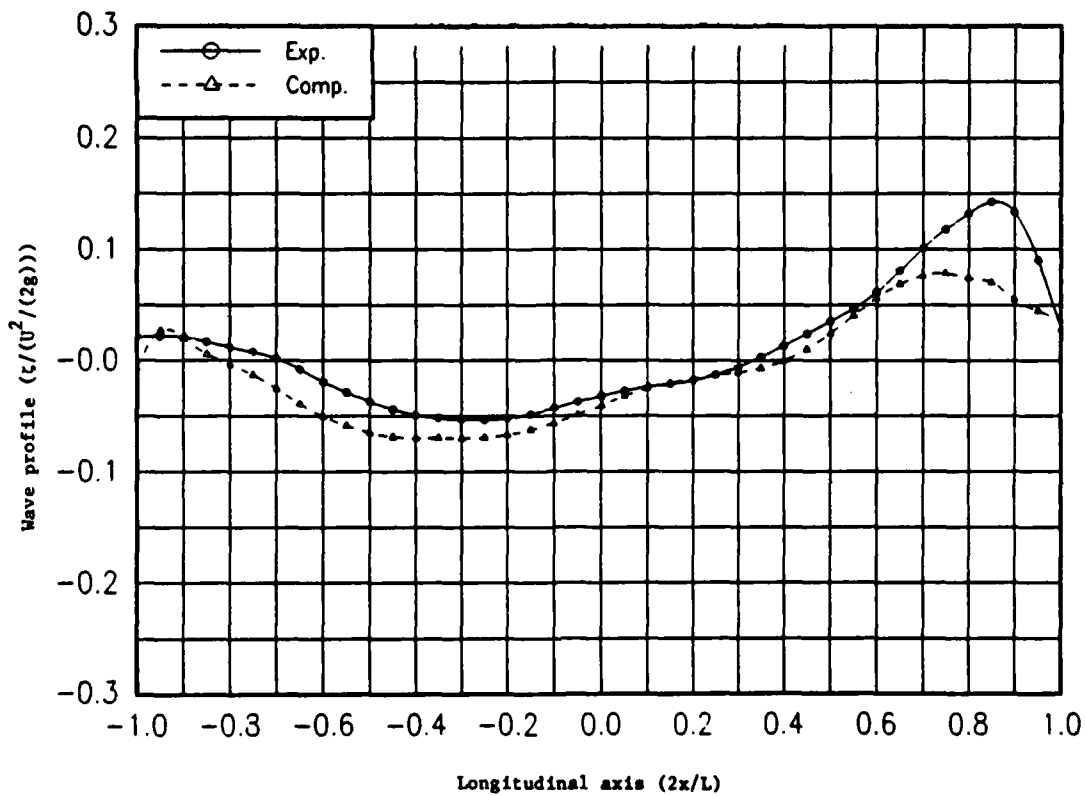
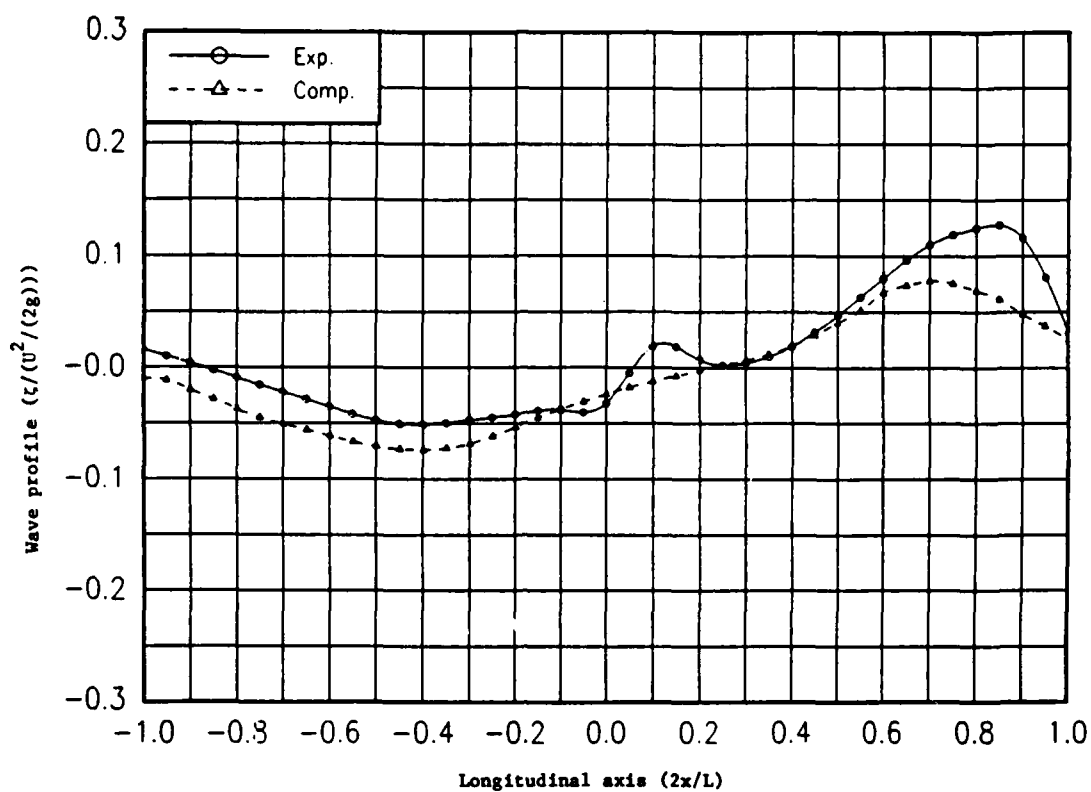
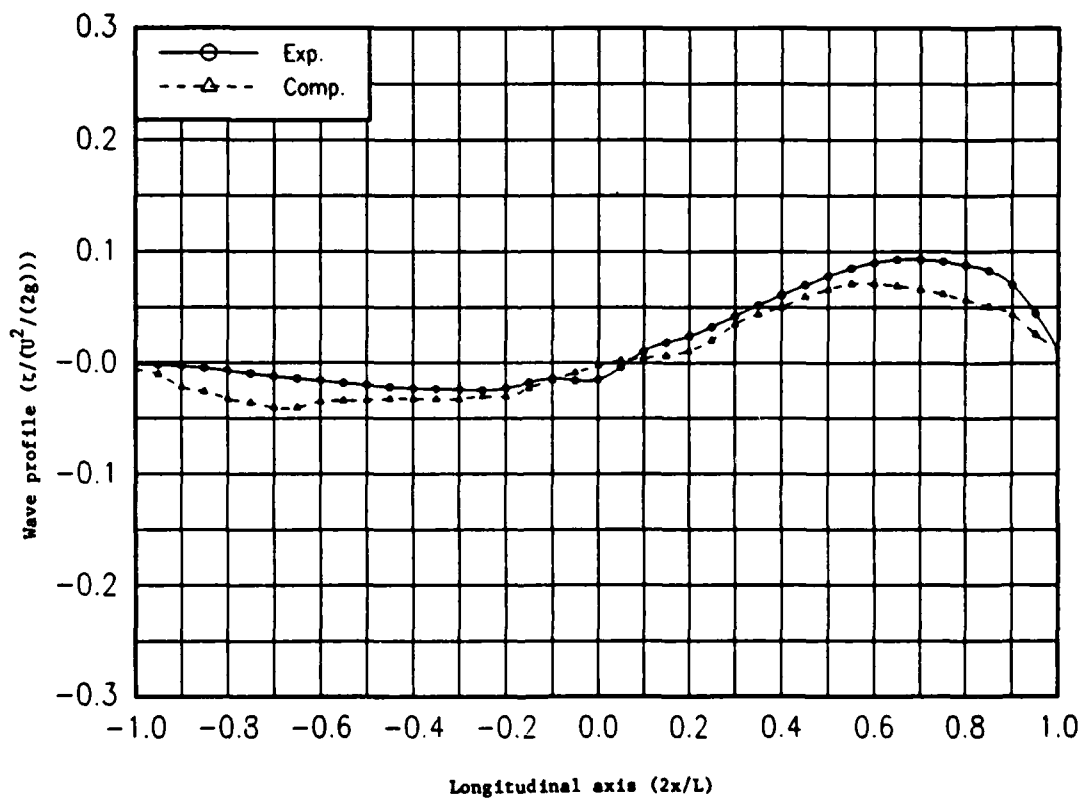


Fig. 32. Wave profile comparison for Athena hull at  $F_n=0.412$ .



**Fig. 33.** Wave profile comparison for Athena hull at  $F_n=0.484$ .



**Fig. 34.** Wave profile comparison for Athena hull at  $F_n=0.651$ .

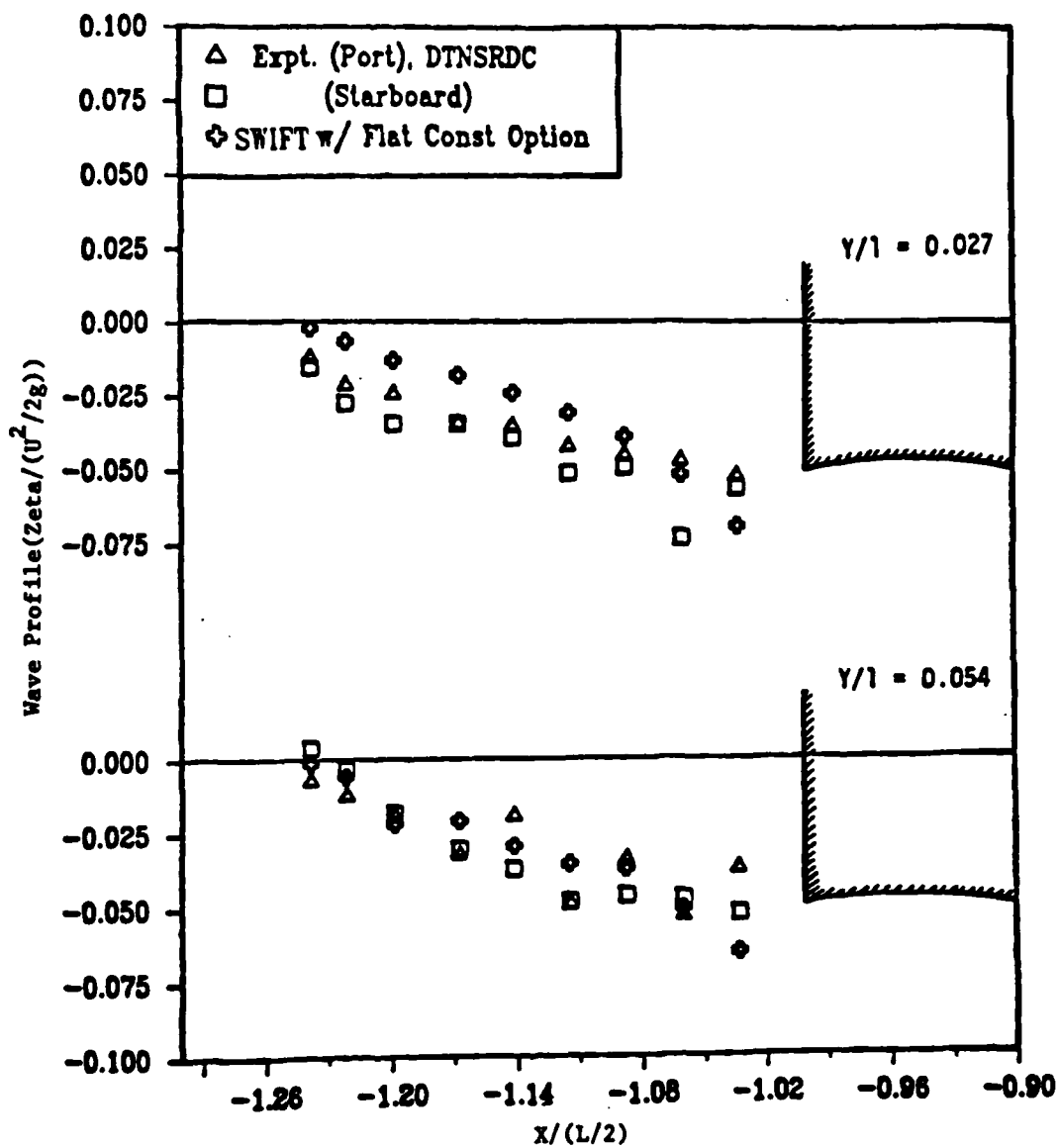


Fig. 35. Wave profile comparison behind stern at  $F_n=0.484$ .

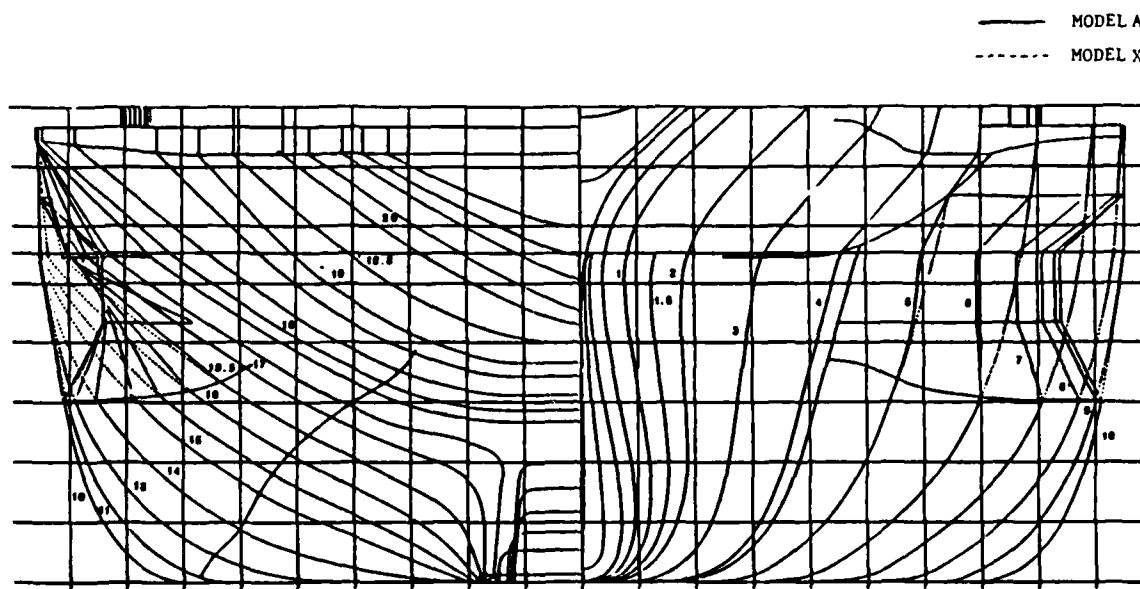


Fig. 36. Body plans of Models X and A.

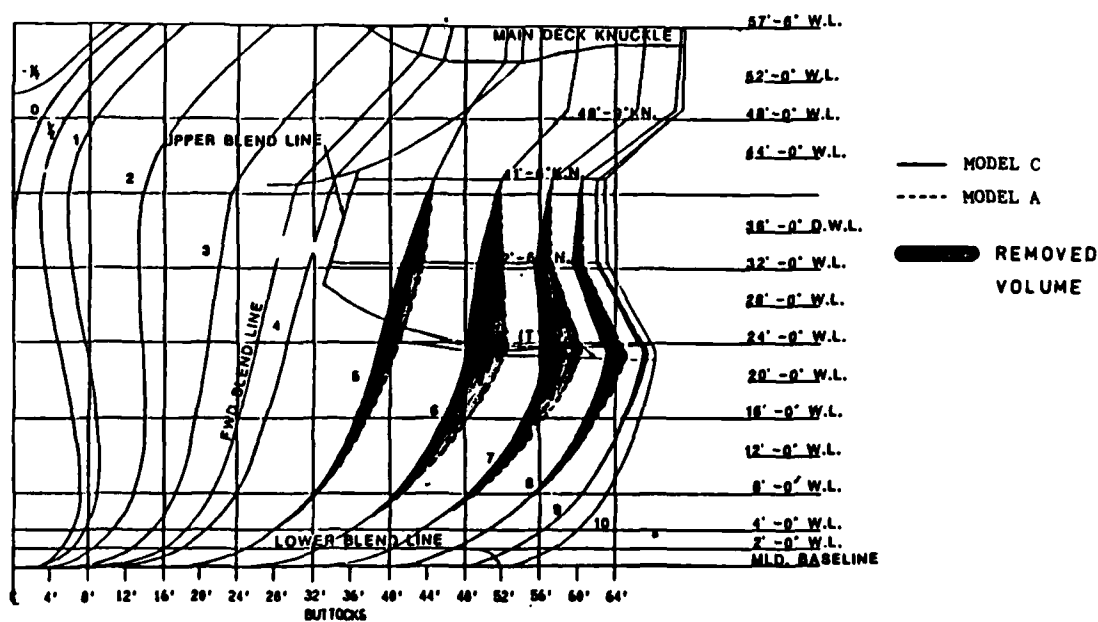


Fig. 37. Body plans of Models A and C.

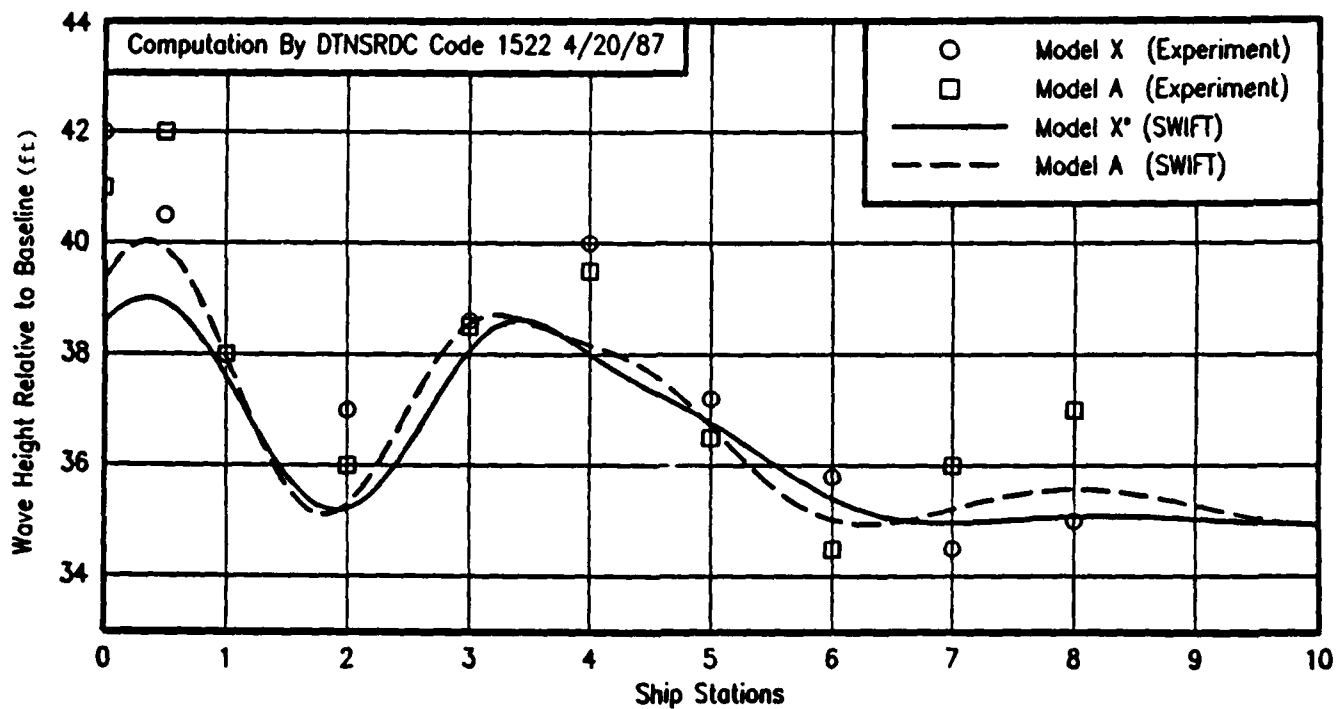


Fig. 38. Wave profile along the hull at  $F_n=0.179$ .

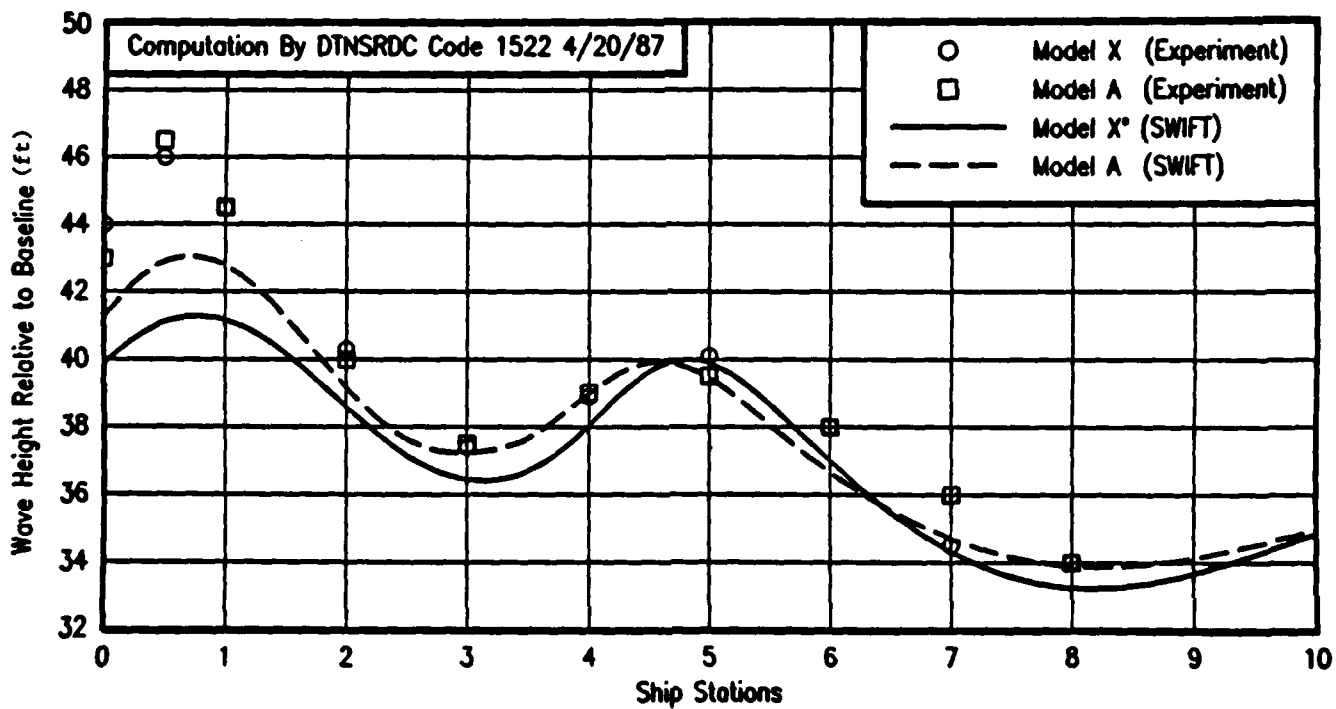


Fig. 39. Wave profile along the hull at  $F_n=0.238$ .

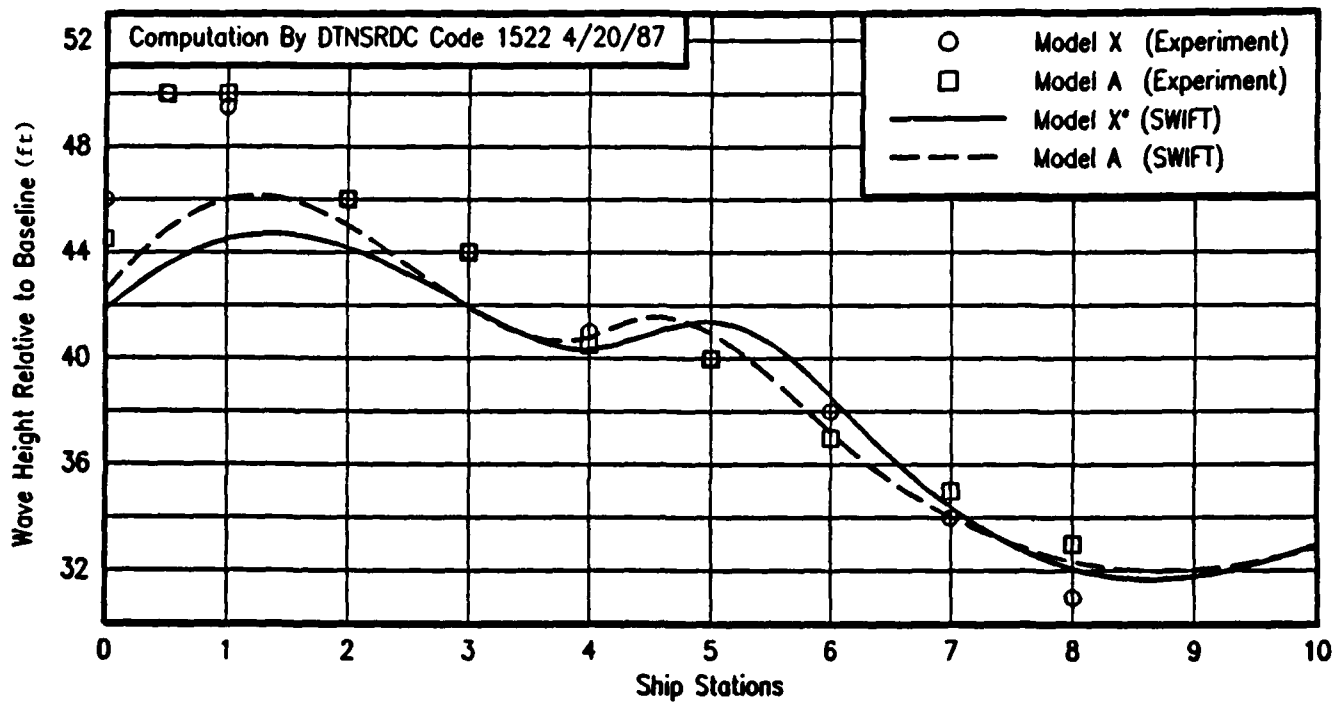


Fig. 40. Wave profile along the hull at  $F_n=0.298$ .

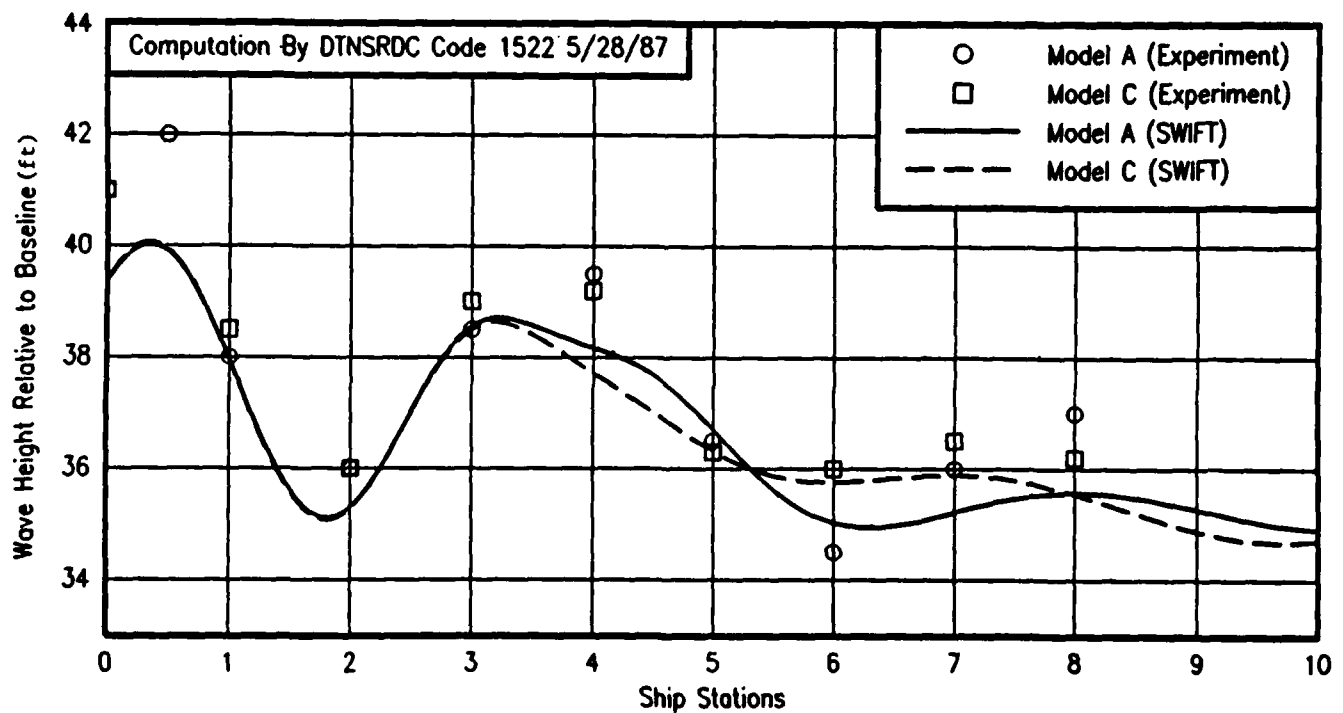


Fig. 41. Wave profile along the hull at  $F_n=0.179$  for Models A and C.



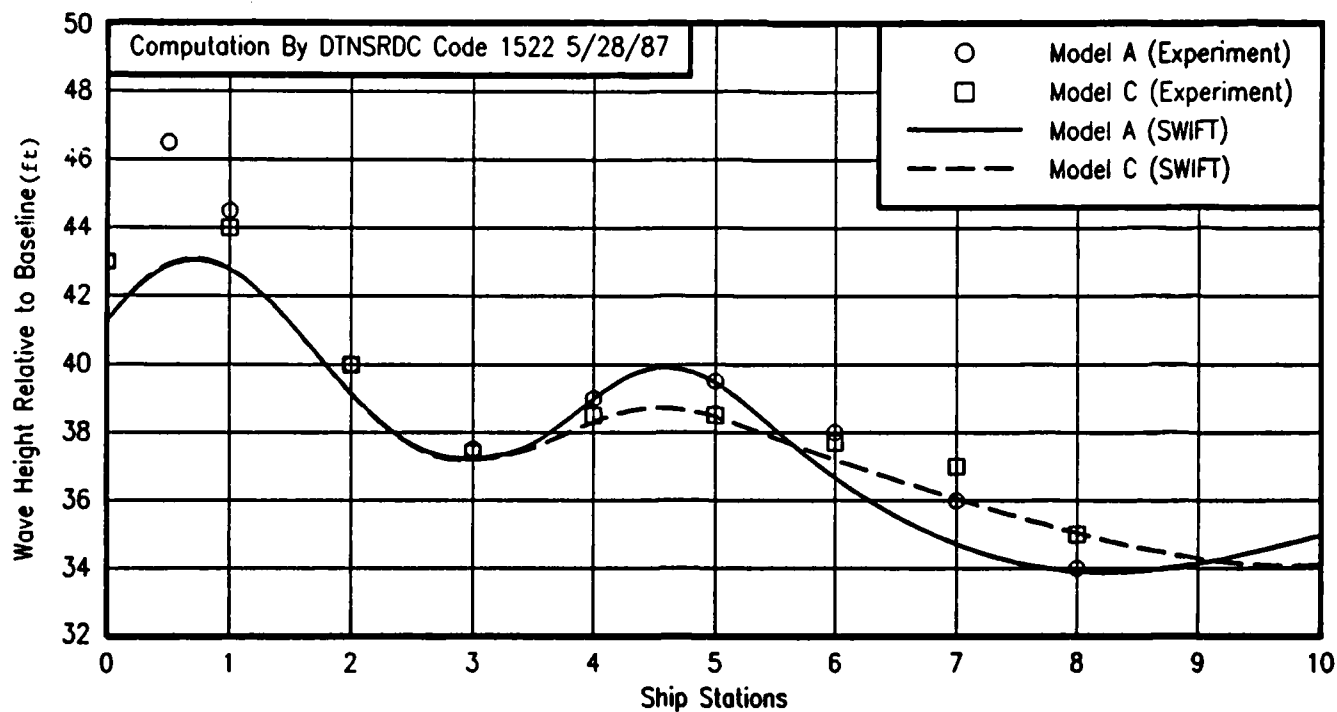


Fig. 42. Wave profile along the hull at  $F_n=0.238$  for Models A and C.

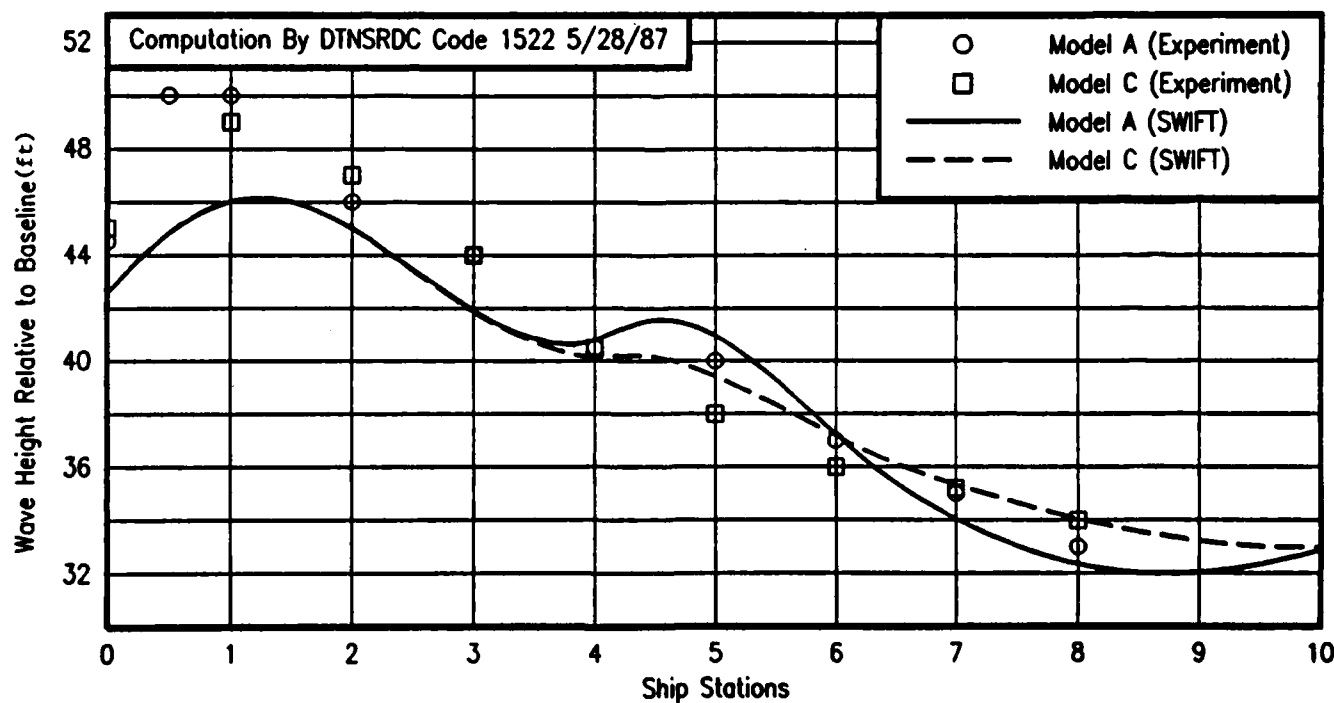
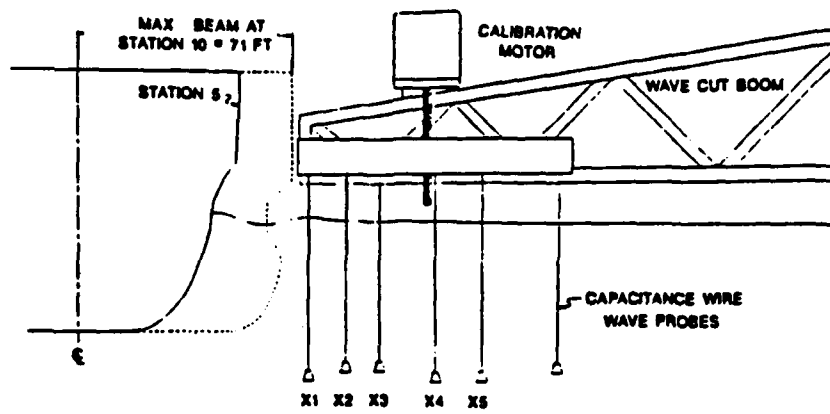


Fig. 43. Wave profile along the hull at  $F_n=0.298$  for Models A and C.



x1 = 77.5 ft off centerline  
 x2 = 89.9 ft off centerline  
 x3 = 102.1 ft off centerline  
 x4 = 119.2 ft off centerline  
 x5 = 135.8 ft off centerline

Fig. 44. Capacitance wire wave probes for wave-cut measurements.

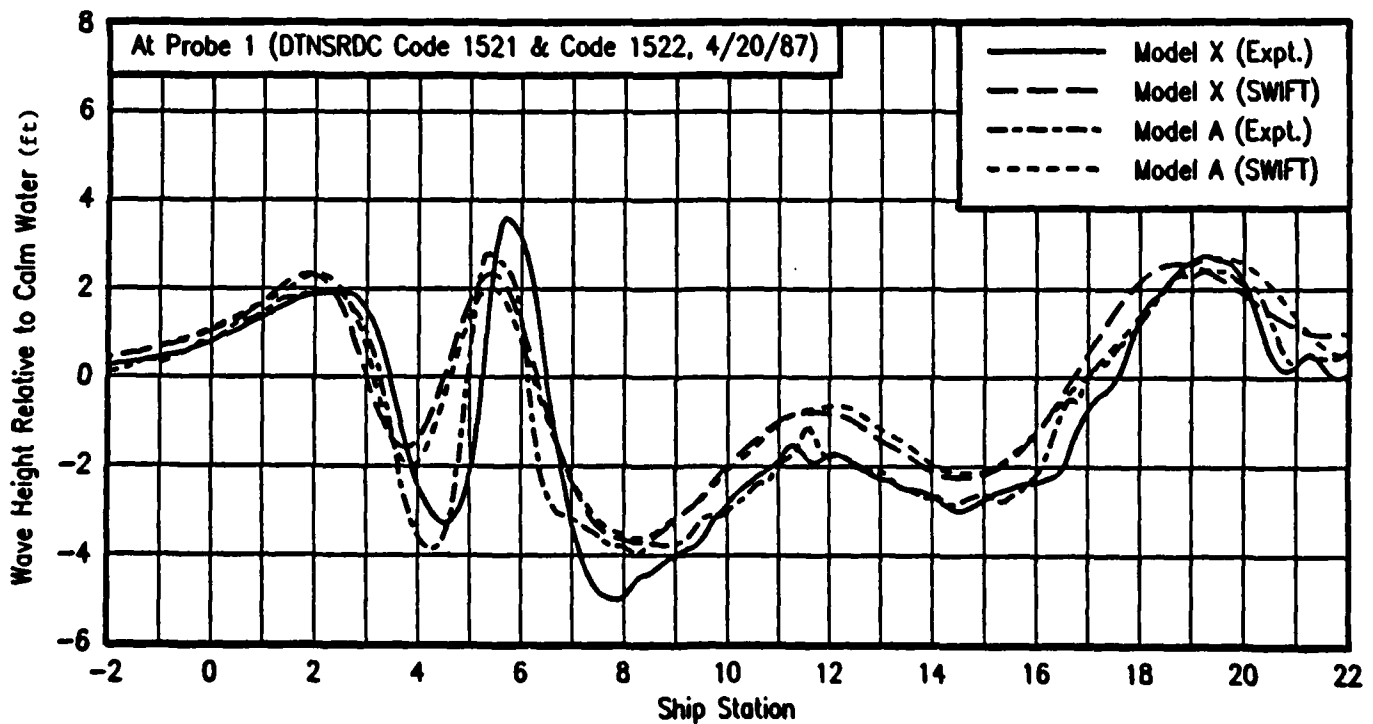


Fig. 45. Longitudinal wave cut at  $F_n=0.238$  (Probe 1).

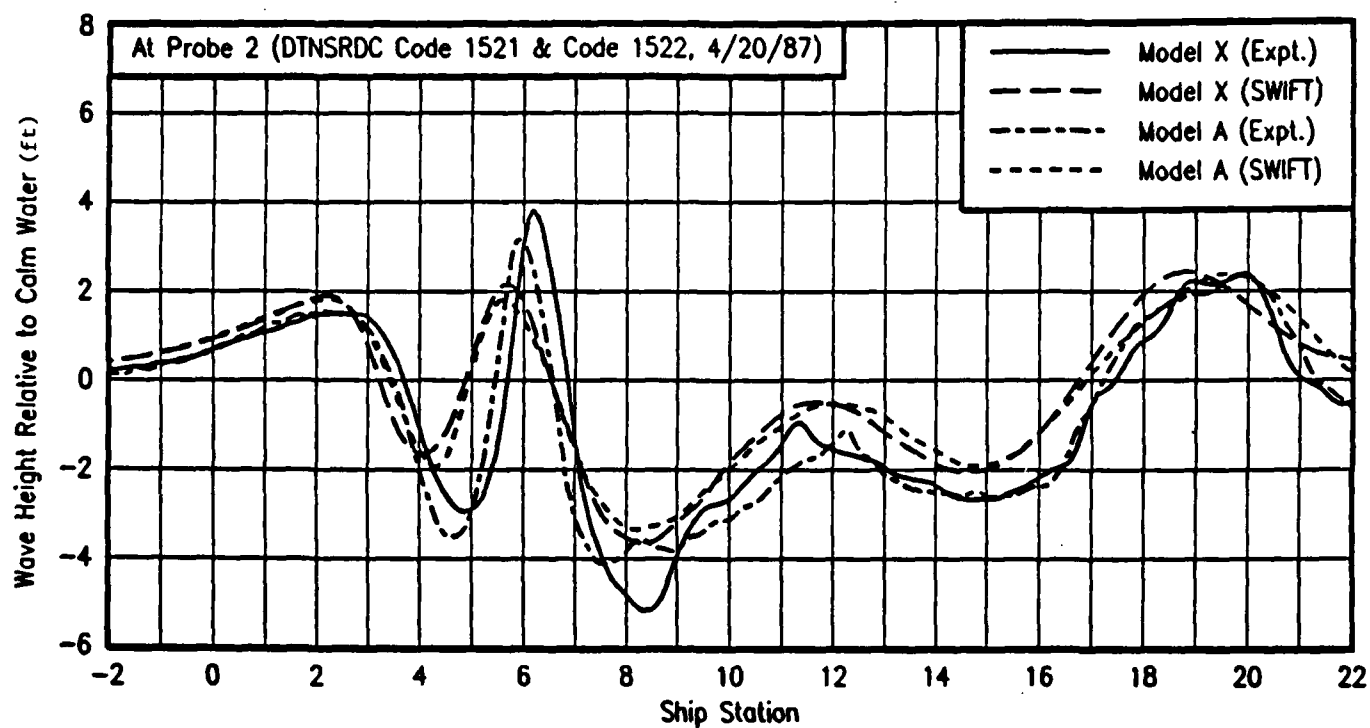


Fig. 46. Longitudinal wave cut at  $F_n=0.238$  (Probe 2).

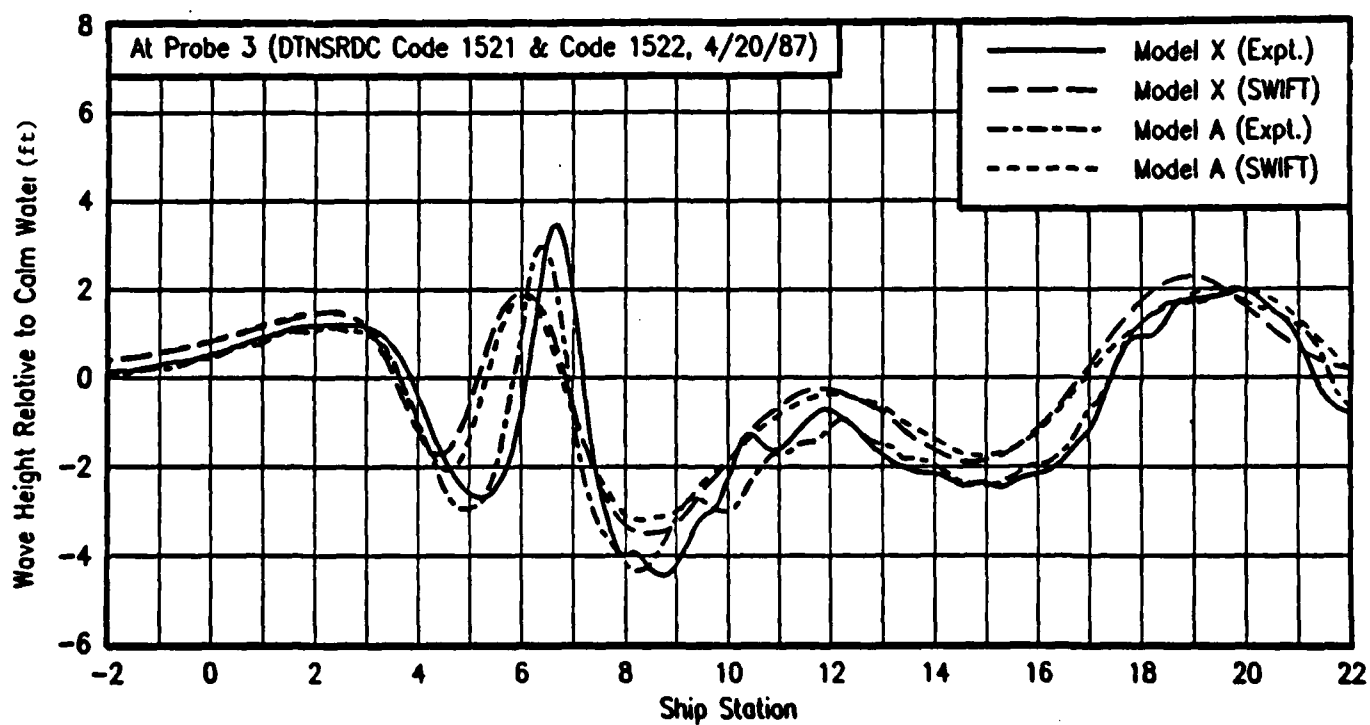


Fig. 47. Longitudinal wave cut at  $F_n=0.238$  (Probe 3).

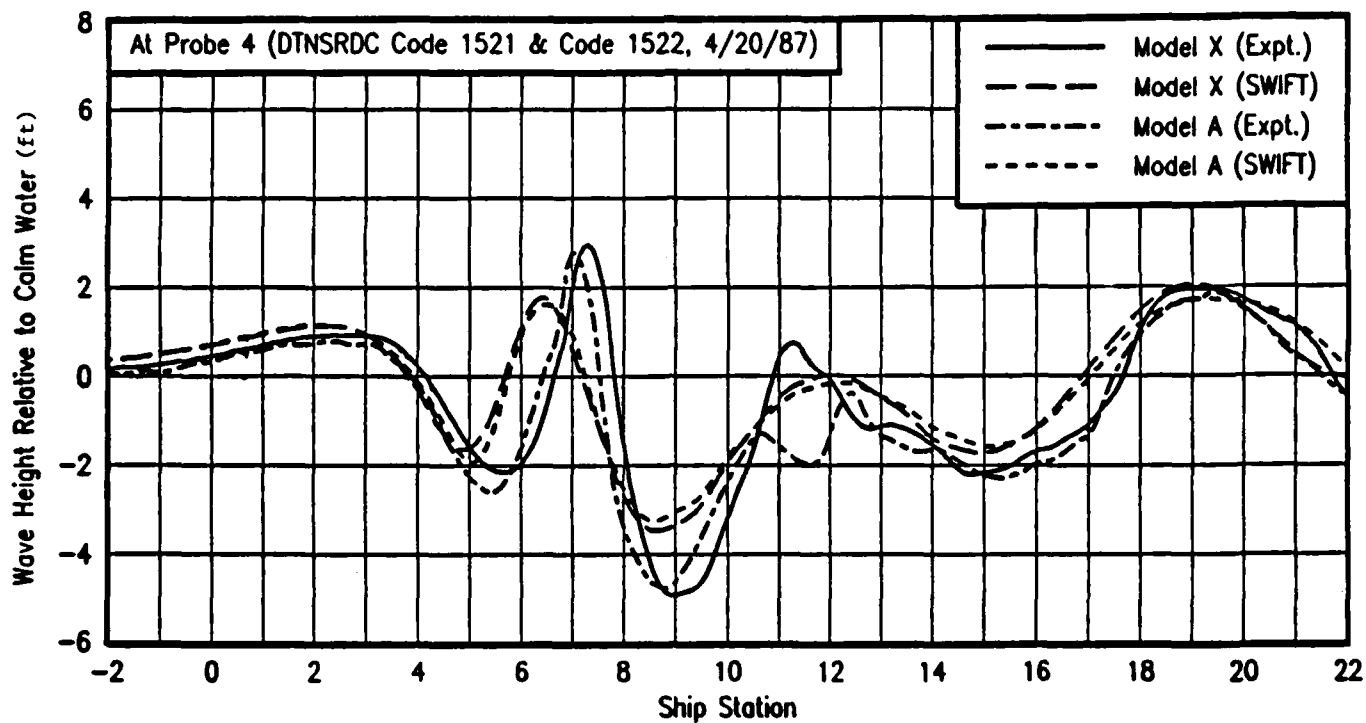


Fig. 48. Longitudinal wave cut at  $F_n=0.238$  (Probe 4).

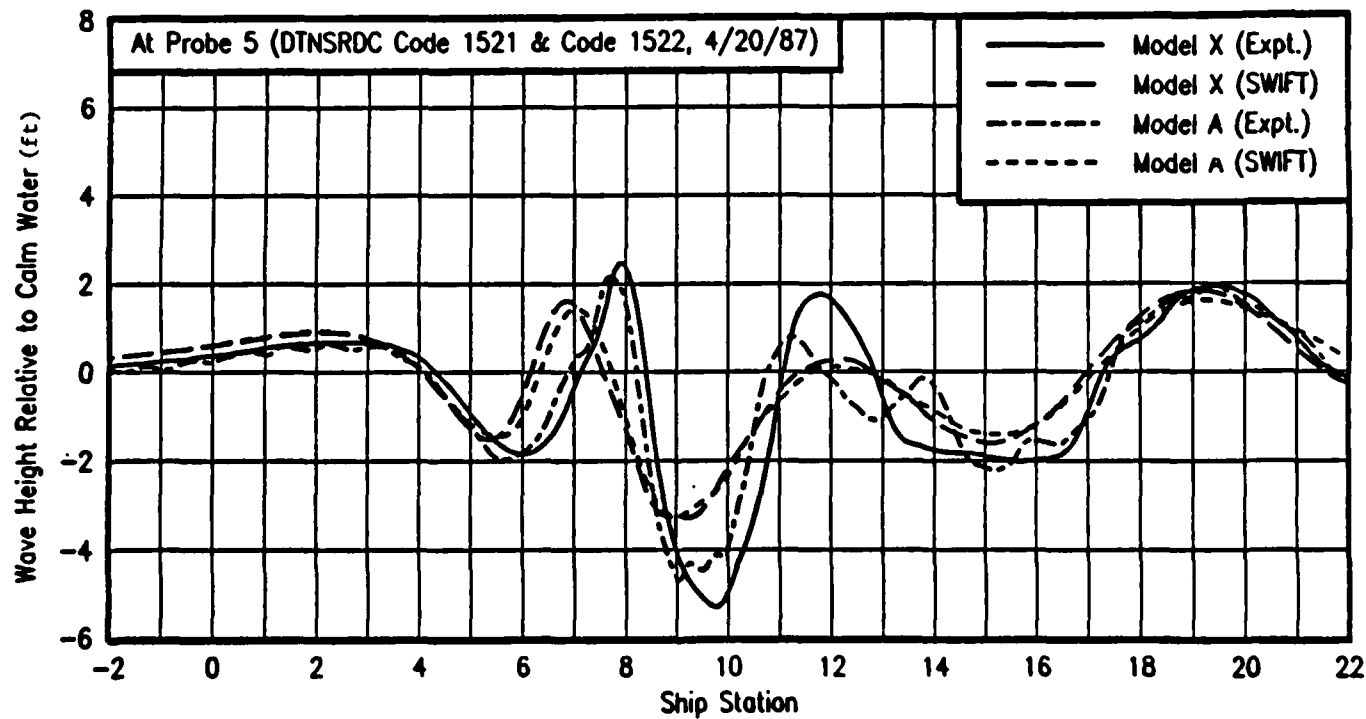


Fig. 49. Longitudinal wave cut at  $F_n=0.238$  (Probe 5).

**Table 1. Comparisons between flat panel and curved panel results.**

No. of Panels	Relative Error (%)							
	Flat Panel.Constant Source				Curved Panel.Linear Source			
	$\phi$	$\phi_x$	$\phi_y$	$\phi_z$	$\phi$	$\phi_x$	$\phi_y$	$\phi_z$
50	3.43	4.52	1.85	1.85	0.64	0.96	0.91	0.91
200	1.71	1.25	0.32	0.32	0.12	0.20	0.27	0.27
520	1.19	0.66	0.22	0.22	0.07	0.17	0.15	0.15

Note : Since the body is axisymmetric, one-quarter of body panels is provided.

The relative error is defined as

$$\text{relative error} = \text{ABS} \left( \frac{\text{computed} - \text{analytic}}{\text{analytic}} \right) \times 100$$

**Table 2. Tables of offsets, Series 60,  $C_B=0.60$ .  
(from Todd, 1953)**

Half breadths of waterline given as fraction of maximum beam on each waterline

Model = 4210W

W.L. 1.00 is the designed load waterline

Forebody prismatic coefficient = 0.881

Afterbody prismatic coefficient = 0.846

Total prismatic coefficient = 0.814

Sta.	Tan.	Waterlines							Area as fraction of max. area to 1.00 W.L.
		0.075	0.25	0.50	0.75	1.00	1.25	1.50	
FP	0.000	0.000	0.000	0.000	0.000	0.000	0.020	0.042	0.000
1/4	0.009	0.032	0.042	0.041	0.043	0.051	0.076	0.120	0.042
1	0.013	0.064	0.082	0.087	0.090	0.102	0.133	0.198	0.085
1 1/4	0.019	0.095	0.126	0.141	0.148	0.160	0.195	0.278	0.135
2	0.024	0.127	0.178	0.204	0.213	0.228	0.270	0.380	0.182
3	0.055	0.196	0.294	0.346	0.368	0.391	0.440	0.631	0.323
4	0.134	0.314	0.436	0.502	0.535	0.562	0.607	0.883	0.475
5	0.275	0.486	0.689	0.800	0.831	0.718	0.784	0.904	0.630
6	0.469	0.630	0.733	0.802	0.824	0.841	0.862	0.989	0.771
7	0.666	0.779	0.864	0.905	0.917	0.928	0.936	0.946	0.880
8	0.831	0.898	0.935	0.971	0.977	0.979	0.981	0.982	0.965
9	0.945	0.964	0.979	0.986	1.000	1.000	1.000	1.000	0.980
10	1.000	1.000	1.000	1.000	1.000	1.000	1.000	1.000	1.000
11	0.985	0.982	0.980	1.000	1.000	1.000	1.000	1.000	0.996
12	0.982	0.922	0.958	0.994	1.000	1.000	1.000	1.000	0.977
13	0.767	0.826	0.892	0.962	0.987	0.994	0.997	1.000	0.838
14	0.622	0.701	0.781	0.864	0.943	0.975	0.990	0.999	0.663
15	0.463	0.580	0.639	0.704	0.857	0.937	0.977	0.994	0.750
16	0.308	0.413	0.483	0.562	0.728	0.857	0.933	0.975	0.608
17	0.188	0.287	0.330	0.413	0.541	0.725	0.844	0.924	0.445
18	0.065	0.152	0.183	0.236	0.321	0.536	0.708	0.834	0.288
18 1/4	0.032	0.102	0.130	0.166	0.218	0.425	0.626	0.789	0.167
19	0.014	0.058	0.076	0.085	0.116	0.308	0.530	0.686	0.109
19 1/4	0.010	0.020	0.020	0.022	0.033	0.183	0.418	0.579	0.040
AP	0.000	0.000	0.000	0.000	0.000	0.082	0.270	0.420	0.004
Max half beam*	0.710	0.964	0.985	1.000	1.000	1.000	1.000	1.000	

\*As fraction of maximum load waterline beam.

Table 3. Offsets for the high-speed hull, Athena.

Sta.	Tan.	0.125	0.25	0.50	0.75	1.00	1.25	1.50
FP	0.0000	0.0000	0.0000	0.0000	0.0000	0.0048	0.0185	0.0347
1/2	0.0000	0.0000	0.0246	0.0359	0.0451	0.0570	0.0758	0.0989
1	0.0000	0.0000	0.0525	0.0818	0.0959	0.1110	0.1354	0.1637
1 1/2	0.0000	0.0000	0.0838	0.1292	0.1462	0.1675	0.1945	0.2267
2	0.0000	0.0000	0.1162	0.1766	0.2035	0.2257	0.2542	0.2886
3	0.0000	0.0377	0.1955	0.2813	0.3104	0.3398	0.3711	0.4081
4	0.0000	0.1029	0.2849	0.3891	0.4218	0.4478	0.4761	0.5129
5	0.0000	0.1972	0.3989	0.4992	0.5280	0.5643	0.5776	0.6078
6	0.0000	0.3036	0.4972	0.6009	0.6246	0.6462	0.6700	0.6990
7	0.0000	0.4305	0.6190	0.6934	0.7070	0.7263	0.7476	0.7703
8	0.0000	0.5918	0.7262	0.7783	0.7830	0.7967	0.8156	0.8345
9	0.0000	0.7410	0.8346	0.8517	0.8448	0.8568	0.8807	0.8889
10	1.0000	0.8868	0.9240	0.9136	0.9002	0.9065	0.9177	0.9199
11	1.0000	1.0000	1.0000	0.9671	0.9420	0.9381	0.9457	0.9488
12	1.0000	0.8353	0.9519	1.0000	0.9762	0.9660	0.9684	0.9699
13	0.0000	0.4580	0.8424	1.0000	0.9942	0.9872	0.9875	0.9888
14	0.0000	0.0000	0.5765	0.9801	1.0000	1.0000	1.0000	1.0000
15	0.0000	0.0000	0.0581	0.9113	0.9865	0.9939	0.9946	0.9953
16	0.0000	0.0000	0.0000	0.7645	0.9575	0.9751	0.9791	0.9799
17	0.0000	0.0000	0.0000	0.4870	0.9227	0.9478	0.9505	0.9517
18	0.0000	0.0000	0.0000	0.0871	0.8731	0.9108	0.9147	0.9134
18 1/2	0.0000	0.0000	0.0000	0.0000	0.8545	0.8926	0.8920	0.8899
19	0.0000	0.0000	0.0000	0.0000	0.8345	0.8695	0.8711	0.8689
19 1/2	0.0000	0.0000	0.0000	0.0000	0.8068	0.8477	0.8461	0.8416
20 (AP)	0.0000	0.0000	0.0000	0.0000	0.8023	0.8289	0.8216	0.8168
Max. half beam	0.0073	0.3538	0.5431	0.7937	0.9424	1.0000	1.0170	1.0303

Table 4. Principal dimensions and form coefficients of Models X, A, and C.

Model X

PRINCIPAL DIMENSIONS	NONDIMENSIONAL COEFFICIENTS			
LENGTH (Lpp) = 900.00 ft (274.32 m)	C <sub>B</sub> = 0.343	C <sub>VP</sub> = 0.771	A <sub>g</sub> /A <sub>x</sub> = 0.003	
LENGTH (Lwl) = 910.65 ft (277.57 m)	C <sub>P</sub> = 0.579	C <sub>VP</sub> = 0.879	L <sub>g</sub> /L <sub>wl</sub> = 0.233	
BEAM (B <sub>x</sub> ) = 141.10 ft (43.01 m)	C <sub>PP</sub> = 0.546	C <sub>VPA</sub> = 0.694	L <sub>p</sub> /L <sub>wl</sub> = 0.000	
DRAFT (T <sub>x</sub> ) = 35.36 ft (10.79 m)	C <sub>PL</sub> = 0.613	C <sub>S</sub> = 2.669	L <sub>g</sub> /L <sub>wl</sub> = 0.212	
TRIM = 0.00 ft (+ bow)	C <sub>PE</sub> = 0.516	C <sub>S</sub> = 0.045	L <sub>p</sub> /L <sub>wl</sub> = 0.506	
DISPLACEMENT = 70560 L (71688 t)	C <sub>PE</sub> = 0.585	L <sub>wl</sub> /B <sub>x</sub> = 6.454	FF/L <sub>wl</sub> = 0.552	
WETTED SURFACE = 127942 sq ft (11886.2 sq m)	C <sub>E</sub> = 0.938	B <sub>g</sub> /T <sub>x</sub> = 3.990	C <sub>V</sub> = 0.00327	
lg = 7.343 degrees	C <sub>UP</sub> = 0.705	A <sub>g</sub> /A <sub>x</sub> = 0.000	⑤ = 7.007	
lg = 10.214 degrees	C <sub>UP</sub> = 0.582	B <sub>g</sub> /B <sub>x</sub> = 0.000	⑥ = 6.739	
lg = 20.370 degrees	C <sub>VPA</sub> = 0.887	T <sub>p</sub> /T <sub>x</sub> = 0.000	A/(.01L <sub>wl</sub> ) <sup>3</sup> = 93.42	

Model A

PRINCIPAL DIMENSIONS	NONDIMENSIONAL COEFFICIENTS			
LENGTH (Lpp) = 900.00 ft (274.32 m)	C <sub>B</sub> = 0.593	C <sub>VP</sub> = 0.814	A <sub>g</sub> /A <sub>x</sub> = 0.001	
LENGTH (Lwl) = 913.88 ft (278.55 m)	C <sub>P</sub> = 0.582	C <sub>VP</sub> = 0.937	L <sub>g</sub> /L <sub>wl</sub> = 0.232	
BEAM (B <sub>x</sub> ) = 126.21 ft (38.47 m)	C <sub>PP</sub> = 0.548	C <sub>VPA</sub> = 0.729	L <sub>p</sub> /L <sub>wl</sub> = 0.000	
DRAFT (T <sub>x</sub> ) = 35.83 ft (10.92 m)	C <sub>PL</sub> = 0.615	C <sub>S</sub> = 2.718	L <sub>g</sub> /L <sub>wl</sub> = 0.213	
TRIM = 0.00 ft (+ bow)	C <sub>PE</sub> = 0.578	C <sub>S</sub> = 0.046	FF/L <sub>wl</sub> = 0.503	
DISPLACEMENT = 70090 L (71211 t)	C <sub>PE</sub> = 0.586	L <sub>wl</sub> /B <sub>x</sub> = 7.421	FF/L <sub>wl</sub> = 0.553	
WETTED SURFACE = 128247 sq ft (11949.9 sq m)	C <sub>E</sub> = 1.020	B <sub>g</sub> /T <sub>x</sub> = 3.522	C <sub>V</sub> = 0.00321	
lg = 7.287 degrees	C <sub>UP</sub> = 0.729	A <sub>g</sub> /A <sub>x</sub> = 0.000	⑤ = 7.075	
lg = 9.823 degrees	C <sub>UP</sub> = 0.597	B <sub>g</sub> /B <sub>x</sub> = 0.000	⑥ = 6.778	
lg = 20.003 degrees	C <sub>VPA</sub> = 0.925	T <sub>p</sub> /T <sub>x</sub> = 0.000	A/(.01L <sub>wl</sub> ) <sup>3</sup> = 91.83	

Model C

PRINCIPAL DIMENSIONS	NONDIMENSIONAL COEFFICIENTS			
LENGTH (Lpp) = 910.00 ft (277.32 m)	C <sub>B</sub> = 0.588	C <sub>VP</sub> = 0.810	A <sub>g</sub> /A <sub>x</sub> = 0.001	
LENGTH (Lwl) = 914.79 ft (278.83 m)	C <sub>P</sub> = 0.577	C <sub>VP</sub> = 0.931	L <sub>g</sub> /L <sub>wl</sub> = 0.233	
BEAM (B <sub>x</sub> ) = 126.26 ft (38.48 m)	C <sub>PP</sub> = 0.558	C <sub>VPA</sub> = 0.728	L <sub>p</sub> /L <sub>wl</sub> = 0.000	
DRAFT (T <sub>x</sub> ) = 36.10 ft (11.00 m)	C <sub>PL</sub> = 0.616	C <sub>S</sub> = 2.713	L <sub>g</sub> /L <sub>wl</sub> = 0.213	
TRIM = 0.00 ft (+ bow)	C <sub>PE</sub> = 0.568	C <sub>S</sub> = 0.046	FF/L <sub>wl</sub> = 0.507	
DISPLACEMENT = 70089 L (71211 t)	C <sub>PE</sub> = 0.586	L <sub>wl</sub> /B <sub>x</sub> = 7.245	FF/L <sub>wl</sub> = 0.555	
WETTED SURFACE = 128490 sq ft (11937.1 sq m)	C <sub>E</sub> = 1.020	B <sub>g</sub> /T <sub>x</sub> = 3.498	C <sub>V</sub> = 0.00320	
lg = 7.235 degrees	C <sub>UP</sub> = 0.726	A <sub>g</sub> /A <sub>x</sub> = 0.000	⑤ = 7.067	
lg = 9.823 degrees	C <sub>UP</sub> = 0.589	B <sub>g</sub> /B <sub>x</sub> = 0.000	⑥ = 6.784	
lg = 20.007 degrees	C <sub>VPA</sub> = 0.928	T <sub>p</sub> /T <sub>x</sub> = 0.000	A/(.01L <sub>wl</sub> ) <sup>3</sup> = 91.56	

**THIS PAGE INTENTIONALLY LEFT BLANK**

## REFERENCES

1. Michell, J.H., "The Wave Resistance of a Ship." Phil. Mag., pp 106-123. Vol. 45. 1898.
2. Hess, J.L. and A.M.O. Smith, "Calculation of Nonlifting Potential Flow about Arbitrary Three-Dimensional Bodies," Douglas Aircraft Company Report No. ES40622, March 1962.
3. Xia, Fei, "Calculation of Potential Flow with a Free Surface" (amended version). SSPA Report No. 2912-1. SSPA Maritime Research and Consulting, Goteborg. Sweden. 1984.
4. Dawson, C.W., "A Practical Computer Method for Solving Ship-Wave Problems," Proc. the 2nd International Conference on Numerical Ship Hydrodynamics. Berkeley, California, 1977.
5. Johnson, F.T., "A General Panel Method for the Analysis and Design of Arbitrary Configuration in Incompressible Flow," NASA Contract Report 3079. Boeing Comm. Airplane Co., Seattle, 1980.
6. Dongarra, J.J. and S.C. Eisenstat, "Squeezing the Most out of an Algorithm in Cray Fortran." ACMT Trans. on Math. Software, Vol. 10, No. 3, 1984.
7. Report of the 17th ITTC Resistance Committee, 1984.
8. Kim, Y.-H. and D. Jenkins, "Trim and Sinkage Effects on Wave Resistance with Series 60,  $C_B = 0.60$ ." DTNSRDC/SPD-1013-01, 1981.
9. Beaver, W.E., "Predicted Calm Water Wave Elevations and Powering for Aircraft Carrier CV-41 and Alternative Hull Forms Represented by Model 5457, 5460, and 5461." DTNSRDC/SHD-0861-05, 1987.
10. Lindenmuth, W.T., T.J. Ratcliffe, and A.M. Reed. "Comparative Accuracy of Numerical Kelvin Wake Code Prediction - 'Wake-Off'," DTRC/SHD-1260-01(May 1988).
11. Shearer, J.R. and J.J. Cross, "The Experimental Determination of the Components of Ship Resistance for a Mathematical Model," Trans. Inst. Naval Arch. Vol. 107. pp 459-473. 1965.
12. Todd, F.H., "Some Further Experiments on Single-Screw Merchant Ship Forms-Series 60." Trans. SNAME, 1953.



**THIS PAGE INTENTIONALLY LEFT BLANK**

## INITIAL DISTRIBUTION

### Copies

<p>4 OCNR</p> <p style="padding-left: 20px;">1 121 R. Hansen</p> <p style="padding-left: 20px;">1 1132 R. Whitehead</p> <p style="padding-left: 20px;">1 1215 J. Fein</p> <p style="padding-left: 20px;">1 1132F E. Rood</p> <p>12 NAVSEA</p> <p style="padding-left: 20px;">1 503 D. Ewing</p> <p style="padding-left: 20px;">1 5012 R. Nix</p> <p style="padding-left: 20px;">1 5045 J. Sandison</p> <p style="padding-left: 20px;">1 55W3 E. Comstock</p> <p style="padding-left: 20px;">1 55W3 A. Engle</p> <p style="padding-left: 20px;">1 50151 C. Kennell</p> <p style="padding-left: 20px;">1 55N32 K. Yankaskas</p> <p style="padding-left: 20px;">1 55N36 J. Kim</p> <p style="padding-left: 20px;">1 55W32 S. Chun</p> <p style="padding-left: 20px;">1 55W33 D. McCallum</p> <p style="padding-left: 20px;">1 55W33 R. Conrad</p> <p style="padding-left: 20px;">1 55W33 C. Chen</p> <p>2 NRL</p> <p style="padding-left: 20px;">1 W. Sanberg</p> <p style="padding-left: 20px;">1 H. Wang</p> <p>2 USNA</p> <p style="padding-left: 20px;">1 Hydro Lab/B. Johnson</p> <p style="padding-left: 20px;">1 Tech. Lib.</p> <p>1 Library of Congress</p> <p style="padding-left: 20px;">Science and Tech. Div.</p> <p>2 DTIC</p>	<p>3 U. of Michigan/Dept of NAME</p> <p style="padding-left: 20px;">1 NAME Lib.</p> <p style="padding-left: 20px;">1 R. Beck</p> <p style="padding-left: 20px;">1 A. Trosch</p> <p>4 U. of Calif.. Berkeley/Dept of NAOE</p> <p style="padding-left: 20px;">1 J. Wehausen</p> <p style="padding-left: 20px;">1 R. Yeung</p> <p style="padding-left: 20px;">1 W. Webster</p> <p style="padding-left: 20px;">1 NAOE Lib.</p> <p>4 MIT/Dept of Ocean Engr</p> <p style="padding-left: 20px;">1 J. Newman</p> <p style="padding-left: 20px;">1 P. Sclavounos</p> <p style="padding-left: 20px;">1 D. Yue</p> <p style="padding-left: 20px;">1 OE Lib.</p> <p>3 U. of Iowa</p> <p style="padding-left: 20px;">1 F. Stern</p> <p style="padding-left: 20px;">1 V. Patel</p> <p style="padding-left: 20px;">1 Hydraulic Lab.</p> <p>2 Boeing Company</p> <p style="padding-left: 20px;">1 F. Johnson</p> <p style="padding-left: 20px;">1 Marine System</p> <p>5 U. of N.C..Charlotte</p> <p style="padding-left: 20px;">5 T. Lucas</p> <p>2 NASA/Ames Res. Ctr</p> <p style="padding-left: 20px;">1 D. Kwak</p> <p style="padding-left: 20px;">1 S. Yoon</p>
---	--

# INITIAL DISTRIBUTION (Continued)

## Copies

2	Webbs Institute
1	P. Gale
1	Tech. Lib.
2	SAIC
1	N. Salveson (Annapolis)
1	C. Scragg (San Diego)
1	U. of New Orleans/School of NAME
1	S. Liapis

## CENTER DISTRIBUTION (Continued)

Copies	Code	Name
1	1521	W. Beavor
1	1521	D. Cusanelli
1	1521	K. Lynaugh
20	1522	Y.-H. Kim
1	1522	D. Jenkins
1	1522	T. Ratcliffe
1	1522	J. Wood
1	1542	F. Noblesse
1	1544	A. Reed
1	1544	K.-H. Kim
1	1564	Y. Hong
1	1843	B. Cheng
1	522.1	TIC(C)
1	522.2	TIC(A)
10	522.6	Reports Control

## CENTER DISTRIBUTION

Copies	Code	Name
1	015	S. Hawkins
1	15	W. Morgan
1	16	H. Chaplin
1	152	W. Lin
1	1504	V. Monacella
1	1506	D. Walden
1	1521	B. Day
1	1522	M. Wilson
1	1540.1	B. Yim
1	1235	B. Lamb
1	1501	H. Haussling
1	1501	C. Lin
1	1501	S. Fisher
1	1501	J. Smith
1	1521	G. Karafiath
1	1521	W. Lindenmuth
1	1521	H. Liu
1	1521	P. Chang
1	1521	W. Cave